Spectroscopy of ^{163,165}Os and ^{164}Ir

Thesis submitted in accordance with the requirements of the University of Liverpool for the degree of Doctor in Philosophy

by

Mark Christopher Drummond

Oliver Lodge Laboratory

2013

Acknowledgements

Firstly, I would like to thank my supervisor, Prof. Robert Page, for all his guidance and support throughout my studies. Robert's knowledge of nuclear physics is seemingly boundless and something to aspire to. I am extremely fortunate to have worked under him.

I am also hugely grateful to Dr. David Joss. Without Dave I wouldn't be where I am today. Besides his ability to get me out of difficult situations, he has also served as a brilliant, although unofficial, supervisor.

Next to thank is Dr. Dave O'Donnell. Absolute legend. If I listed the amount of times Dave helped me with something, this thesis would be at least a quarter of a page longer. On a serious note, Dave is a great friend and extremely talented nuclear physicist. I can only hope to be as good a physicist as he in the future.

I would like to thank the STFC for providing the funding for my research. I would also like to thank all the people at the Liverpool and Jyväskylä that made the research possible.

A huge thanks to: Dr. Rob Carroll for getting me started. Unfortunately, I think neither of us will forget our first meeting. Dr. Liam Gaffney for all his help on computing and being a pure dafty, pears? Ha'way man. Joe Rees, a great friend of mine and an overall canny lad. I can't remember the amount amount of times Joe has been there for me... literally. Bahadır Sayğı, another good friend who has put up with me many times when I've needed a bed.

I'd also like to thank all the other friends I have made in the department: Andy Mistry, John Revill, Eddie Parr, Paul Sapple... the list goes on.

Thanks to all my friends, Philly, Ifan, Tom, Laura, Hannah, Mike, Úna and all the others that have been there to share many a Brazzer when I've needed them. I'd especially like to thank Smudge and Emily, two amazing friends, without whom

I would have been homeless for the last few months of my PhD.

Lastly, I'd like to thank my family: Adrian, Maria, Emma and the new addition to the family, Annabelle, for supporting me all the way in everything I've done. Thank you to my gran, to whom I apparently owe my supposed intelligence. Finally, the biggest thank you of all goes to my mam and dad for their emotional and financial support; I owe everything that I have acheived to them.

Abstract

Excited states in the neutron-deficient isotopes ^{163}Os and ^{165}Os were identified using JUROGAM and GREAT spectrometers in conjunction with the RITU gas-filled separator. The ^{163}Os and ^{165}Os nuclei were populated via the ^{106}Cd(^{60}Ni,3n) and ^{92}Mo(^{78}Kr,2p3n) reactions at bombarding energies of 270 MeV and 357 MeV, respectively. Gamma-ray emissions from these nuclei have been established unambiguously using the recoil-decay tagging technique and a coincidence analysis has allowed level schemes to be established. These results suggest that the yrast states are based upon negative-parity configurations originating from the $\nu f_{7/2}$ and $\nu h_{9/2}$ orbitals.

The neutron deficient odd-odd nucleus ^{164}Ir has been studied using the GREAT spectrometer in conjuction with the RITU gas-filled separator. The experiment was performed using the ^{92}Mo(^{78}Kr, $p5n$)^{164}Ir reaction at bombarding energies of 420-450 MeV for 12 days. An alpha decay has been observed for the first time with an energy of 6880 $\pm$ 10 keV and a branching ratio of 4.8 $\pm$ 2.2 % and assigned as the decay of the πh$_{11/2}$ state of ^{164}Ir. The energy of the proton decay of the high-spin state has been measured to a higher precision as 1814 $\pm$ 6 keV. The half life of this state has been measured to be 70 $\pm$ 10 μs. The DSSDs of the GREAT spectrometer have been instrumented using digital electronics for the first time and a pulse shape analysis has been performed to observe particle emission within the dead time of the detector.

Contents

List of Figures

Chapter 1

Introduction

Since the discovery of radioactivity by Becquerel in 1896 physicists have been fascinated with the deeper structure of the atom. Thanks to studies that led to the description of the atom as a concentrated positive mass orbited by electrons in 1911 [6] and later the discovery of the neutron in 1932 [7], the building blocks for describing the nuclear landscape were set. At present around 3000 nuclei are known, of which only about 300 are stable. Today the challenge is to understand these complicated structures.

The nucleus is a complex many-body system of fermions governed by the interplay of several forces, the strongest of these being the well-understood Coulomb force and the not-so-well understood strong nuclear force. Solving Schrödinger's equation for these many-body problems becomes increasingly difficult, and at present the computational power required to solve the wavefuntion for $A > 7$ is too high. It is therefore neccessary to understand the interactions within heavy nuclei in terms of models. The behaviour of the nucleus is governed not only by single-particle interactions, but also by its bulk properties. Accordingly, it is possible to describe the nucleus using a shell model when all particles are considered separately, or using a collective model where the behaviour is better described by bulk properties.

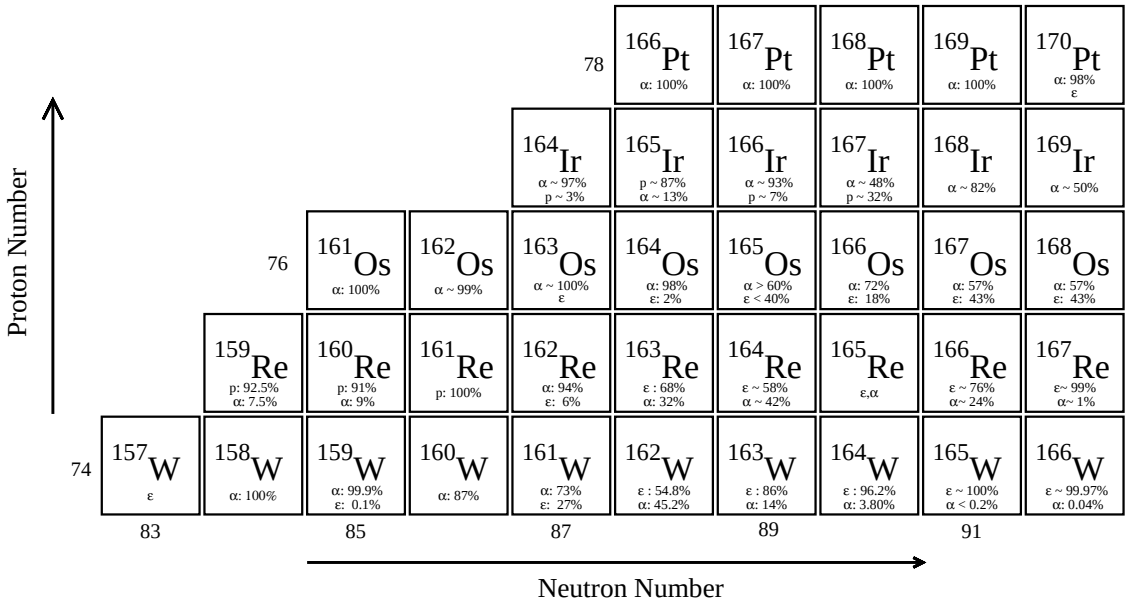

Figure 1.1: A (small) section of the chart of nuclides in the region of interest. Proton and neutron numbers are indicated. The decay mode branching ratios are also shown.

In the spherical shell model, proton and neutron energy levels are filled according to the Pauli exclusion principle. Large gaps in the energy levels appear at certain particle numbers (2, 8, 20, 28, 50, 82, 126) called magic numbers. Around these numbers nuclei take on a spherical shape as the shells are nearly full. These regions are therefore perfect for probing single-particle/hole excitations. In this work, nuclei of interest are located just below the $Z = 82$ shell gap and just above the $N = 82$ shell gap around the proton drip line, where the proton separation energy becomes zero. Lifetimes of nuclei in this area decrease rapidly with decreasing N as the proton drip line is approached.

The area of the Segrè chart studied in this thesis is shown in Figure 1.1. It can be seen from the decay branching ratios that the two main competing decay modes are alpha and proton emission. Iridium is particularly intersting as it is one of only two elements of which four proton-emitting isotopes exist, the other being thulium. Spectroscopy of proton-emitting nuclei in this area burgeoned in recent years due to increasingly advanced detector systems, but the limit of our studies is

fast approaching as lifetimes of states become shorter than our systems can detect. It is therefore crucial that we adapt conventional detection techniques as we study these nuclei nearing the limit of existence. Part of this thesis describes new detection and analysis techniques for short-lived proton decays. Investigating iridium isotopes allows us to probe the limits of existence and is a stringent test for theoretical models. Furthermore because proton decay does not require a preformation factor, structural information can be extracted directly from the properties of the decay. The very proton-rich nucleus $^{164}\mathrm{Ir}_{87}$ will be a focus in this study.

The proton daughter nucleus of ^{164}Ir, $^{163}\mathrm{Os}_{87}$, forms part of one of the best known isotopic chains in this area. The osmium isotopes currently represent the best opportunity to probe the evolution of nuclear structure across the $82 \leq N \leq 126$ neutron shell. The existence of the osmium isotopes in an uninterrupted sequence from $^{161}\mathrm{Os}_{85}$ [8] to $^{200}\mathrm{Os}_{124}$ [9] has been established through the measurement of their radioactive decay properties [10]. Excited states have been established in these known nuclei below $^{196}\mathrm{Os}_{120}$ with the exception of the odd-mass isotopes below $N = 89$. The excitation level schemes across the shell reveal the transitions between the single-particle and collective regimes as a function of neutron number.

The low-lying energy spectra in the osmium isotopes have been investigated from different theoretical perspectives. For example, the neutron-deficient osmium isotopes have been discussed in terms of general collective models [11], shape co-existence [12, 13, 14] and phase transitions between the limiting symmetries of the interacting boson approximation [15]. However, most theoretical investigations have focused on the even-N isotopes above $^{170}\mathrm{Os}_{94}$ and little is known about the transition to single-particle structures as the $N = 82$ closed shell is approached.

The discovery of yrast states in the Os isotopes at greater neutron deficiency has flourished with the advent of selective tagging techniques [16, 17, 18, 19, 20]. Prior to this work, γ-ray transitions in ^{165}Os have been identified but no level scheme of

excited states was proposed [18]. However, the spin and parity of the ground state of ^{165}Os have been assigned to be $7/2^-$ on the basis of the measured proton and α radioactivity observed in a correlated decay chain originating from ^{170}Au [21]. The ground state of ^{163}Os is also assigned as having spin and parity $7/2^-$ on the basis of the low hindrance factor of its α decay to the $7/2^-$ ground state of ^{159}W [22, 23]. This work reports the first level schemes for $^{163}Os_{87}$ and $^{165}Os_{89}$, providing knowledge of low-lying yrast states in an unbroken chain of isotopes from $^{162}Os_{86}$ [16] to $^{199}Os_{123}$ [24].

Chapter 2

Physics Background

The existence of heavy nuclei requires a force stronger than the Coulomb repulsion to be present within the nucleus. Understanding the strong nuclear force is a formidable challenge. Instead of describing a whole picture of the potential, theoretical models are chosen that best describe empirical observations. There are a few general properties, however, that can be determined by experiment. For example, experiments show that the nuclear radius is of the order of 10^{-15} to 10^{-14} m and the nuclear force can be neglected when considering atomic and molecular phenomena. These observations are indicative of a strong short-range force that only affects hadronic matter. As obvious as this statement may seem, it has important implications when attempting to describe the overall potential within the nucleus.

A basic theoretical understanding of the nucleus and the forces involved is vital for the interpretation of the results presented in this thesis. This chapter will describe some of the important aspects one must consider when describing the structure of the nucleus and the decay mechanisms involved in alpha, proton and gamma decay. Later in chapter 6 some of the discussed topics will be reintroduced to compare current theoretical models.

2.1 Nuclear Models

2.1.1 The Semi-Empirical Mass Formula

The problem of interactions within a nucleus comprising more than a few nucleons is too complex to be solved analytically. The nucleus is therefore described using both bulk properties and residual single-nucleon interactions. The important observation that the mass of a nucleus is less than the sum of its constituents led to the proposal of *nuclear binding energy*. It was proposed that the binding energy would be a function of the atomic number, Z, and the neutron number, N, and are given by the equation

$$B(Z,A) = M(Z,A) - ZM_H - NM_N, \tag{2.1}$$

where $M(Z,A)$ is the atomic mass, M_H is the mass of a hydrogen atom and M_N is the mass of a neutron. Nuclei radioactively decay towards stability to increase their binding energy per nucleon. It was therefore deduced that there would be a limit either side of stability for a given isotope at which the binding energy falls so low that particle emission is favoured. These limits are called the proton and neutron drip lines (See Fig 2.1). Based on the liquid-drop model, the semi-empirical mass formula gave an early prediction to where these limits existed. This is given by

$$B(Z,A) = a_{vol}A - a_{surf}A^{\frac{2}{3}} - a_{Coul}\frac{Z^2}{A^{\frac{1}{3}}} - a_{sym}\frac{(N-Z)^2}{A} - \delta(Z,N), \tag{2.2}$$

where

$$f(t_n) = \begin{cases} -a_{pair}A^{-\frac{3}{4}} & \text{if } Z \text{ and } N \text{ are even} \\ 0 & \text{if } A \text{ is odd} \\ a_{pair}A^{-\frac{3}{4}} & \text{if } Z \text{ and } N \text{ are odd} \end{cases}, \tag{2.3}$$

and $a_{vol},\ a_{surf},\ a_{Coul},\ a_{pair}$ and a_{sym} are the volume, surface, Coulomb, pairing and symmetry constants respectively. Examples of these constants and their origin are described more fully in [25] and [26]. The limits of proton and neutron stability lie far from beta stability where there is a superabundance of protons (neutrons); they occur because the binding energy of the last added particle is so low that it is energetically favoured to "drip" off. In these nuclei the energy needed to remove the last proton, the proton separation energy, given by

$$S_p = B({}^{A}_{Z}X_N) - B({}^{A-1}_{Z-1}X_N), \tag{2.4}$$

is < 0. Figure 2.1 shows a Segrè chart of known nuclei, with stable nuclei highlighted in black. Nuclei can exist beyond the proton drip line, because of the hindering effect of the Coulomb potential, which will be discussed in further detail later. The implications of Coulomb repulsion are immediately obvious as stable nuclei quickly decouple from the $N = Z$ line. More neutrons than protons are needed to balance out this repulsion, the result being that most nuclei contain more neutrons than protons. This effect is described in Equation 2.2 where the Coulomb term decreases as the $Z^2/A^{1/3}$ decreases. Coulomb repulsion is also the main reason for saturation of binding energy per nucleon at the proton drip line, as the symmetry term is very low in comparison. This is in contrast to the neutron drip-line where for a given isotope the rapidly increasing symmetry term becomes the important factor in reducing the binding energy.

One notable feature of the semi-empirical mass formula is the pairing term. The pairing term extends the borders of the proton drip line for even-Z nuclei, this causes staggering of the proton drip line between odd and even nuclei. One consequence of this staggering is that there are no known even-Z nuclei that decay by the emission of a single proton above $Z = 8$.

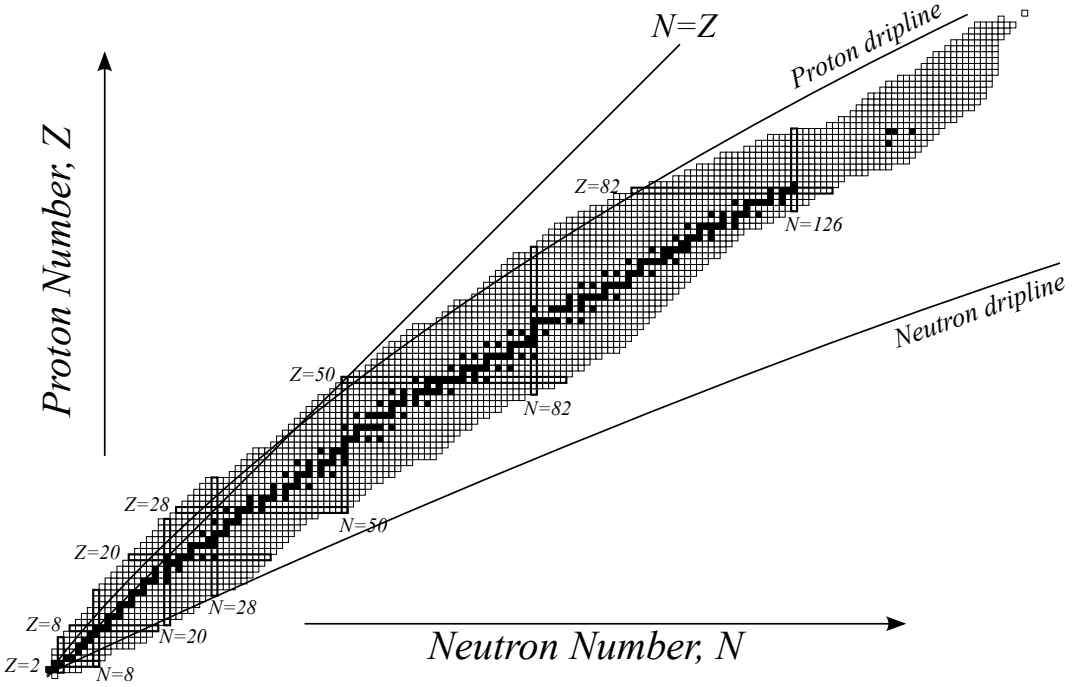

Figure 2.1: A Segré chart. Naturally occuring nuclei are highlighted in black

Although the semi-empirical mass formula works relatively well at predicting the proton and neutron drip lines, it does not take into account any nuclear shell structure. At certain nucleon numbers, *magic numbers*, the binding energy predicted by Equation 2.2 varies greatly from experimental measurements [27]. To describe the nucleus more thoroughly and account for these shell effects, individual contributions from nucleons within the nucleus must be considered.

2.1.2 The Independent Particle Model

To account for the shell effects observed at magic numbers ($N, Z = 2$, 8, 20, 28, 50, 82 and 128), all single-particle contributions to the system must be considered. The independent particle model treats each nucleon as a particle within a common potential. The two-body problem can then be solved for all nucleons within the system provided they obey the Pauli exclusion principle. To start a Hamiltonian for

a particle i moving in the system that experiences a force from particles k is defined as

$$H = T + V = \sum_{i=1}^{A} \frac{\hat{p}_i^2}{2m_i} + \sum_{i>k=1}^{A} V_{ik}(\hat{r}_i - \hat{r}_k), \tag{2.5}$$

where T_i and m_i are the kinetic energy and mass of the ith nucleon, respectively, V_{ik} is the potential experienced between the ith and kth nucleons with positions $\hat{r}_{ik}$, and $\hat{p}$ is the momentum operator. The potential V_{ik} represents the strong nuclear force felt between both protons and neutrons. The Coulomb potential is much weaker than the strong nuclear force and is ignored. This is valid as neutrons experience the same magic numbers as protons and thus must feel the same potential. As stated previously, a simplification of this potential is nesessary to solve the Hamiltonian. The nucleus is therefore described as a common potential, U_i, within which all nucleons move with an added perturbation called the *residual interaction* to account for single nucleon iteractions. The Hamiltonian for such a system is found by adding and subtracting a common potential from Equation 2.5:

$$H = \sum_{i=1}^{A} \left[\frac{\hat{p}_i^2}{2m_i} + U_i(r) \right] + \sum_{i>k=1}^{A} V_{ik}(\hat{r}_i - \hat{r}_k) - \sum_{i=1}^{A} U_i(r) \equiv H_0 + H_{residual}, \tag{2.6}$$

where H_0 is the Hamiltonian of the mean-field potential and $H_{residual}$ is the Hamiltonian of the perturbation given by residual interactions. For the purposes of this discussion the residual interaction will be ignored and the Hamiltonian will only be taken to the first order. Picking an appropriate mean-field potential is essential to finding a suitable model that describes observations best. As a first attempt at extracting eigenvalues of the Hamiltonian, a potential well that best describes the nuclear force is chosen.

The square well shown in Figure 2.2 is clearly an unrealistic description of the nuclear potential, and does not reproduce the magic numbers. The harmonic oscillator potential has angular momentum degeneracy. A centrifugal term, often referred

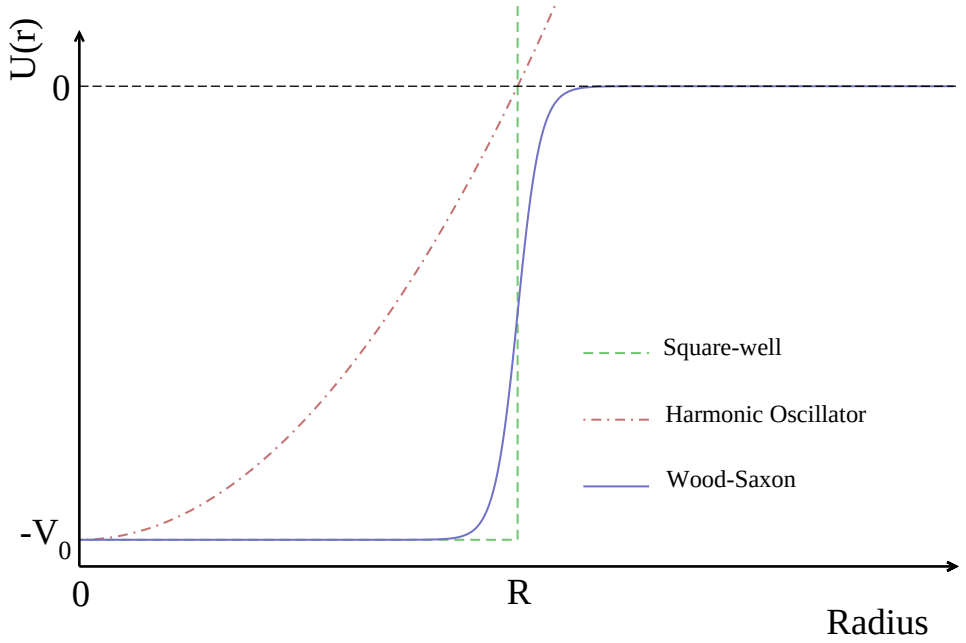

Figure 2.2: Theoretical potentials of the nuclear force. The Woods-Saxon incorporates features from both the square well and the simple harmonic oscillator

to as the ℓ^2 term, is added to account for energy differences due to different spins that are observed experimentally. Spin-orbit coupling, proposed simultaneously by Mayer [28] and Haxel *et al.* [29], gives rise to another important correction that must be applied to the potential in order to obtain a more realistic model of the nucleus. When both corrections are added the final potential is relatively good at reproducing the first few magic numbers. However, because the strong nuclear force is a finite short range force, the shape of the potential is clearly not a good reflection of the short range nuclear force. The Woods-Saxon potential, which resembles a combination of the square well and simple harmonic oscilator is given by

$$V(r) = \frac{-V_0}{1 + exp\left[(r - R)/a\right]}, \tag{2.7}$$

where $V_0 \sim$ 50 MeV, $R = 1.25A^{1/3}$ and a is the diffuseness term that varies the sharpness of the transition between V_0 and 0; a typical value of this is 0.524 fm [27].

The Woods-Saxon potential is a realistic representation of the potential inside a nucleus, i.e. a constant potential inside the nucleus and a smooth transition to zero outside of the nucleus. The non-definite edge of the potential can be observed in electron scattering experiments [27]. This potential is sometimes referred to as the intermediate form as it incorporates useful parts of both the square well and harmonic oscillator potentials. Unlike the harmonic oscillator, the angular momentum degeneracy is lifted [30]. The calculated energy levels of the Woods-Saxon potential are shown in Figure 2.3.

Even in this relatively simple form the first energy gaps appear at nucleon numbers 2, 8 and 20. The final potential including the spin-orbit term is

$$V(r) = V_{WS} + V_{SO}(r)\vec{\ell} \cdot \vec{s}, \tag{2.8}$$

where quantum numbers ℓ and s are the orbital angular momentum and spin respectively and V_{SO} is the strength of the interaction between the two. After this well-known correction is applied the energy eigenvalues of quantum states, shown to the right of Figure 2.3, result. The energy eigenvalues of quantum states are labelled $[n,\ell,j]$, where n and j denote the principle quantum number and the total angular momentum respectively. This appears to be a good model for spherical nuclei as the large gaps at the observed magic numbers are well reproduced.

2.1.3 Collective Motion in Nuclei

Although the independent particle model works well with spherical nuclei, it fails to reproduce empirical observations of nuclei with many nucleons above closed shells. Many nuclei in the mid-shell region have been observed to undergo collective motion. Collectivity involves a large number of nucleons within a nucleus moving in a coherent manner. Collective excitations manifest themselves as either a vibration

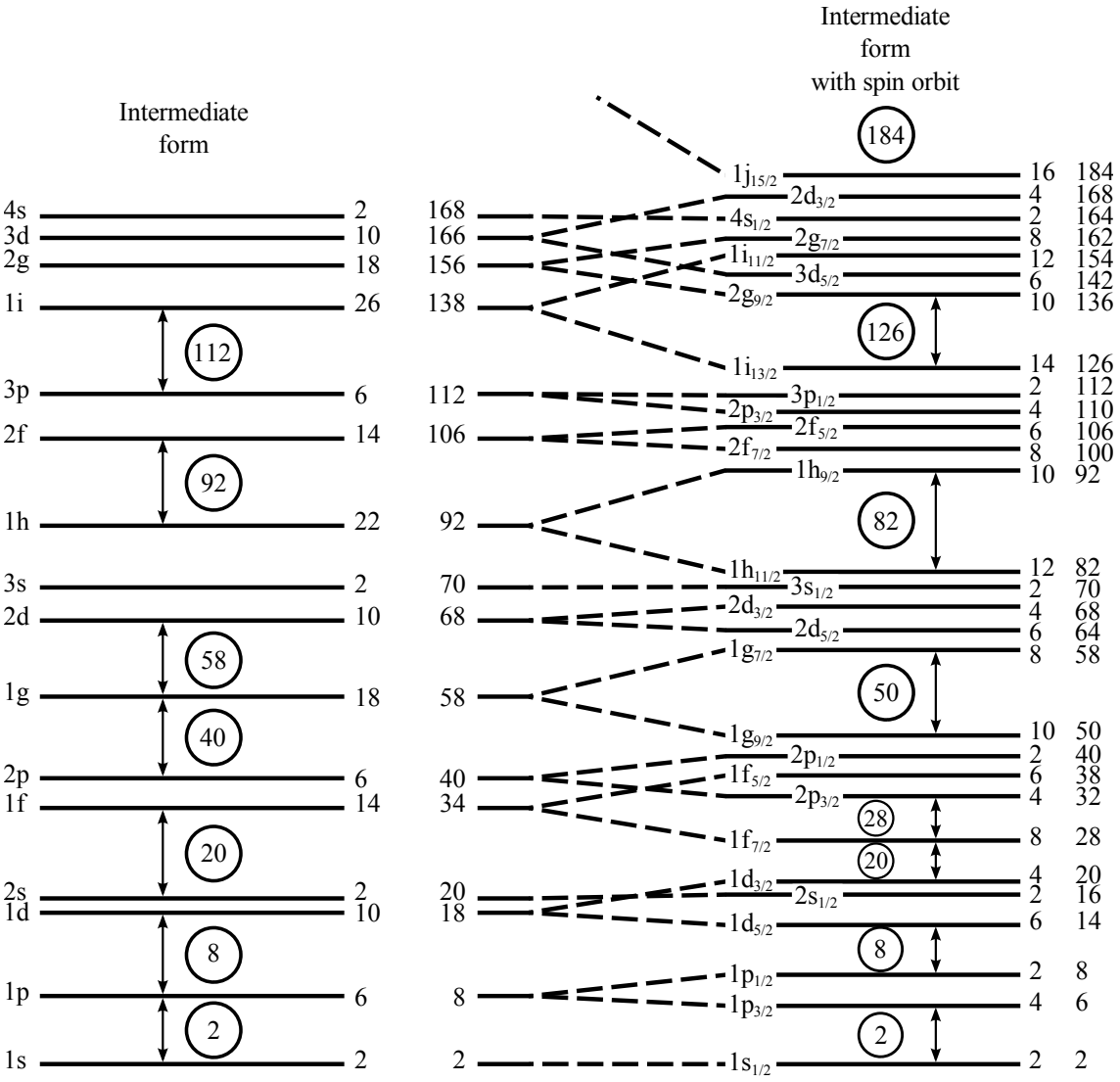

Figure 2.3: A pictoral representation of single particle energy eigenvalues using the Woods-Saxon potential before (left) and after (right) the spin-orbit term is introduced. The numbers to the right of the energy levels for both potential show the number of particles within each level and a sum of the particles up to and including that level, respectively.

or rotation of a nucleus.

Nuclear Vibrations

As rotations in spherical nuclei are quantum mechanically forbidden, even-even nuclei that lie close to magic numbers exhibit vibrational excitations. For nuclear

vibrations, the nucleus is described as a liquid drop that oscillates about an average spherical shape with radius $R_0 = 1.2A^{1/3}$. The radius of the nuclear surface of can be defined using spherical harmonics as

$$R(\theta, \phi) = R_0 \left[1 + \sum_{\mu} \alpha_{\lambda\mu} Y_{\lambda\mu}(\theta, \phi) \right] \tag{2.9}$$

where $\alpha_{\lambda\mu}$ is a time-dependent amplitude of the vibration and $Y_{\lambda}^{\mu}(\theta, \phi)$ is the spherical harmonic function of Euler angles ϕ and θ. The sum is performed over the range $-\lambda \leq \mu \leq +\lambda$ where μ is an integer and λ is the multipole order.

The value of λ determines the type of vibrational motion. Vibrational excitation quanta are called *phonons*, and carry angular momentum $\lambda\hbar$, energy $\hbar\omega$ and parity $(-1)^{\lambda}$. For a monopole vibration ($\lambda = 0$), the nucleus can be thought of expanding and contracting with a constant radius with respect to θ and ϕ. As nuclear matter is not easily compressible, these excitations require a very high energy and are not observed. The dipole vibrational mode ($\lambda = 1$) describes the nucleus oscillating around its equilibrium position; no internal force can cause such vibrations of the nucleus as a whole. Giant dipole resonances can occur, however, at very high energies.

The most common excitation mode arises from quadrupole phonons. In this case the nucleus oscillates between a spherical and quadrupole shape. The excitation requires no compressibility and only involves surface nucleons. One phonon coupled with an even-even nucleus gives the first excited state $J^{\pi} = 2^{+}$. The addition of a further phonon gives rise to degeneracy in angular momentum: in theory, the second excited state should take values of $J^{\pi} = 0^{+}, 2^{+}, 4^{+}$ with equal energy [27]. In reality the three states are perturbed by residual interactions and observed with closely lying, but different energies. Along with the observation of this triplet, another signature of vibrational nuclei is the energy ratio between the first and second excited state. According to this theory, the energy of the second excited state should be

exactly double that of the first, i.e. $E(4^+)/E(2^+)$=2. This is indeed the case in many nuclei and is compelling evidence of vibrational excitations in nuclei. Other more complicated vibrations are obtained by increasing the harmonic multipole. Several octupole vibrating nuclei have been observed. However, the probability of higher values of λ decreases rapidly after $\lambda = 3$.

Nuclear Rotations

As stated above, spherical nuclei are quantum mechanically forbidden to rotate. Rotational excitations are, however, allowed in deformed nuclei. Deformed nuclei with cylindrical symmetry have one axis, the *symmetry axis*, that is longer or shorter with respect to the other two. The surface of axially symmetric nuclei can be described by the formula

$$R(\theta, \phi) = R_0 \left[1 + \beta Y_{20}(\theta, \phi)\right] \tag{2.10}$$

where Y_{20} is again a quadrupole spherical harmonic function which is independent of ϕ. The deformation parameter β describes the magnitude of the deformation along the symmetry axis and is related to the eccentricity of the elliptical deformation by

$$\beta = \frac{4}{3}\sqrt{\frac{\pi}{5}}\frac{\Delta R}{R_0}, \tag{2.11}$$

where ΔR is the difference between the semi-major and semi-minor axis of the ellipse. By examination of Equation 2.10 it is apparent that three shapes can be described by β. When $\beta < 0$ the symmetry axis is contracted and Equation 2.10 describes an *oblate* spheroid, $\beta = 0$ describes a perfect sphere, and $\beta > 0$ elongates the symmetry axis resulting in a *prolate* spheroid. Due to the cylindrical symmetry, deformed nuclei must rotate around an axis perpendicular to the symmetry axis.

Nuclei of this form are found in the $150 < A < 190$ and $A > 220$ mass regions.

As with vibrational excitations, rotational excitations have a signature indicative of deformation. In a very simple case, the kinetic energy of a rotating object is given by $\frac{1}{2}\Im\omega^2$, where $\Im$ is the moment of inertia given by $\Im = mr^2$ and ω is the rotational frequency. Expressing the energy as a function of angular momentum, $L = \Im\omega$, yields $E = L^2/2\Im$. Replacing L^2 with the quantum mechanical value of ℓ^2 yields

$$E = \frac{\hbar^2}{2\Im} I(I+1) \tag{2.12}$$

where I is the angular momentum quantum number. As the moment of inertia is fixed for a rigid rotor, the rotational energy is only dependent on I, therefore to increase energy I is increased. Even-even nuclei are observed to have a ground-state of 0^+ with even spin levels built above it. Following from Equation 2.12, the energy ratio between the first few excited states in rotational even-even nuclei should therefore give a constant value; the theoretical values for the first $4^+/2^+$ and $6^+/2^+$ energy level ratios are 3.33 and 7 respectively. Indeed many rotational bands do exhibit these ratios giving strong evidence for the existence of this type of motion.

2.1.4 Deformed Shell Model (Nilsson Model)

It is possible to obtain the single-particle states in non-spherical nuclei by deforming the nuclear potential. The Hamiltonian of a system using a harmonic oscillator potential with quadrupole deformation ($z \neq x = y$) is given by

$$H = T + V = \frac{\mathbf{p}^2}{2m} + \frac{1}{2}m\left[\omega_{x,y}^2(x^2+y^2) + \omega_z^2 z^2\right] + \mathbf{l}\cdot\mathbf{s} + \mathbf{l}^2, \tag{2.13}$$

where $\mathbf{p}$ is the momentum operator and $\omega_{x,y,z}$ are the angular frequencies along their respective axes. Again the spin-orbit coupling and centrifugal corrections have been added to make a more realistic potential. Due to cylindrical symmetry, harmonic motion has the same angular frequency along the x and y axes in Equation 2.13.

The deformation of such a shape can be described by

$$\epsilon = \frac{\omega_{x,y} - \omega_z}{\omega_0} \tag{2.14}$$

where ω_0 is a constant if the nuclear volume remains constant. In analogy to the β parameter in the collective rotation description, the ϵ parameter defines the eccentricity of the elliptical cross section of the nucleus (x-z plane or y-z plane). For spherical nuclei ϵ=0, for oblate shapes $\epsilon < 0$ and for prolate shapes $\epsilon > 0$.

A non-zero value of ϵ lifts the angular momentum degeneracy, there is a further splitting of the energy levels on the right hand side of Figure 2.3, and ℓ is no longer a good quantum number. For prolate nuclei, the energy eigenvalues are lowered when the projection of j on the symmetry axis, Ω, is low. Conversely the energy eigenvalues for high values of Ω are increased. The opposite is true for oblate nuclei. In general, the separation of the eigenvalues is increased with increasing deformation. Unlike the independent particle model, the major shell, N, is defined by the sum of the quanta along each axis ($N = n_x + x_y + x_z$). It is also necessary to define the projections of ℓ and s on the symmetry axis as Λ and Σ, respectively. With these formalisms it is possible to label single particle orbitals as $[Nn_z\Lambda]\Omega^\pi$ where the parity, π, is again equal to $(-1)^\pi$. A maximum of two nucleons of the same kind can occupy each energy level due to the spin degeneracy.

As with the independent single particle model, the energy eigenvalues can also be extracted using a Woods-Saxon potential. In this case, however, the potential is again deformed in one direction. This potential yields similar results to the modified oscillator potential, and will not be discussed further in this thesis.

2.2 Alpha Emission

Ever since its discovery by Bequerel in 1896, alpha decay has played a major role in probing nuclear structure phenomena. Many heavy nuclei decay via alpha emission. Of these nuclei that are β^+ unstable a very large portion lie beyond the $N = 82$ shell gap. This two body decay process can be represented by the formula,

$$ {}^{A}_{Z}X_N \rightarrow {}^{A-4}_{Z-2}X'_{N-2} + \alpha \tag{2.15} $$

where X and X' are the mother and daughter nucleus respectively, and α is the nucleus of a ^{4}He atom. For the purpose of this chapter, the mass superscript of helium is dropped and always taken as 4. Many things can be learned from alpha decay observations, including ground-state decay energies and mass excess values, isomer decay energies, spin assignments of decaying states, information on parent and daughter states from spectroscopic or hindrance factors, isotopic assignment based on mother-daughter correlations (see Chapter 4), gamma-ray assignments through alpha tagging and Q-value systematics [31]. Alpha decay is prevalent in heavy nuclei because the alpha particle is very tightly bound, which means that compared to other decay modes alpha decay is best at reducing the mass of the system. In this section a simple theoretical background of the alpha decay process will be described.

2.2.1 Alpha-decay Q-value

If an alpha decay is energetically possible, it will occur in nature. This condition is met when the energy released in the reaction, the Q-value (Q_α), is positive. The energy released in a decay reaction is given by the difference in mass between the mother atom (M_m) and the decay products, in this case the α particle (M_{He}) and

the daughter atom (M_d):

$$Q_\alpha = (M_m - M_d - M_{He})c^2. \tag{2.16}$$

The mass of the helium *atom* is used in Equation 2.16 to account for the masses of the electrons. In experimental nuclear physics, spectra are usually calibrated using the kinetic energies of observed nuclei. To calculate the Q-value of the decay, the kinetic energy of the recoiling mother nucleus must also be included. Conservation of momentum leads to

$$m_\alpha \nu_\alpha = m_r \nu_r \quad \text{thus} \quad \nu_r = \frac{m_\alpha \nu_\alpha}{m_r}, \tag{2.17}$$

where $m_{\alpha,r}$ and $\nu_{\alpha,r}$ are the masses and velocities of the α particle and recoiling nucleus respectively. The total energy for an alpha decay can be therefore written as

$$Q_\alpha = E_\alpha + E_r = E_\alpha + \frac{1}{2} m_r \left(\frac{m_\alpha \nu_\alpha}{m_r} \right)^2 \approx E_\alpha \left(1 + \frac{4}{A_d} \right), \tag{2.18}$$

where A_d is the mass number of the daughter nucleus, and the mass number of alpha particle is 4. These formulae can be used to calculate the mass of the mother (daughter) nucleus from the alpha-decay energy, provided the mass of the daughter (mother) nucleus is known.

A further correction to the Q-value must be applied to correct for the *cloud* of electrons surrounding the decaying nucleus. The electron cloud has two effects: before alpha decay the Coulomb barrier is slightly reduced, after decay the alpha particle loses energy whilst traversing the cloud. The former effect is neglected in this discussion but is accounted for in Ref. [32]. The latter effect is accounted for

by the screening correction given by

$$E_{sc} = (65.3Z^{7/5} - 80Z^{2/5}) \text{ (eV)} \tag{2.19}$$

where Z is the charge of the daughter nucleus [1]. The alpha decay Q-value of a bare nucleus (without electrons) is therefore given by

$$Q_{\alpha}^{bare} = Q_{\alpha} + E_{sc}. \tag{2.20}$$

Provided $Q_{\alpha} > 0$ the nucleus can spontaneously alpha decay, although the probability of the alpha decay is strongly dependent on Q_{α} and the rate of decay only becomes detectable at a few MeV. The decay rate is related to the half-life, $t_{1/2}$, as

$$\lambda = \frac{ln\ 2}{t_{1/2}}. \tag{2.21}$$

If a nucleus has two different decaying states their, partial half-lives, $\tau_{1/2_i}$, and partial decay constants, λ_i, are related to the branching ratio, b_{α_i}, by the equation

$$\tau_{1/2_i} = \frac{ln\ 2}{\lambda_i} = \frac{t_{1/2}}{b_{\alpha_i}}. \tag{2.22}$$

As stated above, the half life of a decay is strongly dependent on the disintegration energy, and a small change in alpha-decay energy can give rise to a difference of multiple orders of magnitude in the half-life. As a result the range of alpha decay half lives is over 30 orders of magnitude. Geiger and Nuttall [33] performed an experiment where they measured the stopping distance of alpha particles in air. It was found that the decay constant plotted against the stopping distance of several isotopes gives a reasonably straight line. As the range is related to the energy of

the alpha particle, the following statement can be made:

$$\tau_{1/2_i} \approx a + \frac{b}{\sqrt{Q_\alpha}}, \tag{2.23}$$

where a and b are empirically measured constants and are different for each element.

2.2.2 Theory of α Emission

The theory of alpha decay requires a non-classical approach to the problem. The first successful model describing the alpha decay process was given by Gamow who was closely followed by Gurney and Condon. These models describe alpha decay as a one body problem, consisting of a preformed alpha particle existing within the potential of the daughter nucleus. The preformed alpha moves in a spherical potential well ($V(r)$) of depth $-V_0$ with energy $+Q_\alpha^{bare}$. Classically, the alpha particle cannot penetrate the barrier and is bound in the potential. However, quantum mechanics states that there is a probability, P, of tunneling through the potential between the classical turning points R_0 and R_i shown in Figure 2.4. The probability is approximated by applying the WKB-integral [34] of the classical forbidden region between points R_0 and R_i[1],

$$P = \exp\left\{-2\int_{R_i}^{R_o} \frac{(2\mu)^{1/2}}{\hbar}\left[V(r) - Q_\alpha^{bare}\right]^{1/2} dr\right\} \tag{2.24}$$

where μ is the reduced mass given by

$$\mu = \frac{M_{He}M_d}{M_{He}+M_d} \approx \frac{4A_d}{4+A_d}m_u \tag{2.25}$$

where m_u is the atomic mass unit.

For the purpose of this study, the potential postulated by Igo was used as the

[1]The integration part is often referred to as the Gamow factor

nuclear potential [35] given by

$$V_{\text{Igo}} = -1100 \ \exp\left\{-\left[\frac{r - 1.17A^{1/3}}{0.574}\right]\right\} \ (\text{MeV}), \tag{2.26}$$

where r is the radius in fm. The total potential is the sum of the nuclear, Coulomb and centrifugal barriers and is given by

$$V(r) = -1100 \ exp\left\{-\left[\frac{r - 1.17A^{1/3}}{0.574}\right]\right\} + \ell(\ell+1)\frac{\hbar^2}{2mr^2} + \frac{zZe^2}{4\pi\epsilon_0 r} \ (\text{MeV}), \tag{2.27}$$

where ϵ_0 is the permittivity of free space. The shape of the total potential and its constituents can be seen in Figure 2.4. Also shown in this figure is the varying barrier height with angular momentum. Angular momentum and parity must be conserved in an alpha transition therefore

$$\vec{\ell} = \vec{I_i} - \vec{I_f}. \tag{2.28}$$

This yields the selection rule

$$|I_i^\pi - I_f^\pi| \leq \ell \leq |I_i^\pi + I_f^\pi| \quad \text{where} \tag{2.29}$$

$$\pi_f = \pi_i(-1)^\ell \quad \text{and} \quad \pi_i = (-1)^L, \tag{2.30}$$

where L is the orbital angular momentum of the initial state. The classical inner turning point R_0 is calculated by a simple iterative process in which the difference between the potential of choice and the Q-value is reduced to zero. The outer turning point is found by setting the Igo potential to zero and solving the quadratic equation. The integration part of Equation 2.24 is found using the method of Rasmussen [34], which uses numerical integration and gives a good approximation of the area of the

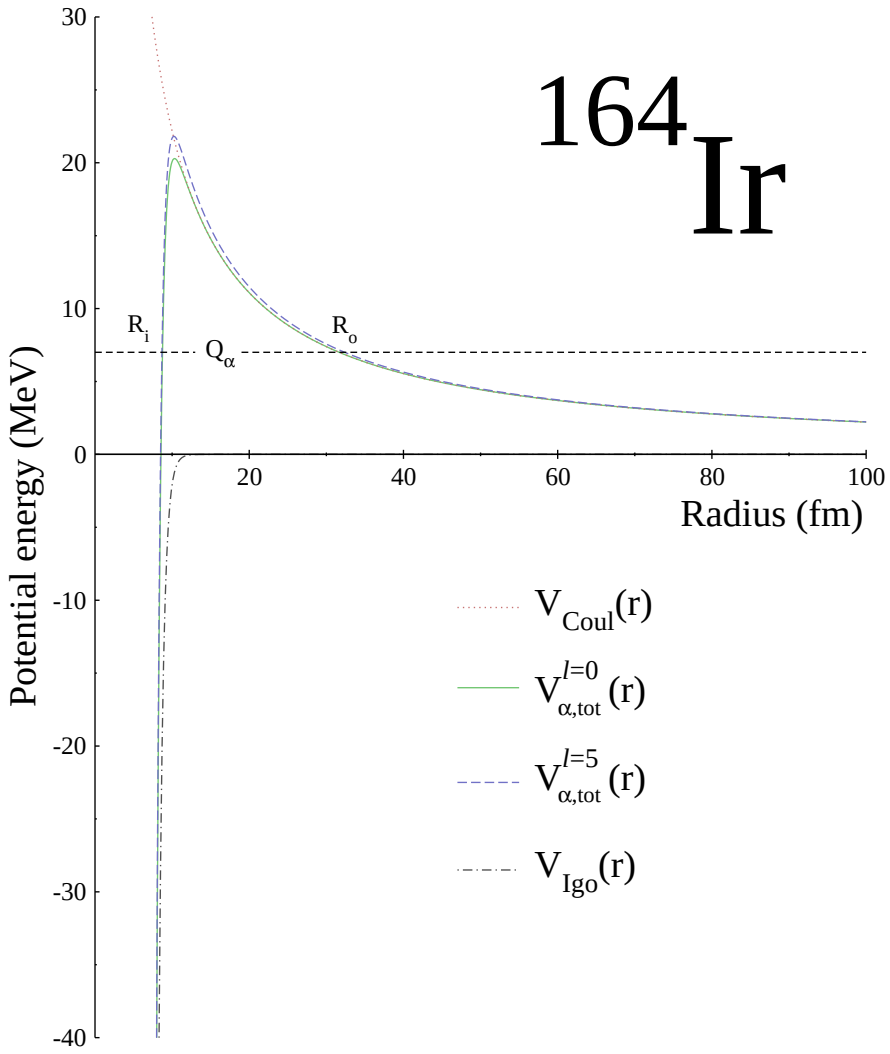

Figure 2.4: Coulomb, Igo and Centrifugal potentials experienced by a preformed alpha particle within the daughter nucleus of ^{164}Ir. The total barrier height for $\ell = 0$ and $\ell = 5$ are also shown.

classically forbidden region[2]. Using the total kinetic energy of the preformed alpha particle, $(V_0 + Q_\alpha)$, the calculated decay constant can be expressed as

$$\lambda_{calc} = (\nu_\alpha / 2R_i) \cdot P = f \cdot P. \tag{2.31}$$

[2]The method of Rasmussen uses a modified version of Simpson's rule to integrate numerically.

In this equation, the *knocking frequency*, f, is the frequency in which the preformed alpha particle hits the Coulomb barrier at radius R_i.

A comparison of theoretical values gained in either Equations 2.31 or 2.23 with experimental data can yield nuclear structure information about the mother nucleus. Large deviations from theoretical values can indicate a change in nuclear stucture between the mother and daughter nucleus. A commonly used value to measure the deviation from theory is the hindrance factor, defined as

$$HF = \frac{t_{1/2}^{exp}}{t_{1/2}^{calc}}. \tag{2.32}$$

Alpha decays can be thought of as *hindered* or *unhindered*. In the one-body picture, a hindered decay can be thought of as requiring a rearrangement of nucleons before emission of an alpha particle carrying angular momentum, making the decay slower than expected. An unhindered alpha decay requires no rearrangement of nucleons and has a low hindrance factor, generally less than four. For decays where $\ell > 0$ the hindrance factor is increased ($HF > 4$). A large hindrance factor therefore is indicative of a change in angular momentum from the mother and daughter states.

Another commonly used quantitative description of this process is the reduced alpha-decay width, also known as the spectroscopic factor or preformation probability. A high preformation probability is indicative of no rearrangement of nucleons, conversly, a low preformation probability is indicative of a change in angular momentum. The reduced alpha-decay is defined as

$$\delta^2 = \frac{\lambda_{exp} h}{P}(\text{eV}). \tag{2.33}$$

Where P is the penetration probability and λ_{exp} is the measured decay constant. Typical values for hindered and unhindered decays are $\sim$ 1 keV and $>$ 40 keV respectively. The nucleus of ^{212}Po can be described as the doubly magic ^{208}Pb

nucleus containing an alpha particle. The alpha decay of this nucleus is therefore the best example of a preformed alpha particle and decay widths are often represented as normalisations relative to this decay.

2.3 Proton Radioactivity

Proton emission can be expressed by the formula,

$$ {}^{A}_{Z}X_{N} \rightarrow {}^{A-1}_{Z-1}X'_{N} + p \tag{2.34} $$

As previously stated, a negative separation energy of the last proton is required for proton emission to occur, i.e. the binding energy of the daughter nucleus must be higher than mother nucleus. The point at which this condition is fulfilled is called the proton dripline. The pairing interaction increases the binding energy of even-Z nuclei by coupling the spins of nucleon pairs to zero. Odd-Z nuclei therefore become subject to proton radioactivity at higher N than their even-Z neighbours. In fact no even Z proton emitters are observed in the region $Z < 82 < N$. This results in a staggering of the proton drip line which is accounted for in Equation 2.2 by the pairing term.

In analogy to alpha decay (see Equation 2.16), the proton emission Q-value can be expressed using the mass of the mother, daughter and hydrogen (M_H) atoms as

$$ Q = (M_m - M_d - M_H)\, c^2. \tag{2.35} $$

This is the inverse of Equation 2.4. Again a correction to the measured kinetic energy, E_p, of the proton decay must be applied to calculate the Q-value. This is

given by

$$Q_p^{bare} = Q_p + E_{sc} = E_p \left(1 + \frac{M_H}{M_d}\right) + E_{sc} \approx E_p \left(1 + \frac{1}{A_d}\right) + E_{sc}, \tag{2.36}$$

where in this case the screening correction energy, E_{sc}, accounts for the energy lost to balance the different binding energies of the mother and daughter atoms [31]. These binding energies can be calculated from values taken from Table 1 of Ref. [36] using the equation

$$E_{sc} = B_m - B_d, \tag{2.37}$$

where B_m and B_d are the total electron binding energies of the mother and daughter atoms respectively.

A proton moving inside a nucleus experiences a Coulomb barrier roughly half the size of that which an alpha particle experiences. The angular momentum barrier is however increased four-fold due to the inverse dependence on mass. Because of this, the height of the barrier, and thus the half-life of the decay, is extremely sensitive to changes in the angular momentum of the emitted proton. The selection rules for proton decay between the initial state I_i and the final state I_f are

$$|I_i^\pi - I_f^\pi| \pm \tfrac{1}{2} \leq \ell \leq |I_i^\pi + I_f^\pi| \pm \tfrac{1}{2} \quad \text{where} \tag{2.38}$$

$$\pi_f = \pi_i (-1)^\ell, \tag{2.39}$$

where ℓ is the orbital angular momentum taken away from the nucleus by the proton. The high sensitivity to changes in angular momentum mean that spectroscopic information about the mother and daughter nuclei can be measured directly by comparing measured half-lives and branching ratios with theory. Unlike alpha decay, no preformation must be considered, which makes the study of proton decays very appealing.

2.3.1 Simple Theoretical Model of Proton Emission From Spherical Nuclei

A similar approach to alpha decay can be taken to describe proton emission. Firstly decay rate is defined as

$$\lambda = \frac{ln\ 2}{t_{1/2}} = f \cdot P. \tag{2.40}$$

Instead of calculating the knocking frequency from the Q-value of the decay, it is defined as

$$f = \frac{\sqrt{2}\pi^2\hbar^2}{m^{3/2}R_c^3(zZe^2/R_c - Q_p^{bare})^{1/2}}. \tag{2.41}$$

All relevant constants are listed below. This equation is analogous to the expression obtained by Bethe [37] and Rasmussen [38] for alpha-decay rates of spherical nuclei. The WKB approximation is applied to integrate over the classically forbidden area between the inner and outer turning points to obtain an expression for penetration probability. In analogy to Equation 2.24, the penetration probability is given by

$$P = \exp\left\{-2\int_{R_i}^{R_o} \frac{(2m)^{1/2}}{\hbar}\left[V_{j\ell}(r) + V_{Coul}(r) + V_\ell(r) - Q_p^{bare}\right]^{1/2} dr\right\}. \tag{2.42}$$

The nuclear potential, $V_{j\ell}$, is in this case taken from the real part of the optical model given by Bechetti and Greenlees [39]. The centrifugal, Coulomb and nuclear potentials experienced by the inside the daughter nucleus and their superposition are shown Figure 2.5.

The relevent formulae and constants for Figure 2.5, and Equations 2.41 and 2.42 are listed below in Equations 2.43 to 2.50.

$$V_{j\ell} = -V_R f(r, R_R, a_R) + V_{SO}\lambda_\pi^2\ \bar{\sigma}\cdot\bar{\ell}\left(\frac{1}{r}\right)\left(\frac{d}{dr}\right)[f(r, R_{SO}, A_{SO})] \quad \text{[MeV]} \tag{2.43}$$

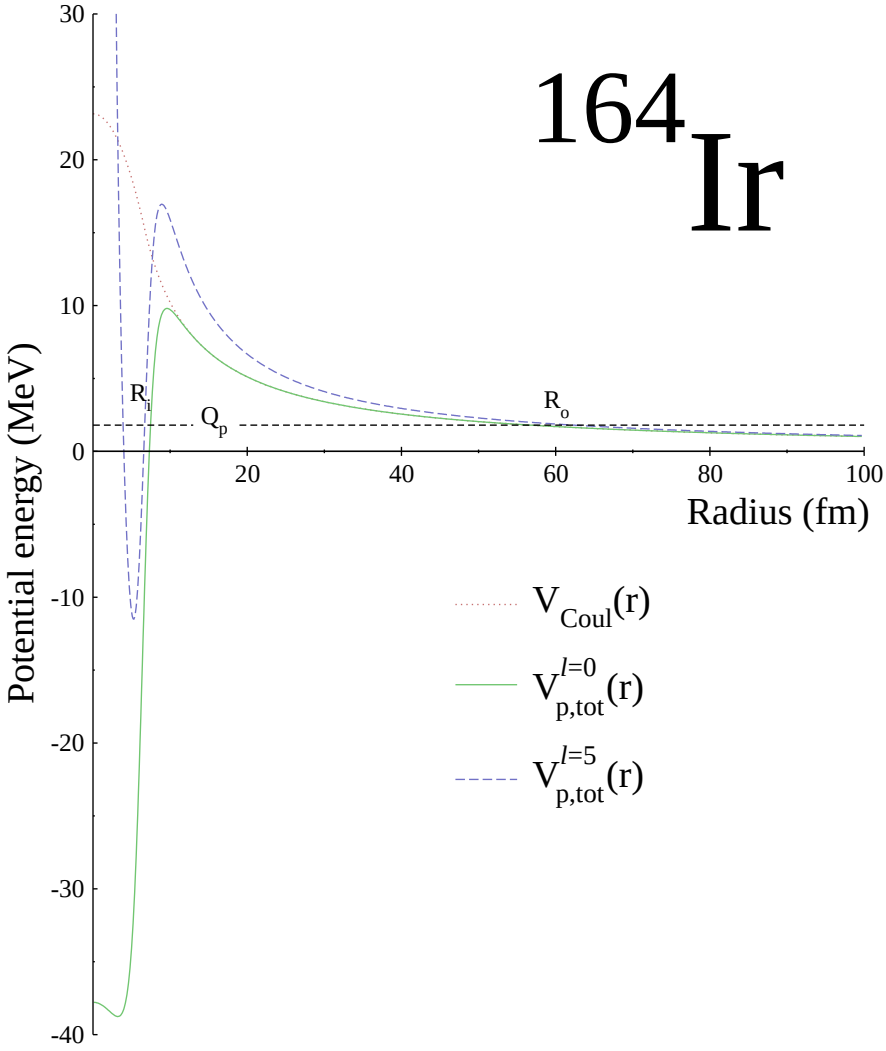

Figure 2.5: The potentials experienced by a proton moving within the daughter nucleus. Equations 2.43 to 2.50 have been used to draw these functions. The dramatic difference in potential height for $\ell = 0$ and $\ell = 5$ can be seen. R_i and R_o indicate the inner and outer classical turning points

$$V_R = 54.0 - 0.32E_p + 0.4\frac{Z}{A^{\frac{1}{3}}} + 24.0\left(\frac{N-Z}{A}\right) \quad \text{[MeV]} \tag{2.44}$$

$$V_C(r) = \frac{zZe^2}{4\pi\epsilon_0 2R_C}\left(3 - \frac{r^2}{R_C^2}\right) \text{ [MeV]} \quad \text{for} \quad r \leq R_C \tag{2.45}$$

$$V_C(r) = \frac{zZe^2}{4\pi\epsilon_0 r} \text{ [MeV]} \quad \text{for} \quad r > R_C \tag{2.46}$$

$$V_\ell(r) = \ell(\ell+1)\frac{\hbar}{2mr^2} \tag{2.47}$$

$$\text{where} \quad \bar{\sigma}\cdot\bar{\ell} = \ell \quad \text{for} \quad j = \ell + \frac{1}{2} \tag{2.48}$$

$$\text{and} \quad \bar{\sigma}\cdot\bar{\ell} = -(\ell+1) \quad \text{for} \quad j = \ell - \frac{1}{2} > 0 \tag{2.49}$$

$$f(r,R,a) = \frac{1}{1+\exp\left(\frac{r-R}{a}\right))} \tag{2.50}$$

z, Z = charge number of proton and daughter nucleus

N = neutron number of daughter nucleus

A = mass number of daughter nucleus

$R_R = 1.17A^{\frac{1}{3}}$ fm, $a_R = 0.75$ fm

$R_{SO} = 1.01A^{\frac{1}{3}}$ fm, $a_{SO} = 0.75$ fm, $V_{SO} = 6.2$ MeV

$R_{SO} = 1.21A^{\frac{1}{3}}$ fm

$m \approx$ [A/(A+1)]m_u = reduced mass

$m_u = 938.501$ MeV/c^2

λ_π^2 = pion Compton wavelength squared ≈ 2.0 fm^2

It can be seen in the above equations, that small variations in ℓ have a large influence on the penetration probability. This is shown in Figure 2.5 as the classically forbidden area is dramatically increased when increasing ℓ from 0 to 5. Like in the case of alpha decay, the lowering of the Coulomb potential due to the electron cloud is neglected.

2.3.2 Spectroscopic Factor

In analogy to the hindrance factor for alpha decay, deviations from theory because of changes in nuclear structure can be quantified by the spectroscopic factor (or reduced width). The experimental spectroscopic factor can be calculated using the

formula

$$S_{exp} = \frac{\lambda_{\rm exp}}{fP} = \frac{t_{1/2}^{calc}}{t_{1/2}^{exp}}, \tag{2.51}$$

where $t_{1/2}^{calc}$ is the calculated half life from the WKB approximation of the model described above. This model does not take in to account the overlap of the mother and daughter nuclear wavefunctions that effect the probability of proton emission. In a paper by Davids *et al.* [40], a low-seniority shell-model is proposed to calculate the theoretical spectroscopic factors of nuclei lying in the region $64 < Z < 82$. In this paper the spectroscopic factor is defined as the overlap of mother and daughter wave functions and is reduced to

$$S_{calc} = \frac{p}{9} \quad \text{for} \quad 1 \leq p \leq 9 \tag{2.52}$$

where p is the number of proton-hole pairs in the daughter nucleus. This calculation accounts for when the occupied levels of the mother nucleus are different to that of the daughter. For example, the parent state may be based on a hole in a particular orbital and the daughter nucleus may have this oribital filled. The probability of this occuring decreases with the increasing number of proton-hole pairs available in the $s_{1/2}$, $d_{3/2}$ and $h_{11/2}$ orbitals. Therefore the spectroscopic factor increases with decreasing Z. An obvious consequence of this model is that half lives should be consistently less than those predicted by the WKB approximation. These theoretical calculations agree well with experimental measurements and will be discussed later in the results chapter.

2.3.3 Gamma-ray Transitions

An excited nucleus loses energy via electromagnetic or particle emission. In most cases gamma-ray emission is favoured as it requires the smallest rearrangement of nucleons, because of this lifetimes of excited states tend to be very short ($< 10^{-15}$ s).

L	T_E (s)	T_M (s)
1	$6.73\ A^{-2/3}\ E_\gamma^{-3} \times 10^{-15}$	$2.24\ A^{0}\ E_\gamma^{-3} \times 10^{-14}$
2	$9.37\ A^{-4/3}\ E_\gamma^{-5} \times 10^{-9}$	$3.12\ A^{-2/3}\ E_\gamma^{-5} \times 10^{-8}$
3	$1.98\ A^{-2}\ E_\gamma^{-7} \times 10^{-2}$	$6.60\ A^{-4/3}\ E_\gamma^{-7} \times 10^{-2}$
4	$6.30\ A^{-8/3}\ E_\gamma^{-9} \times 10^{4}$	$2.10\ A^{-2}\ E_\gamma^{-9} \times 10^{5}$
5	$2.83\ A^{-10/3}\ E\gamma^{-11} \times 10^{11}$	$9.43\ A^{-8/3}\ E_\gamma^{-11} \times 10^{11}$

Table 2.1: Half-lives based on Weisskopf estimates for electric and magnetic transitions for the first five orders of multipolarity [26], where A is the mass number and E_γ is the γ-ray energy in MeV.

Lifetimes of excited states where a large rearrangement of nucleons is needed for de-excitation are longer. These states are often referred to as isomeric states; in these cases, particle emission can compete. A study of these discrete excited states gives information on the structure of the nucleus.

For γ-ray energy $E_\gamma < 5$ MeV, the kinetic energy of a recoiling nucleus is negligible and the energy difference between the initial and final state is taken to be equal to the γ-ray energy. Gamma-ray transitions from the initial state I_i to final state I_f follow the selection rules

$$|I_i^\pi - I_f^\pi| \leq L \leq I_i^\pi + I_f^\pi \tag{2.53}$$

$$\Delta\pi(EL) = (-1)^L \quad \text{and} \quad \Delta\pi(ML) = (-1)^{L+1}, \tag{2.54}$$

where EL and ML denote electric and magnetic multipoles, respectively. Although Equation 2.29 presents several ℓ values for a given transition, of which the lower values are favoured. Transitions probabilities due to single-proton excitations are estimated by Weisskopf in Ref. [41]. The equations for estimated half-lives using Weisskopf estimates are given in Table 2.1

It is important to note that Weisskopf estimates are based on a very simplified model, and only give a good indication on the relative half-lives of the transitions (and therefore transition rates).

Chapter 3

Experimental Apparatus

3.1 Fusion Evaporation Reactions

To gain understanding of states in nuclei which are not naturally occuring, a suitable reaction must be chosen to examine different regions of the nuclear chart. Several techniques are employed to probe different parts of the chart of nuclides including transfer, projectile-fragmentation, deep inelastic scattering and in the case of the present study, fusion-evaporation reactions. Fusion-evaporation reactions involve a projectile nucleus P fusing with a stationary target nucleus T, the resulting compound nucleus C is highly excited due to the large energy of the projectile needed to overcome the coulomb barrier of the target nucleus. A fusion-evaporation reaction may be expressed by

$$ {}^{A_1}_{Z_1}P + {}^{A_2}_{Z_2}T \rightarrow {}^{A_1+A_2}_{Z_1+Z_2}C^*, \tag{3.1} $$

where A and Z are the mass number and proton number respectively. The excited compound nucleus may then evaporate protons, neutrons and alpha particles in order to reduce its angular momemtum and energy. This happens within a time

scale of the order 10^{-19} s. The fusion evaporation process can be expressed by

$$^{A_1+A_2}_{Z_1+Z_2}C^* \rightarrow \ ^{A_C-(x+y+4z)}_{Z_C-(x+2z)}R + xp + yn + z\alpha, \tag{3.2}$$

where $A_C = A_1 + A_2$ and $Z_C = Z_1 + Z_2$, or in the more compact and conventional form

$$^{A_1}_{Z_1}T(^{A_2}_{Z_2}P, xpynz\alpha)^{A_3}_{Z_3}R, \tag{3.3}$$

where xp is the number of protons evaporated, yn is the number of neutrons evaporated, $z\alpha$ is the number of alpha particles evaporated, and R is the resulting evaporation residue (recoil). In fusion evaporation reactions the energy of the impinging beam, the angular momemtum and the excitation energy of the compound nucleus are among many factors that determine how many particles are evaporated. Figure 3.1 is a schematic of two decay paths from a compound nucleus passing the particle evaporation threshold at different energies. As protons are more loosely bound than neutrons in neutron deficient nuclei, proton evaporation is favoured. Evaporated protons take ∼2 MeV of energy (separation energy) and ∼1 $\hbar$ of angular momentum. The yrast line shows the minimum energy needed for a given nuclear angular momentum. The dashed line shows the limit where particle evaporation is no longer possible, after this has passed the nucleus must then decay by gamma radiation. As the separation energy is higher for neutrons the evaporation limit varies for different particle evaporation channels, therefore different evaporation channels will yield different spins.

The energy of the compound nucleus is defined by

$$E^* = K_{cm} + Q = \frac{1}{2}\mu v_{rel}^2 + (M_P + M_T - M_C)c^2 \tag{3.4}$$

Where the $\mu = (M_T M_P)/M_C$ is the reduced mass, K_{cm} is the centre of mass

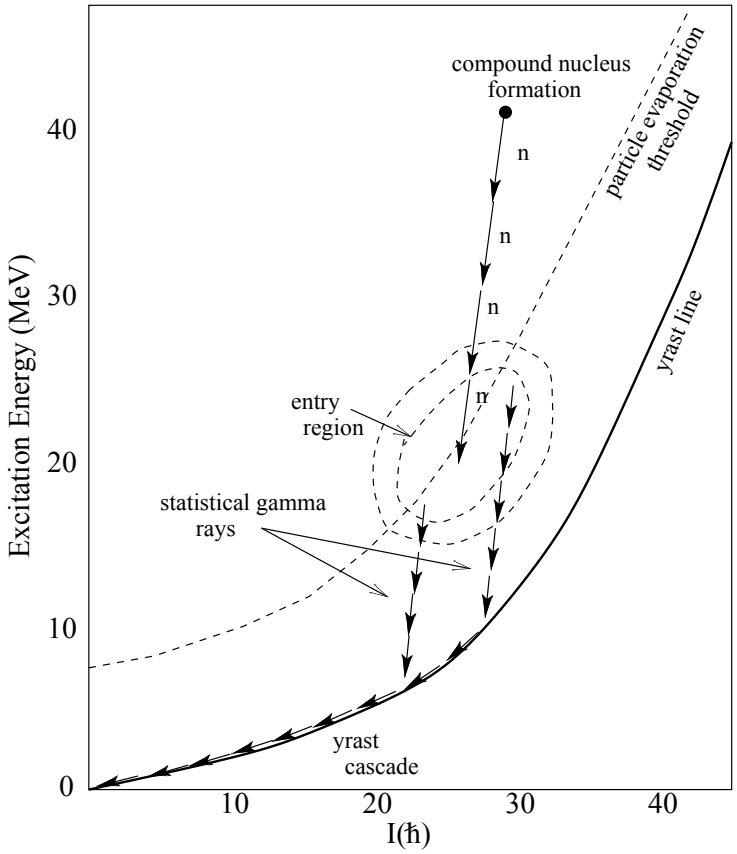

Figure 3.1: A schematic of a four particle channel fusion-evaporation reaction. Once the particle-evaporation threshold is reached, angular momentum and energy are lost via statistical gamma-rays. Image taken from Ref. [1]

kinetic energy, Q is the energy gained from the mass difference, $M_{P,T,C}$ are the projectile, target and compound nucleus mass respectively, and v_{rel} is the relative velocity. As the target is stationary, the formula can be re-written as

$$E^* = K_{cm} + Q = \frac{M_T}{M_P + M_T} K_P + (M_P + M_T - M_C)c^2 \tag{3.5}$$

Where K_P is the kinetic energy of the energy of the projectile nucleus. Using this energy, Monte Carlo simulations can be performed to give an idication of the cross sections of nuclei being produced. The energy of the beam is then is chosen to populate the desired nuclei. It is possible to select a beam energy to populate high or low spin states depending on the experiment [42].

3.2 Semiconductor Detectors

A semiconductor is a material that posesses properties of an intermediate between an insulator and a conductor; at T=0 K a semiconductor acts as an insulator, i.e. all electrons occupy the valence band and none exist in the conduction band, however, when T > 0 K the energy gap is sufficiently small to allow thermal excitations of electrons into the conduction band and act as a conductor. An elemental semiconductor is a material composed of one element that pertains to group IV of the periodic table such as Ge and Si. In such lattices, all electrons are shared with the neighbouring atom. When thermal excitations across the band gap occur, a vacancy, known as a hole, is left in the valence band. The relative movement of electrons to fill that vacancy makes the positive charge of the hole appear to migrate. The result is a migrating hole and a free electron, the material becomes conductive.

The conductivity of the material can be altered by adding *dopants* to it. Dopants from either groups III or V of the periodic table serve to increase the number of holes or free electrons in a lattice, respectively. Group V dopants such as phosphorous

(P), arsenic (As) and antimony (Sb) have 5 valence electrons, 4 of which are shared with neighbouring atoms in the lattice, leaving 1 electron at an energy level very close to the conduction band (donor state). The electron leaves the donor atom leaving it with a positive charge. Materials that contain these materials are known as n-type because of the excess negative charge.

Group III dopants such as boron (B), aluminium (Al), indium (In) and gallium (Ga) have 3 valence electrons. When placed in a group IV lattice, all 3 of the electrons make covalent bonds, leaving 1 vacancy for electrons of neighbouring atoms to fill. The energy level of this acceptor level is just above that of the valence band in the group IV (Ge, Si) atom, and excited states that leave the valence band are accepted in the vacancy. The vacancy in the parent group IV atom is replaced by a neighbouring atom; hole migration results. The acceptor atom is then ionized with a negative charge. Materials that contain these materials are known as p-type because of the excess positive charge.

When a n-type material comes in contact with an p-type material the donor electrons from the n-type material diffuse across the junction and fill the holes. The acceptor atoms that lie in the vicinity of the junction gain an electron and become negatively charged, conversely, the donor atoms lose an electron and become positively charged. Eventually, the electric field between the junction stops the diffusion. This region is called the *depletion region*. The depletion region can be increased by applying a reverse bias. This involves applying a negative potential to the p side thus increasing the natural potential already present. The junction then acts as a diode, allowing free charge to flow in one direction and stopping any flow in the other direction.

When radiation is incident on a detector, many electron-hole pairs are created in the depletion region. The negative-charge carriers (electrons) move toward the anode and the positive charge carriers (holes) move toward on the cathode. The

kinetic energy of the electron-hole pairs are independent of the energy of the incident radiation, therefore only the number of electron-hole pairs liberated is proportional to energy of the incident radiation and is output as a pulse.

3.3 Preamplification

The charge signal that is output from the detector is very small. Before proceeding with any pulse shape processing, the charge pulse must be preamplified. The most common method of preamplification in nuclear spectroscopy is to use a charge-sensitive pre-amplifier. A basic example of a charge sensitive pre-amp circuit is shown in Figure 3.2. The sudden presence of charge in the left-hand side of the

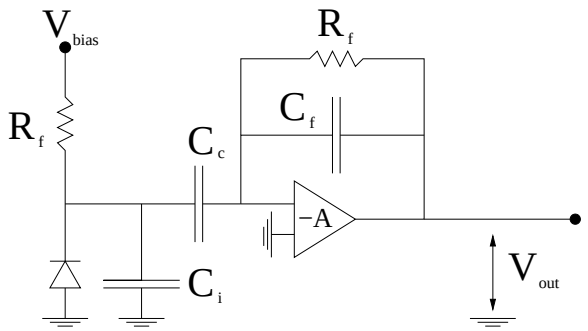

Figure 3.2: A circuit diagram of a basic charge-sensitive preamplifier. The diode symbol represents the detector. The detector bias and feedback resistor are labelled V_{bias} and R_f, respectively. The coupling capacitor and feedback capacitor are labelled C_c and C_f, respectively. The intrinsic capacitance of the detector is represented by C_i.

coupling capacitor induces a voltage across the feedback capacitor, and in turn a voltage pulse in the operational amplifier. The feedback capacitor discharges across the feedback resistor until the voltage returns to baseline. The time constant of the feedback is given by $\tau = R_f C_f$. The voltage across C_f will decay immediately, τ must therefore be much greater than the charge collection time (rise time) in order to collect maximum liberated charge on C_c before the decay of C_f. The total charge collection time is dependent on the height of the voltage pulse, this will be discussed

in later chapters.

3.4 Digital electronics

The pulse from the preamplifier is then processed by analogue-to-digital converters (ADCs) where the height of the pulse is extracted. For results discussed in chapter 6, some of the detectors were instrumented using Lyrtech digital electronics. An advantage of digital electronics is that a discrete representation of signals from the preamplifiers can be stored. These stored pulses are called traces. A buffer containing the ADC sample data consisted of 1016 samples, each 16 bits in size. Along with a 64 bit header (a 32 bit timestamp plus 32 bits for channel and event type information) this gives an event size of 2040 bytes. Each sample is 10 ns long, giving a total sample length of 10160 ns. The dead time of the electronics matched that of the sample length.

3.5 Experimental Apparatus

Nuclei populated via fusion-evaporations reaction immediately radiate gamma rays to reduce their energy and spin. Subsequent particle decays at the focal plane are correlated with the prompt gamma rays which impart physical information. With recoil rates of the order of kilohertz, it is a great challenge to correlate gamma radiation with a particular nucleus. Several sophisticated steps must therefore be taken in order to *tag* an isotope and observe the gamma rays emitted as it decays to its ground state. All experimental data for the present study were aquired at the Accelerator Laboratory of the University of Jyväskylä.

3.5.1 Jurogam

γ-ray detection

In high-resolution gamma-ray spectroscopy, high-purity germanium crystals are used to detect gamma rays and measure their energies. Impurities are added to the contacts to create a p-n junction. An n-type (p-type) coaxial detector has an n-type (p-type) inner contact created by diffusing lithium (boron) onto the crystal surface, and the outer p-type (n-type) contact is created by diffusing boron (lithium). Schematics of both n-type and p-type detectors are shown in Figure 3.3 both with a reverse bias applied to enlarge the depletion region.

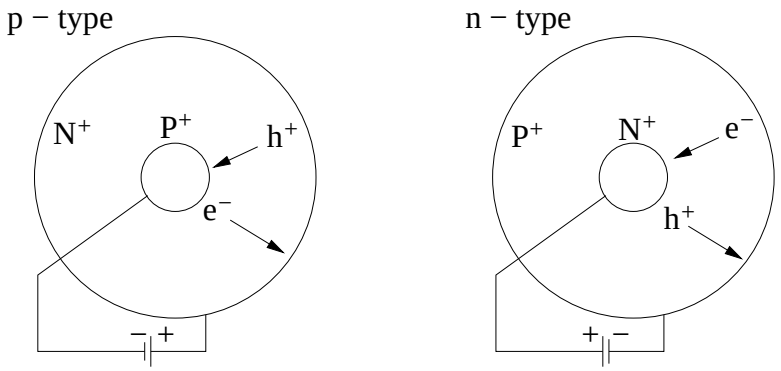

Figure 3.3: Schematic drawings of HPGe crystals with reverse bias applied, the flow of electrons (e^-) and holes (h^+) upon an incident gamma ray are indicated

To reduce noise created by thermal excitations across the energy gap, liquid nitrogen cools the HPGe crystals used in Jurogam array via a *cold finger* shown in Figure 3.4. Incident gamma rays create electron-hole pairs; as discussed above, the amount of liberated charge is directly related to energy deposited in the active medium.

Gamma rays interact with matter by photo-electric absorption, Compton scattering and pair production. The cross sections of these interactions for a given medium are energy dependent. Photo-electric absorption occurs when all of the energy of the gamma ray is transferred to an electron and occurs at low energies.

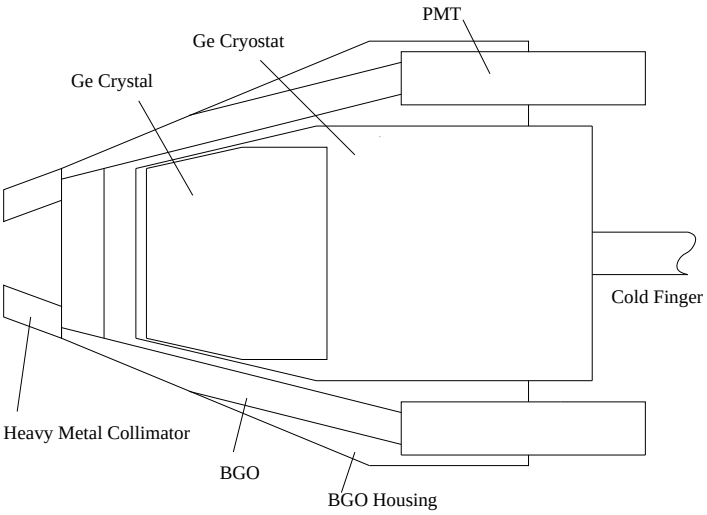

Figure 3.4: A schematic drawing of a HPGe Phase-I detector in the Jurogam array (not to scale)

Pair production refers to the creation of a positron and an electron when a gamma ray passes close by a nucleus. This can only occur when the gamma-ray energy is greater than twice the mass of the electron ($E_\gamma > 1022$ keV).

Compton scattering is the inelastic scattering between a gamma ray and an orbiting electron within a medium. The energy transferred in this reaction is dependent on the scattering angle. Compton scattering often occurs many times before the full energy of the gamma ray is absorbed. Gamma rays that Compton scatter in the active medium before exiting deposit only a fraction of the original gamma-ray energy, which is dependent on the number of interactions and scattering angles. A large number of gamma rays that experience one Compton interaction form an energy continuum up to *Compton edge*, which is the maximum energy in one interaction. Beyond this, a continuum is observed for multiple scattering interactions up to the full-energy photopeak. This gives rise to a poor peak-to-total ratio, and in turn a poor resolving power. To suppress the Compton background, a bismuth germanate (BGO) scintillator detector surrounds each of the germanium crystals (see Figure 3.4). Compton suppression is acheived by discarding any gamma events that

Table 3.1: Jurogam array detector angles and number of detectors

Ring number	θ	Array positions	number of detectors
1	157.60	1 - 5	5
2	133.57	6 - 15	10
3	107.94	16 - 25	10
4	94.16	26 - 30	5
5	85.84	31 - 35	5
6	72.05	36 - 45	10

are detected in both the germanium and the BGO shield that encloses it. With the large stopping power of the BGO detector, owing to its large Z, background is supressed the peak-to-total ratio is significantly improved [43, 44].

The Jurogam Array

At the time of the spectroscopic studies of ^{163,165}Os, the Jurogam array of 43 High-purity germanium n-type detectors was in place. These detectors are often referred to as Phase-I detectors as they were present before the Jurogam upgrade. In the array frame 6 rings are positioned at different angles with respect to the beam direction as shown in table 3.1. As timescale of prompt gamma emission is of the order of $10^{-15} - 10^{-10}$ s and a typical recoil velocity is 0.04c, gamma ray detectors are centred around the target position.

The quadrupole magnet on the entrance of RITU restricts the accessability to the lower angles and reduces the solid angle, this in turn reduces the overall detection efficiency. Corrections for the Doppler shifted energies are discussed later.

3.5.2 RITU (Recoil Ion Transport Unit)

The Recoil Ion Transport Unit is a gas-filled separator that separates fusion-evaporation residues from beam-like fragments. After the fusion evaporation products are formed, they move forward with a cone like trajectory due to different scattering angles. A

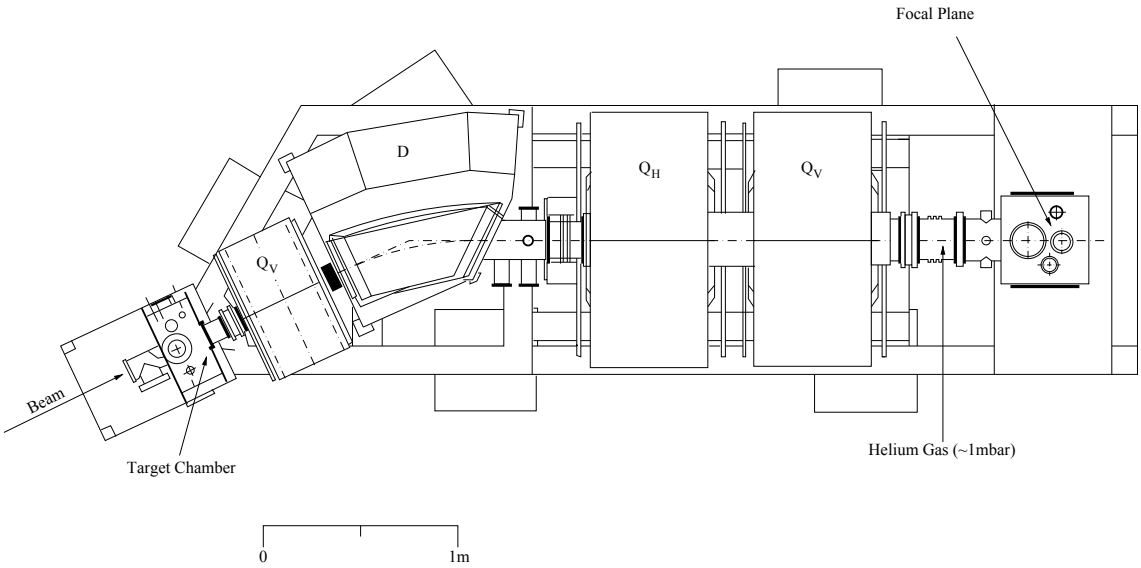

Figure 3.5: An edited schematic drawing of RITU taken from Ref. [2]

quadrupole magnet focuses the cone vertically before entering the dipole magnet discussed below. The magnets of RITU are shown in Figure 3.5.

The helium gas provides charge exchanging interactions leaving the recoiling nuclei in an *average charge state*. The separation by the dipole magnet is no longer so strictly dependent on the mass over charge ratio and can be described by the magnetic rigidity of traversing particles [45]. The force experienced by a charged particle in a magnetic field is described by the formula

$$\vec{F} = q\vec{v} \times \vec{B}, \tag{3.6}$$

where q and v are the charge and velocity of the particle traversing the magnetic field B, respectively. The recoils experience an acceleration perpendicular to the velocity described by $a = v^2/\rho$; this equation can be arranged to

$$B\rho = \frac{mv}{eq_{ave}}, \tag{3.7}$$

where m and ρ are the mass and the radius of the curvature of the trajectory and e

is the charge of an electron, respectively. An approximation for the average charge, $q_{ave} = (v/v_0)Z^{1/3}$, given by the Thomas-Fermi model is used to yield an approximate value for the magnetic rigidity $B\rho$:

$$B\rho = 0.0227A/Z^{1/3}, \tag{3.8}$$

where A and Z are the mass and proton number respectively. In reality the pressure of the helium gas inside the separator must be taken in to account in order to obtain a more realistic magnetic ridity. From this approximation, however, it can be seen that provided the $A/Z^{1/3}$ of the recoiling fusion-evaporation products and the beam like particles are sufficiently different, the two can be separated before entering a further vertical and horizontal focusing quadrupole magnet. The magnetic field can then be set so that the beam like residues are absorbed on the *beam dump* inside the dipole magnet, and the desired recoils are directed towards the DSSDs of the focal plane. Removing the discreteness of the A/Z ratio significantly increases transmission efficiency towards the focal plane (~ 40 %). As a result, mass selection is no longer possible. However the powerful technique of Recoil Decay Tagging (RDT) compensates for this loss (discussed later).

3.5.3 The GREAT (Gamma Recoil Electron Alpha Tagging) Spectrometer

The GREAT spectrometer is a composition of different detectors situated at the focal plane of RITU designed to detect incoming recoils and several subsequent radioactive decay modes. Each detector within the spectrometer can be used as a tagging device post-experiment thanks to the Total Data Readout method discussed below. Discussed in this section are the different detectors composing the GREAT spectrometer in the order with respect to the beam direction.

Multi-Wire Proportional Counter (MWPC)

Positioned at the exit window of RITU is the MWPC of GREAT. The MWPC is a gas detector that has good timing resolution and a high detection efficiency of charged particles, it is therefore ideal for detecting traversing recoiling nuclei. Two mylar foils comprise the entrance and exit windows which separate the isobutane which fills it from the low-pressure helium within RITU and the vacuum of GREAT. When a charged particle passes through the gas it creates free electrons and ions. In a similar fashion to semiconductors, the charge is collected at the anodes and the time and the deposited energy can be extracted. The MWPC is used in *anti-coincidence* to discriminate between decay, recoil and beam interactions within the implantation detector (the DSSDs). As the MWPC is the opening window to GREAT, the recoils must be focused on the 131 $\times$ 50 mm mylar aperture in order to pass through to focal plane.

Double-sided Silicon Strip Detectors (DSSDs)

After passing through the MWPC, the recoils are implanted in either of the two adjacent DSSDs separated by 4 mm. The DSSDs have an active area of 60 $\times$ 40 mm (120 $\times$ 40 mm in total) and have a depth of 300 μm which is sufficient for a typical recoil stopping distance of $\sim$ -20 μm . Each DSSD has 60 $\times$ 40 orthogonal strips with a strip pitch of 1 mm giving a total of 4800 pixels. The ambient temperature can cause thermal excitations in silicon, therefore the crystals are mounted on cooled blocks (coolant temperature $\sim 20^{\circ}$). A schematic diagram of GREAT can be seen in Figure 3.6. For clarity the MWPC has been omitted.

For part of results (see Chapter 6) the rear 80 y-strips were instrumented using Lyrtech digital electronics and run in *trace mode*. All signals from the preamplifiers were stored. As the event rate of the DSSD was $\sim$ 4 kHz this gave rise to a large data rate of $\sim$ 8 Mbs^{-1} for the 80 strips alone. The front 120 strips were instrumented

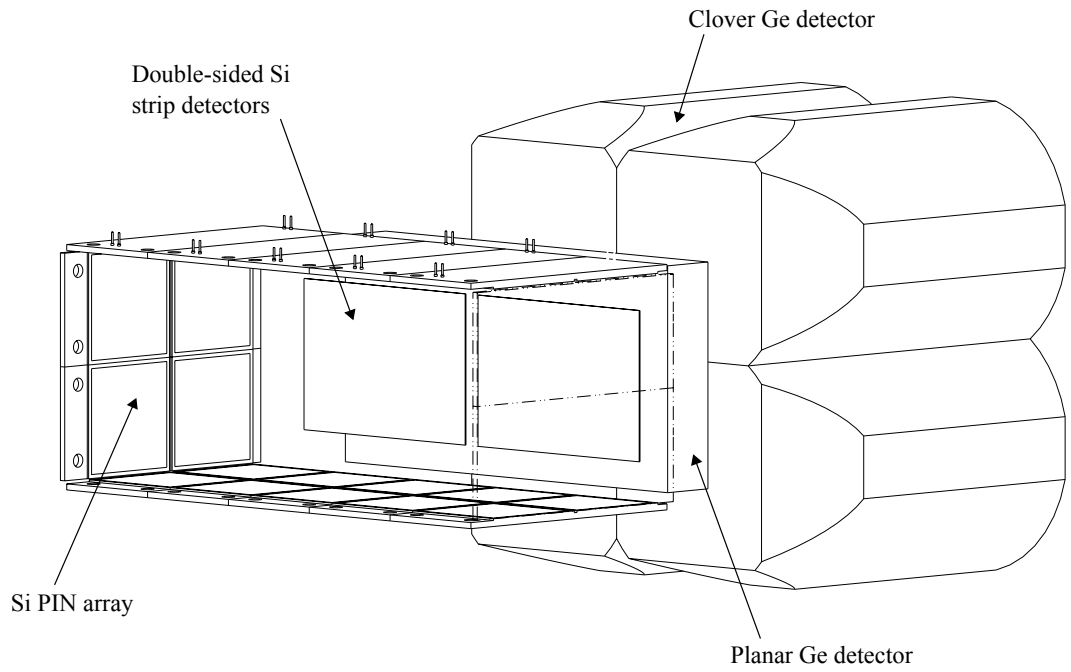

Figure 3.6: A schematic diagram of GREAT shown without the MWPC. The picure is taken from Ref. [3]

using analogue electronics with a dead time of ~ 7.3 μs. Pattern registers were also used in conjunction with the front strips so that spatial correlations with traces could be made during dead time. The purpose of this set-up was to eliminate all dead time; events occuring within the dead time of both the detectors would be observed as *pile-up* in the traces. An offline analysis of the traces can then be performed later. Information from the pattern registers were to retain x and y information of *pile-ups* whilst the electronics were dead.

Silicon PIN Diodes Array

Between the DSSDs and the MWPC is the silicon PIN diode array consisting of 28 PIN detectors, the arrangement of which is shown in Figure 3.6. Each diode has an active area of 28 $\times$ 28 mm and a thickness of 500 μm. Primarily, the PIN diodes are used for detecting conversion electrons. However, they can also be used to regain

energy information of escaping alpha particles. When an alpha particle is emitted in the upstream direction of the beam (towards the MWPC) and leaves the silicon it only deposits a fraction of its energy. If it is then implanted in the surrounding PIN diodes, the sum of the energy from both detectors is equal to the alpha particle's full energy. As typically 40 % of events *escape* the DSSDs, *add-back* can be a powerful tool in increasing statistics. Although not used in this thesis, this technique has been successfully using in Ref. [46].

Planar Germanium Strip Detector

A double-sided germanium strip detector is approximately 10 mm downstream of the DSSDs within the vacuum. This detector has an active area of 60 × 120 mm matching that of the DSSDs. A strip pitch of 5 mm in both x and y directions gives a total of 288 pixels, this spatial information enables correlations with the DSSD. The efficiency of the planar detector is optimised for low-energy gamma transitions and X rays. The maximum efficiency at < 100 keV is due to its relatively low thickness of 15 mm. High-energy gamma rays pass though the detector and are absorbed by surrounding *clover* detectors. Since the time of flight from Jurogam to implantation in the DSSD is ~ 0.5 μs, this detector is used for isomeric or delayed gamma radiation.

Clover Detectors

Four clover detectors are placed above, to the left and right and downstream of the focal plane. Each clover detector has 4 crystals segmented fourfold. These detectors are outside of the vacuum and are used for detecting high-energy gamma rays emitted from isomeric states. One of the four detectors can be seen in Fig. 3.6, this is at the very end of the GREAT spectrometer.

3.5.4 Total Data Read-out (TDR)

Before the TDR system came to place at Jyväskylä, detector systems used a hardware trigger to store data. For example, if the time of flight from the target chamber detectors to the focal plane was 5 μs, then all subsequent decays within a certain time after implantation would be stored with a 5 μs coincidence delay. The amount of information that can be extracted from these data is therefore limited to the initial triggers. The TDR system allows all events to be recorded with a 10 ns timestamp given by the metronome and channel number without using a trigger. The advantages of this are vast, it allows triggers to be made in software without losing any data. Because all events in all detectors are stored, it is possible to to correlate gamma rays to a specific nucleus using Recoil Decay Tagging (RDT), discussed in Chapter 4. [47]

3.5.5 Pattern Registers

A hit pattern VME module was used to provide a timestamp and channel number in parallel with the ADCs. The modules were used with the 120 analogue DSSD strips for the experimental set-up described in Chapter 6. If more than one strip fired within a certain time gate, the hit pattern output was the sum of the bits from each channel. A graphical representation of the output of a pattern register is shown in Figure 3.7.

In total the pattern register occupied 2^{16} bits. When a single channel, ch, is hit the pattern number 2^{ch} was recorded. If two channels of the module fired at the same time the resulting pattern number was $2^{ch_1} + 2^{ch_2}$, the log scale histogram in Figure 3.7 shows how often this happened. Each module had 16 inputs (channels 0 - 15), therefore 2^{16} bits could accommodate for the possibility of all channels that firing at the same time (2^{15}+2^{14}+2^{13}+...). As the hit pattern operated in parallel

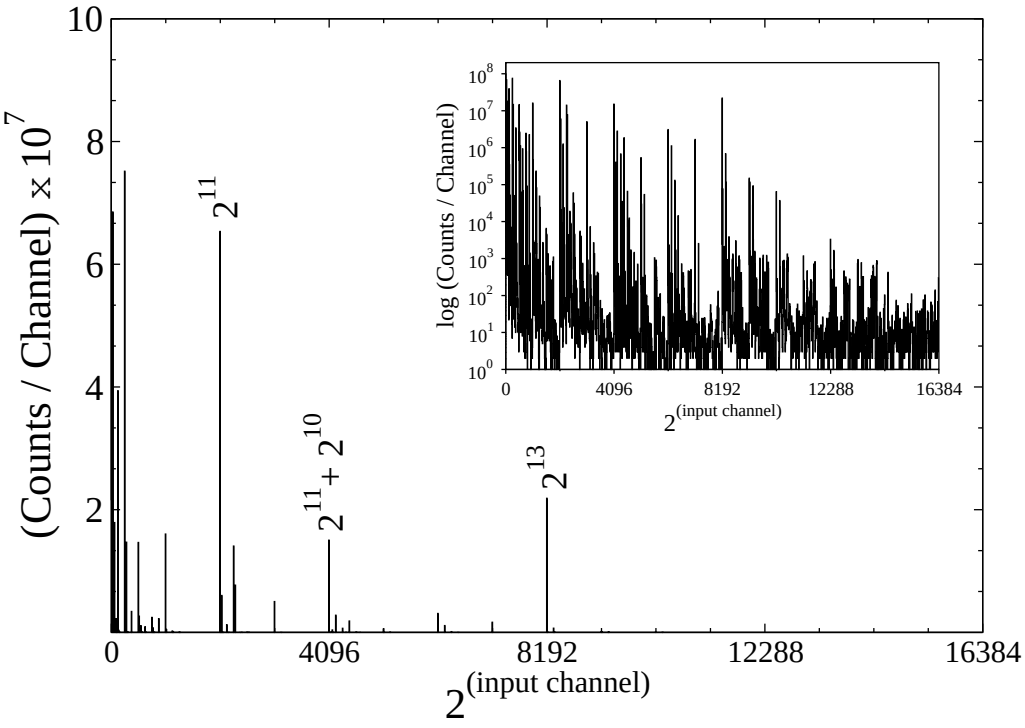

Figure 3.7: A histogram of the numbers output for one VME module. The smaller histogram shows the same histogram plotted with a log scale

with all other signal processing electronics, it was not effected by the dead time associated with ADCs etc.

Chapter 4

Experimental Methodology

4.1 Analysis Prerequisites

4.1.1 Calibrations

Prior to any analysis, all detectors must be calibrated using a known source. To perform a calibration on Jurogam, europium and barium (^{152}Eu and ^{133}Ba) gamma-ray sources are placed at the center of the array. A number of gamma rays were selected in the range 80 - 1408 keV and the energy calibrated as a function of channel number using the equation

$$E = a + (ch \times b) + (ch^2 \times c), \tag{4.1}$$

where ch, a are the channel number and intercept, and b and c are the linear and quadratic term coefficients. Gamma ray energies and intensities can be found in [48]. At low energies ($E_\gamma < 100$ keV) the detector response is non-linear, it has been observed that the residual of the fitted function resembles a damped sinusoidal function. This effect has no physical meaning but has been accounted for by fitting a function at low energies. An external mixed EuBa source is used at the focal plane

to calibrate the planar and clover detectors. Conversion electrons from a barium source within the vacuum of GREAT are used to calibrate the PINs. The DSSDs are initially calibrated using the most intense alpha decays of ^{239}Pu, ^{241}Am and ^{244}Cm using a linear calibration.

This calibration is a useful step for identifying populated alpha decays. However, because the alpha particles are emitted externally, there is energy loss before the alpha particles reach the active area of the detector. Moreover, the energy that is observed with an external souce is only the kinetic energy of the alpha particle and the energy of the recoiling daughter nucleus is not measured. An in-beam calibration using alpha decay chains is therefore performed to ensure observed alpha energies are correct.

4.1.2 Doppler-shift Correction

A typical beam energy for fusion-evaporation reactions is of the order of 10^2 MeV. For results discussed in Chapter 5, a beam of $\sim$ 350 MeV was used. This beam energy yields recoil energies of $\sim$4 % of the speed of light. Any gamma radiation emitted by a particle moving at this velocity will be Doppler shifted according to the equation

$$E_o = E_t \ (1 + \frac{v_{recoil} \ \cos\theta}{c}), \tag{4.2}$$

Where E_o and E_t are the observed and true gamma-ray energies respectively and θ is the angle of the emitted gamma ray with respect to the beam direction (see table 3.1). The value of $\frac{v}{c}$ can be calculated from the gradient when plotting the observed energy against $\cos\theta$ and fitting a straight line.

Figure 4.1 shows the effect of the Doppler shift on the two extreme angles, rings one (a) and six (c) at angles 157.60° and 72.05° respectively. A spectrum of the true energy is shown in (b). Transitions x and y are highlighted to show the increasing

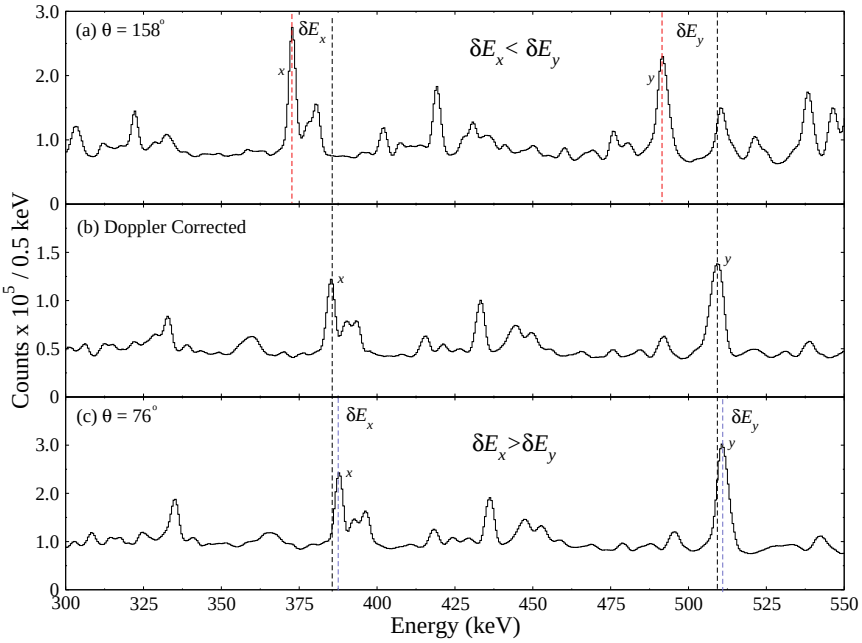

Figure 4.1: Recoil-gated Jurogam spectra of (a) ring 1, (b) the true energy and (c) ring 6. Centroids of transitions x and y in (a), (b) and (c) have been highlighted with red, black and blue dashed lines respectively

effect of the Doppler shift as a function of energy. The shifts with respect to $\theta = 90°$ are analogous to red shift and blue shift. For the backward (forward) angle, the wave is stretched (compressed) and therefore the frequency is decreased (increased). The increase in shift as a function of energy is more noticeable in Figure 4.1 (a) because of the large angle. The high velocity of the recoiling nuclei also introduces an effect known as Doppler broadening, this arises from the range of angles spanned by the diameter of the germanium crystal which cannot be corrected for. The angles quoted in Table 3.1 are the angles at the centre of the exposed surface of the germanium crystals. The $\delta\theta$ leads to an error on the observed energy at the ring angle, giving rise to a spread of energies around the centroid and an increased FWHM.

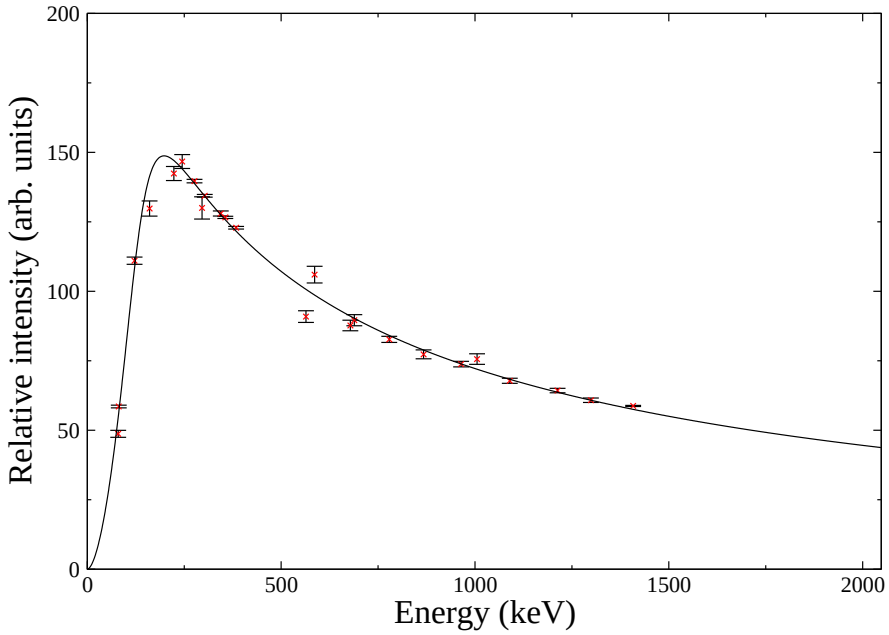

Figure 4.2: Relative efficiency of the Jurogam HPGe array as a function of energy

4.1.3 Efficiency Correction

The interaction cross section for gamma radiation in an active medium is highly dependent on energy. An intrinsic efficiency must be calculated when measuring the intensities of gamma rays. Several factors contribute to the nature of a detector's efficiency as a function of energy. An example of an efficiency curve for Jurogam from the ^{163}Os data can be seen in Figure 4.2. The fit was calculated by a chi-squared minimization routine in the Radware program EFFIT [49].

The cross section of an interaction between a photon and the active volume of the detector is dependent on the energy of the incident photon and the proton number of the material. Consequently, the penetration depth is also a function of energy. The maximum efficiency is therefore dependent on the size of the crystal in the detector; the larger the crystal the more efficient the detector is at higher energies.

Defects within the germanium crystal decrease the energy resolution of the detector, a good balance between resolution and efficiency must be achieved. Jurogam has a maximum efficiency of $\sim$ 20 % at 200 keV. The employment of the efficiency curve will be discussed later.

4.2 The Recoil Decay Tagging (RDT) Technique

When using the recoil decay tagging technique, an *event* is defined as an array of time-ordered signals grouped together by a trigger on a DSSD signal. When defining an event, it is required to set a software trigger which associates signals in other detectors with the DSSD signal of interest. If a signal from a detector lies within the trigger width of the DSSD signal, the two signals are said to be *in coincidence* and are collectively defined as an event. For example, prompt gamma radiation will lie within the trigger delay of a DSSD recoil signal (see Figure 4.4). When there is a large signal in a strip of the DSSD cross talk between the strips can occur, meaning that a single interaction can cause several strips to fire. In this case the largest signal is taken as the event.

The recoil-decay tagging technique allows spatial and temporal correlations to be made between any number of events within a decay chain. The simplest example of recoil-decay tagging consists of three steps: 1) Identify a decay event in a pixel of the DSSD, 2) Correlate this with a recoil signal within the same pixel from which it was emitted, 3) Assign gamma transitions to the known recoiling nucleus. Figure 4.3 (a) shows prompt gamma transitions of all events without any correlations; the spectrum contains gamma rays emitted by a myriad of nuclei produced in the experiment discussed in Chapter 5. The large distribution in the middle is the "Coulex" peak of the target; the width is due to the range of scattering angles. With only this information it would be impossible to assign any of these gamma transitions to a

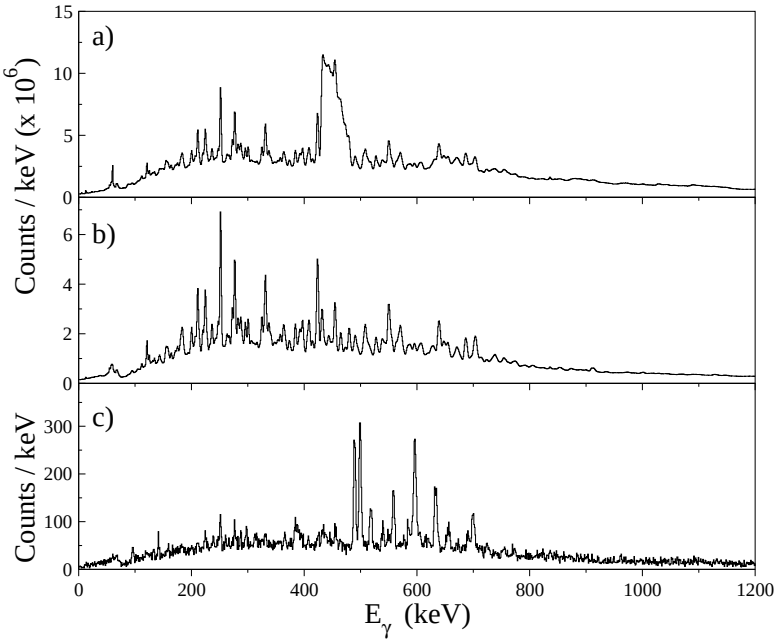

Figure 4.3: (a) DSSD triggered Jurogam energy spectrum. (b) Recoil-gated Jurogam energy spectrum. (c) Jurogam energy spectrum triggered on a recoil followed by an alpha decay characteristic of ^{165}Os.

nucleus.

Cleaning up this spectrum requires applying the above-described technique. If energy has been deposited in the MWPC within an event's trigger, it is very unlikely that the event is a decay. A recoil deposits a larger amount of its kinetic energy in the isobutane gas ($Z_{recoil} > Z_{beam}$ [50]) and has a lower velocity due to conservation of momentum; it is therefore possible to discriminate between beam-like particles and fusion evaporation products and define the latter as a recoil event. By default the MWPC energy has a value of -1, events with this value are therefore defined as decay events. This procedure is widely used and described more fully in [46]. A further condition is set on the TOF between Jurogam and the DSSD to remove any gamma rays associated with the beam, i.e. miscorrelations and Coulomb excitations. A spectrum of gamma transitions correlated with recoil events is shown in Figure 4.3 (b). Already there is a large reduction in background and the Coulex peak is absent.

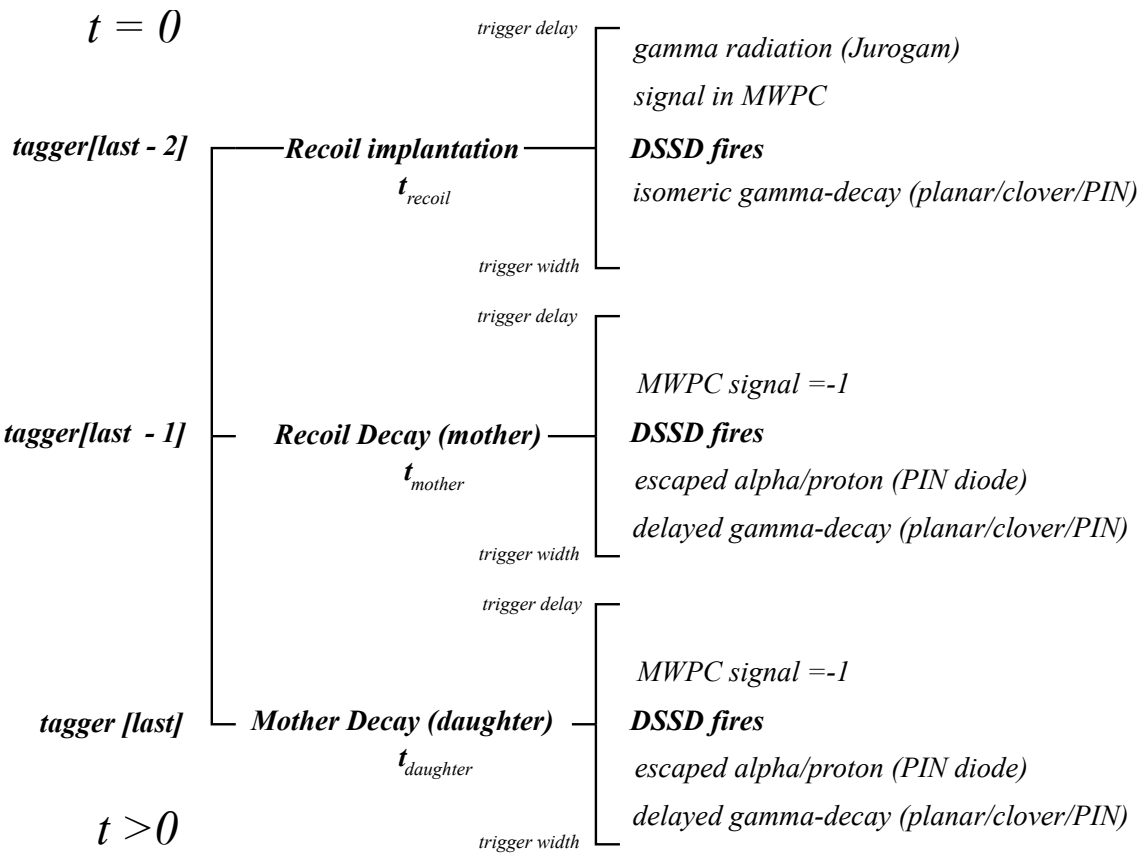

Figure 4.4: An example of time-ordered events within the tagger are shown with detector information contained within the trigger.

To assign these recoil-gamma transitions to a known nucleus, further conditions are set at the focal plane. The species of the recoil can be obtained by observing its decay time and energy. Figure 4.3 (c) has been obtained by requiring $t_{recoil} - t_{decay} < 5t_{\frac{1}{2}}$ where $t_{\frac{1}{2}}$ is that of ^{165}Os and the energy is equal to that of its alpha decay. This is known as *tagging* and the observed gamma ray transitions can be unambiguously assigned to ^{165}Os.

The data analysis package Grain [51] allows this technique to be employed over all 4800 DSSD pixels simultaneously. A moving array of events commonly referred to as the *tagger* is used to *tag* events and pull out information for any detector of any previous event within an appropriate time frame. The RDT technique described above can be extended to any number of subsequent decays. Figure 4.4 shows an

example of a common sequence of events present in the tagger where a recoil implantation is followed by two decay events labelled *mother* and *daughter* in time order. In this case, similar conditions to those described above can be set on the daughter event to learn information on the mother event or regain gamma-ray correlations lost because of escaping mother alpha/protons. Both uses of the tagger have been employed in this thesis and are described in more detail in the results section.

4.2.1 Coincidence Analysis

If an event is identified as a recoil, all interactions within the trigger are stored in the tagger. Subsequent particle decays in the GREAT spectrometer are tagged, as described above, to correlate them with gamma decays stored within the recoil event. As the lifetimes of the prompt-gamma emitting states are so short, the decay of several cascades are observed at the target position by different detectors with a very short time difference. Like the trigger described above, a time gate is set in the Java *sort code* to define if gamma rays are in coincidence with each other (i.e. if they are part of the same decay path to the ground state). An array is then built for each set of coincident gamma rays. From this, a two-dimensional matrix can be built so that a *slice* at a certain energy will give an energy spectrum of all events observed in coincidence with the gamma rays within the slice. A level scheme of several bands (built on different orbitals) is constructed by *gating* on gamma rays and observing coincidences. An example of gamma-gamma coincidence is shown in Figure 4.5.

Figure 4.5 (a) shows a projection of the recoil-gated gamma-gamma matrix. As the strongest populated channel, the transitions from the first few excited states of ^{166}W are easily identifiable and are indicated [52]. A gate set on the 424 keV ($4 \rightarrow 2$) peak yields the spectrum seen in (b). A gate set on the 550 keV transition yields the spectrum seen in (c). The presence of the 550 keV and 911 keV transitions in

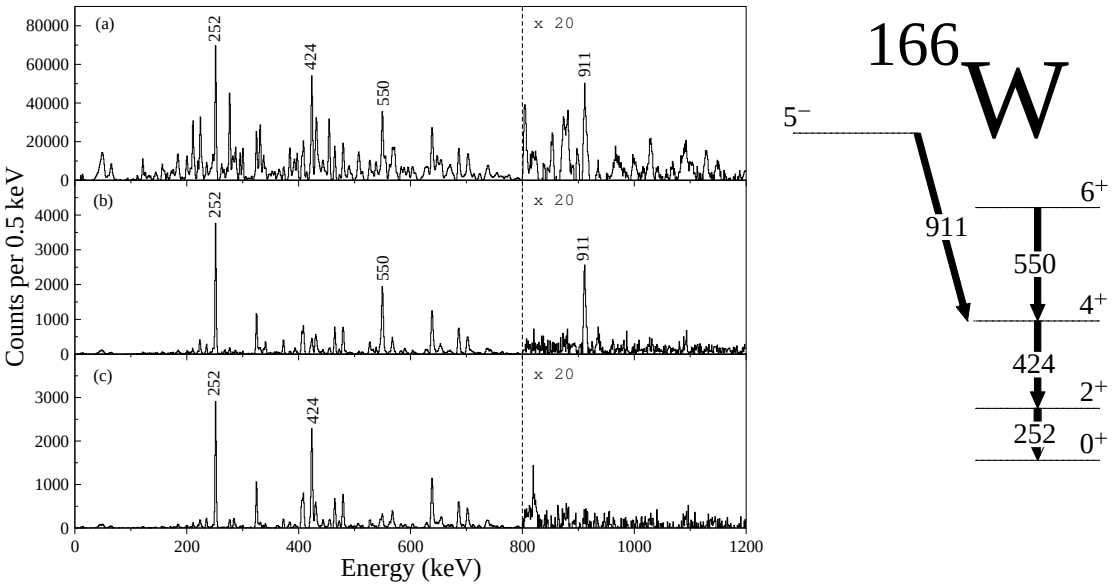

Figure 4.5: Jurogam energy spectra of (a) recoil-gated gamma rays, (b) gamma rays in coincidence with the 424 keV transition and (c) gamma rays in coincidence with the 550 keV transition. For clarity, the scale has y scale has been increased past 800 keV. Using these spectra, the previously established level scheme on the right can be deduced.

Figure 4.5 (b) mean the 424 keV transition is in coincidence with both transitions. When gating on 550 keV, the 911 keV transition is no longer present. This indicates the two transitions are not in coincidence and therefore decay via separate cascades (bands). The level scheme shown in Figure 4.5 can be deduced, in which the transitions are ordered by their respective intensity.

4.3 Trace Analysis

As discussed in the previous chapter, traces from charge-sensitive preamplifiers were recorded for every interaction detected in the rear strips of the two DSSDs at the focal plane. A trace is a numerical representation a charge pulse observed when an interaction occurs within the detector. The height of the trace is directly proportional to the amount of charge liberated in the active medium of a detector and therefore to the energy of an interaction. Examples of some of the traces recorded

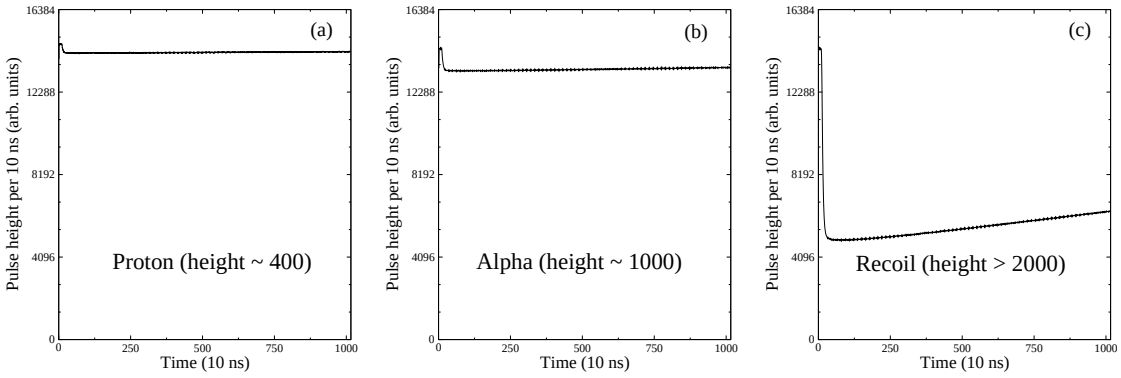

Figure 4.6: Uncorrelated traces of (a) a proton, (b) alpha and (c) recoil signal output by the Lyrtech cards

are shown in Figure 4.6.

The baseline of a trace is 100 ns long and its offset is dependent on time elapsed since the previous pulse and its height. A recoil rate of $\sim$ 2 kHz and the relatively short decay constant, τ, of 200 μs [53] means the pulse has almost fully returned to the detector's baseline for most traces ($\sim$ 14000 arb. units, see Figure 4.6). A ^{239}Pu alpha particle (5.157 MeV) gives a pulse height of $\sim$ 1000. The full dynamic range of the strips is therefore $\sim$ 70 MeV; this large range is crucial for detecting any decays that occur after recoil implantation within the 10 μs trace length. Recoil energies lie within this range provided the offset is sufficiently high to accomodate it. Interactions exceeding the range are generally beam or punch-through particles and account for 7 % of the recorded traces. Traces discussed in this section have been taken directly from the data stream.

4.3.1 Moving Window Deconvolution

Moving Window Deconvolution (MWD) is an analogue-to-digital conversion method that can be applied to any exponential signal from an RC preamplifier, although it is more often used in high-resolution gamma-ray spectroscopy. There are several steps to a MWD and it can be applied more than once to gain different results although a

minimization of shaping time is necessary for a reduction in dead-time. Discussed in this section is a simplified version of an analogue-to-digital conversion in a detector system.

In the DSSD, the rise time of a pulse is of the order of 100s of nano-seconds. For the purpose of this section, signals from the preamplifier are described as an ideal pulse with zero rise time and no ballistic deficit, which will be discussed later. A visual representation of this ideal scenario can be seen in Figure 4.7 (a) where a pulse is followed by a second pulse of the same energy. The initial gradient of the two decaying pulses is dependent on the height from the baseline (the point to which the pulse will eventually decay after an infinite amount of time), thus the second pulse appears to have a different shape. The length of this window is 10 μs (1000 samples) and is what one would expect to see in a trace where two events occur in the same strip when Δt $<$ dead-time. To extract the height of these pulses the initial statements

$$f(t_n) = \begin{cases} A_0 \exp(-\frac{t}{\tau}) & t \geq 0 \\ 0 & t < 0 \end{cases}, \tag{4.3}$$

are made. Knowledge of the amplitude, $f(t_n)$, at time t_n where n is the sample number (every 10 ns), allows for the derivation of the initial amplitude, A_0, at $t = 0$. The manipulation of Equation 4.3 to get the continuous decay curve in the form of a quantizable step function is shown in Equation 4.4.

$$\begin{aligned} A_0 &= f(t_n) + A_0 - f(t_n) \\ &= f(t_n) + A_0 - A_0 \exp\left(-\frac{t_n}{\tau}\right) \\ &= f(t_n) + A_0\left(1 - \exp\left(-\frac{t_n}{\tau}\right)\right) \\ &= f(t_n) + \frac{1}{\tau}\int_0^{t_n} f(t_n)\ dt \\ &= f(t_n) + \frac{1}{\tau}\int_{-\infty}^{t_n} f(t_n)\ dt \end{aligned} \tag{4.4}$$

By substituting the trapezoidal approximation of the integral,

$$\int_{-\infty}^{t} f(t)\ dt = \sum_{k=0}^{n-1} x[k], \tag{4.5}$$

and changing the function to a discrete set of numbers of sample number n, the amplitude can be represented in the discrete form shown in Equation 4.6,

$$A[n] = x[n] + \sum_{k=0}^{n-1} \frac{1}{\tau} x[k], \tag{4.6}$$

where $A[n]$ is the height of the step function at sample point n and is equal to the sum of the energies of all previous pulses. This can be further simplified:

$$\begin{aligned} A[n] &= \left(x[n] + \frac{1}{\tau}\sum_{k=0}^{n-1} x[k]\right) - \left(x[n-1] + \frac{1}{\tau}\sum_{k=0}^{n-2} x[k]\right) + A[n-1] \\ &= x[n] - \left(1 - \frac{1}{\tau}\right) x[n-1] + A[n-1] \end{aligned} \tag{4.7}$$

The result of this conversion is shown in Figure 4.7 (b). The conversion into this form means the step function is infinite in height and must be further operated on to get into a form from which the signals energy can be processed. A numerical

differentiation of this step function is performed by the equation

$$\mathrm{MWD}_M[n] = A[n] - A[n-M], \tag{4.8}$$

where M is an integer that defines the length of the flat top of the MWD. The result of this differentiation is shown in Figure 4.7 (c). In a real signal, there are small ocillations owing to the noise from the preceding circuitry [54]. This noise is suppressed after the MWD module by taking a moving average of length L of the MWD given by the equation,

$$\mathrm{MA}[n] = \sum_{k=n-L}^{n-1} \frac{\mathrm{MWD}[k]}{L}. \tag{4.9}$$

The result of Equation 4.9 is shown in Figure 4.7 (d) where $M = 110$ and $L = 70$ (10 ns). The trapezoidal shape of equal height to the MWD is achieved providing $L < M$. The dimensions of the trapezoid are dependent on L and M and are indicated in the figure.

In reality, the rising edge of the pulse is smeared as charge collection slows towards the maximum height of the pulse. This effect varies from one detector to another as charge collection rates differ. Silicon detectors suffer from this effect commonly referred to as ballistic deficit, so called as the pulse still rises beyond the height of the MWD. Figure 4.8 shows the same MWD as above applied on a real pulse (trace) of an alpha decay. The baseline has been extrapolated based on an average of the 10 samples (when $t < 0$).

The flat top of the trapezoid shown in Figure 4.8 (d) increases as a function of time towards the true energy. This is a result of ballistic deficit and the full energy information of the interaction cannot be retrieved. Ballistic deficit is therefore a major contribution to the degradation of resolution. See Reference [55] for more information and simulations of ballistic deficit. As the right-hand side of the flat

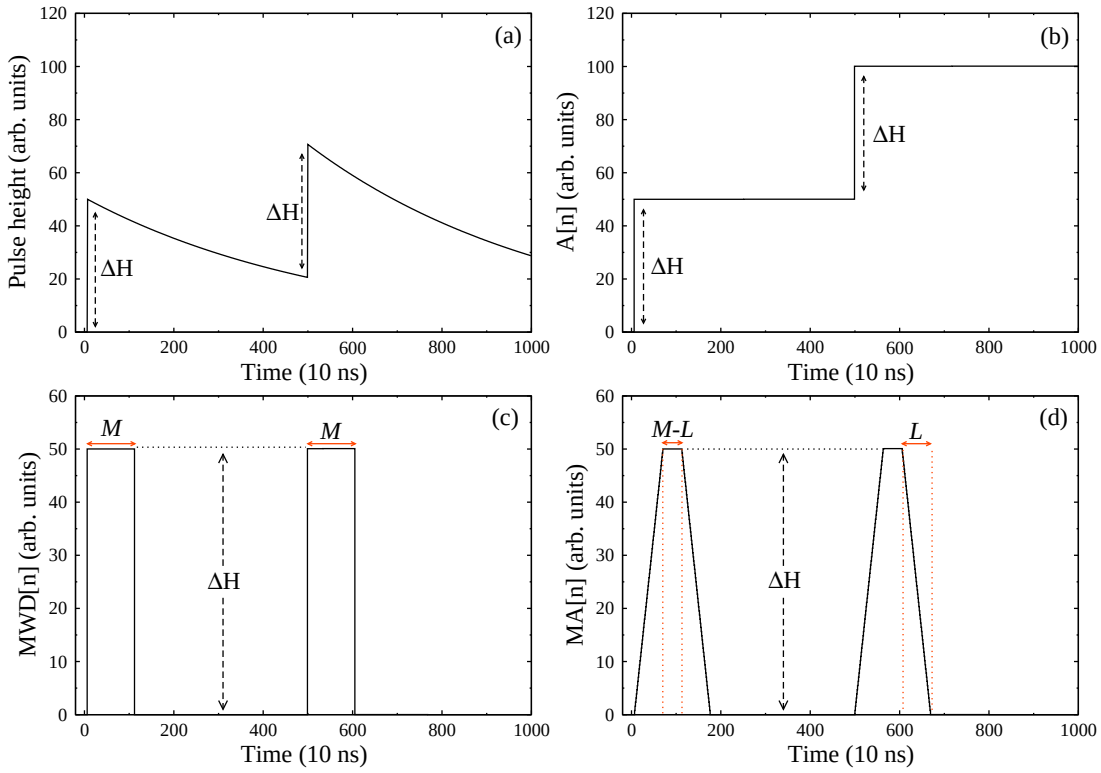

Figure 4.7: (a) a theoretical ideal pulse from a discharging RC preamplifier followed by a pulse of the same energy. The conversion into a discrete step function is shown in (b). The MWD of this step function is shown in (c) where the width of the flat top is equal to M. The final step of shaping is shown in (d) and the dimensions of the trapezoid are indicated. The height is constant throughout providing $L < M$.

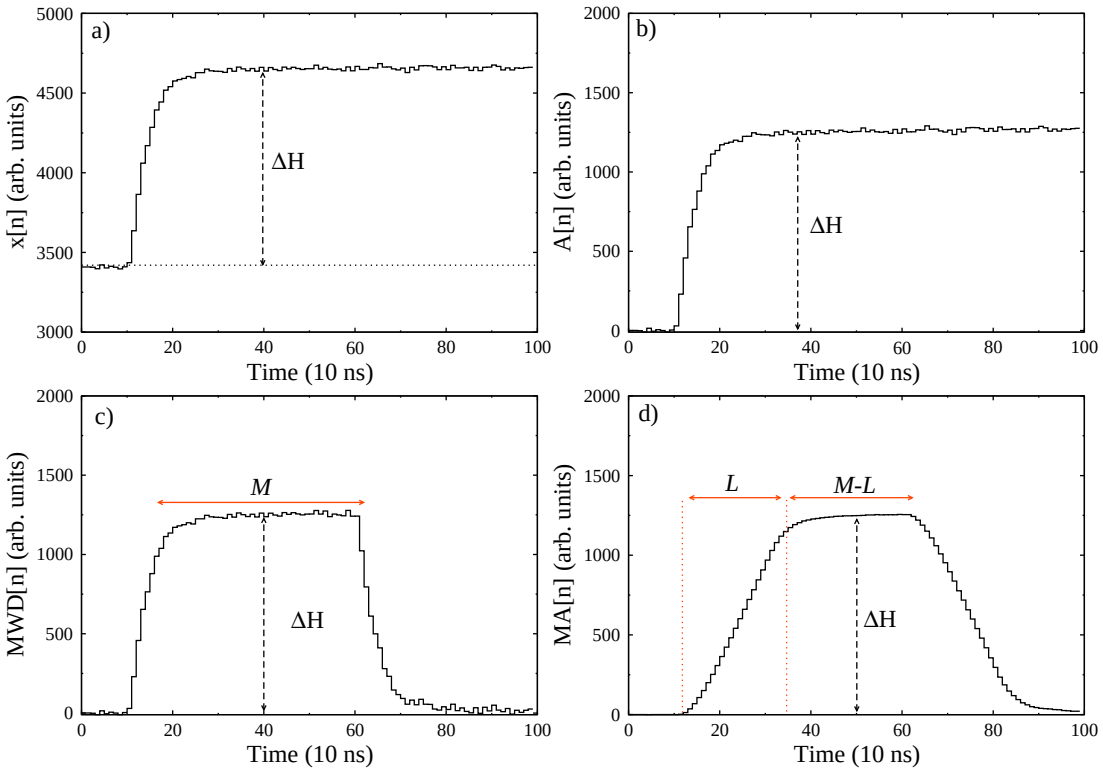

Figure 4.8: (a) a real pulse (alpha particle) from a discharging RC preamplifier with an offset, the conversion into a step function is shown in (b). The MWD of this step function is shown in (c) where the width of the flat top is roughly equal to M. The final step of shaping is shown in (d) and the dimensions of the trapezoid are indicated. The height is constant throughout providing $L < M$.

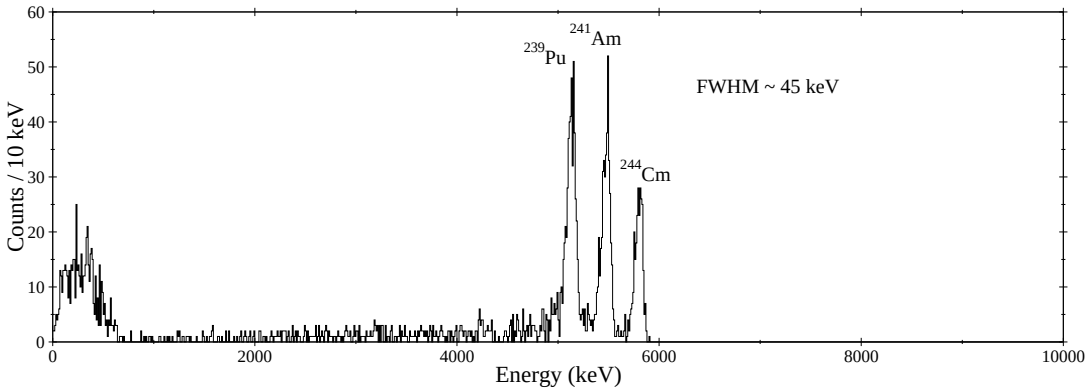

Figure 4.9: A calibrated energy spectrum resulting from an MWD performed on traces obtained using the three-line alpha source. Parent nuclei of the alpha energy peaks are labelled.

top of the trapezoid gives the most accurate representation of the energy, the height is sampled here. An energy spectrum obtained using the offline MWD of calibration traces from a single strip of the DSSD is shown in Figure 4.9.

The spectrum in Figure 4.9 was obtained mid-way through the experiment at which point the DSSDs had been subject to some radiation damage which, combined with the problem of ballistic deficit, result in a relatively large Full-Width Half Maximum FWHM. The fine structure of these decaying nuclei has been encompassed by the width of the peak and contributes to the left tail to each respective Gaussian.

Although resolution is not greatly degraded, the ballistic deficit has an effect on any subsequent pulses up to a few microseconds after the leading edge. During this time, any pulse will appear to have a larger amplitude due to the charge remaining from the last interaction. As the time window of interest is 10 μs, the MWD is not an appropriate method of measuring the energy of decay following a large recoil signal.

4.3.2 The Superpulse Method

As the effect of ballistic deficit lasts for a relatively large length of the trace the exponential component is small, thus the shape of an alpha decay signal does not

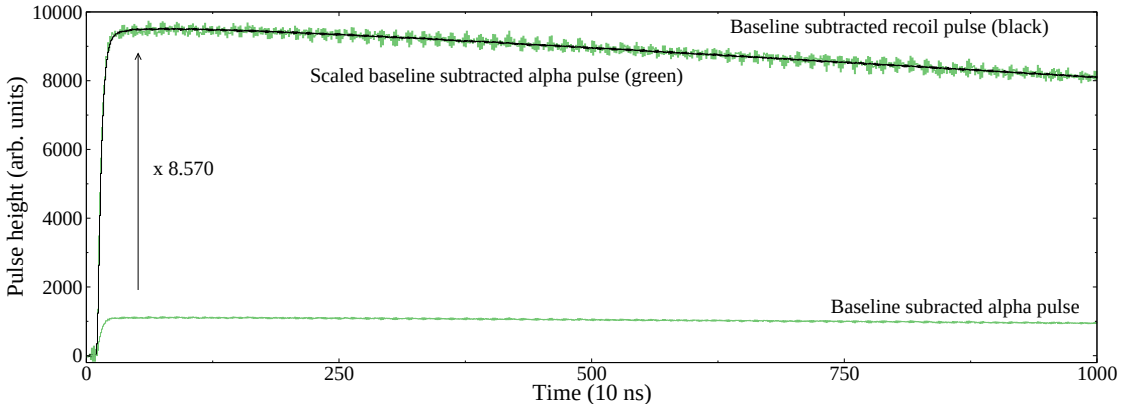

Figure 4.10: An example of baseline-subtracted alpha (green) and recoil (black) pulses. The scaled alpha pulse is also shown and superimposed onto the recoil pulse.

differ greatly from a recoil or proton pulse. Each sample in an alpha trace can therefore be linearly scaled to produce a good fit to a proton or recoil trace. Figure 4.10 shows the same recoil (black) and alpha (green) signals as those in Figure 4.6.

The baseline subtracted alpha pulse shown in Figure 4.10 is scaled to the same height as the recoil by minimizing the chi-squared. The noise of the alpha trace has also been scaled and therefore appears larger. The scaling factor is a representation of the recoil energy as a function of the alpha trace and has arbitrary units. When this method is applied to all traces of the same strip, the energy of each interaction can be described by the scaling factor of the fit. A histogram of these scaling factors will therefore give a spectrum with energies that must be calibrated.

To employ this scaling technique a characteristic pulse with minimized error should be used. As the scaling factor can be easily calibrated using the three-line alpha source, it seems appropriate to sum many *real* alpha traces to produce an average pulse. Using the MWD to select appropriate pulses will give pulses of a certain height but introduces *mirror charges* that will distort the average pulse. An example of a mirror charge signal can be seen in Figure 4.11.

Mirror charge signals are a consequence of the large electric fields within a strip due to the charge of particles in the neighbouring strips. As there is no liberated

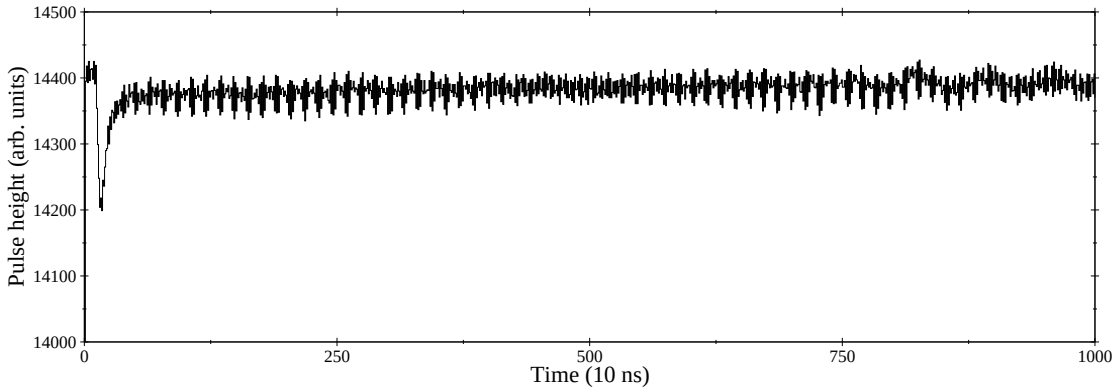

Figure 4.11: An example of a mirror charge pulse. As the pulse is only caused by a change in electric field no charge is collected; the capacitors of the preamplifier quickly discharge and the voltage quickly returns to the baseline

charge the observed pulse returns to the baseline quickly. If a decay happens on the edge of a strip, a large signal will be seen in the neighbouring strip. This effect is more prominent with in-beam interactions as recoils and beam-like fragments have a much larger charge than decay products and causes an exponential-like continuum at the low end of the energy spectrum. Setting conditions on a pulse height at a point after a mirror-charge returns to baseline ensures all traces included in the *super pulse* are real interactions.

As the noise varies from trace to trace the super pulse must be as smooth as possible so that the shape of the noise does not affect the chi-squared minimization. Figure 4.12 shows several super pulses obtained by averaging over different numbers of traces. Also shown in Figure 4.12 is a plot of the Pearson's chi-squared test for some of the super pulses when fitted to the calibration traces of the same strip. Pearson's chi-squared test is given by the formula

$$\chi^2 = \sum_{i=0}^{1016} \frac{(Trace[i] - Superpulse[i])^2}{Trace[i]}. \tag{4.10}$$

Inintially there is a large difference in chi-squared from 1 to 2 trace averaging, but the difference in the chi-squared of the fit between 50 and 1000 averages is minimal.

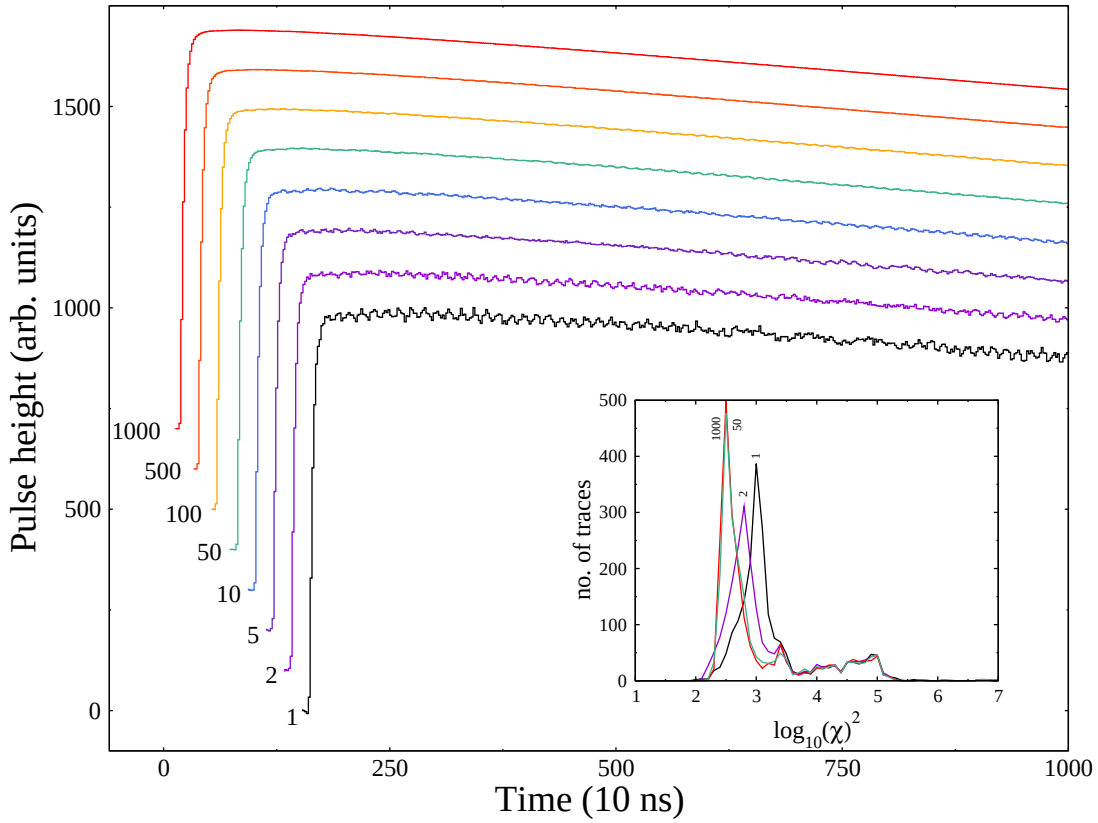

Figure 4.12: Super pulses obtained with several different sample sizes are shown. The time and baselines have been shifted for clarity.

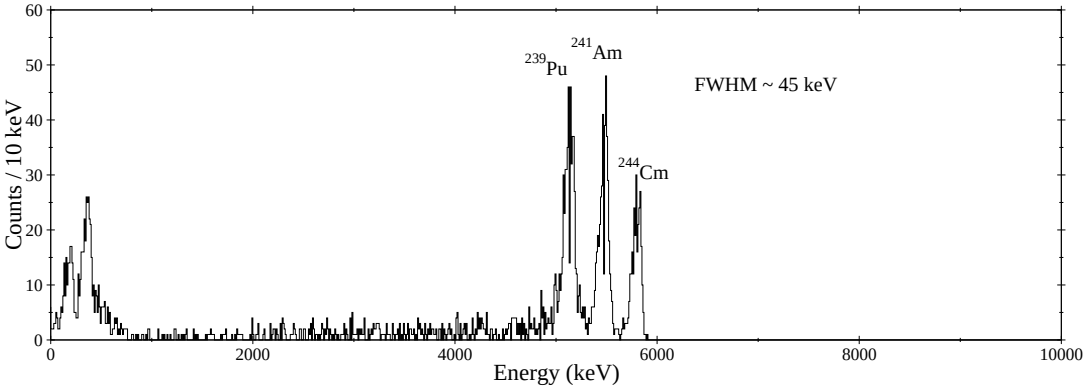

Figure 4.13: A DSSD energy spectrum of the three-line alpha source using the super pulse method.

A super pulse of 50 traces is therefore suitable for energy measurements of the traces. Figure 4.13 shows the energy spectrum of the 3-line alpha source using the super pulse method.

The spectrum is very similar to that of the MWD (see Figure 4.9), only differing at the lower energies where mirror-charge pulses are dealt with differently. A similar FWHM of $\sim$ 45 keV justifies the use of this method for measuring energies of interactions. Although the MWD and super-pulse method appear to give very similar results, the super-pulse method has the advantage of accounting for the ballistic deficit and would work for any shape of pulse, provided the shape was consistent.

To apply this method to piled up traces, a two-step fit is performed. An algorithm was written to identify piled up traces and the time at which the pileup occurs. The pileup filter takes a numerical differention of a two-sampled-wide moving average of the trace given by

$$\mathrm{FD}[n] = (x[n] + x[n-1])/2 - (x[n-1] + x[n-2])/2, \tag{4.11}$$

where n is a sample of trace x. The second operation given by

$$\mathrm{SSD}[n] = (\mathrm{FD}[n])^2 - (\mathrm{FD}[n-1])^2, \tag{4.12}$$

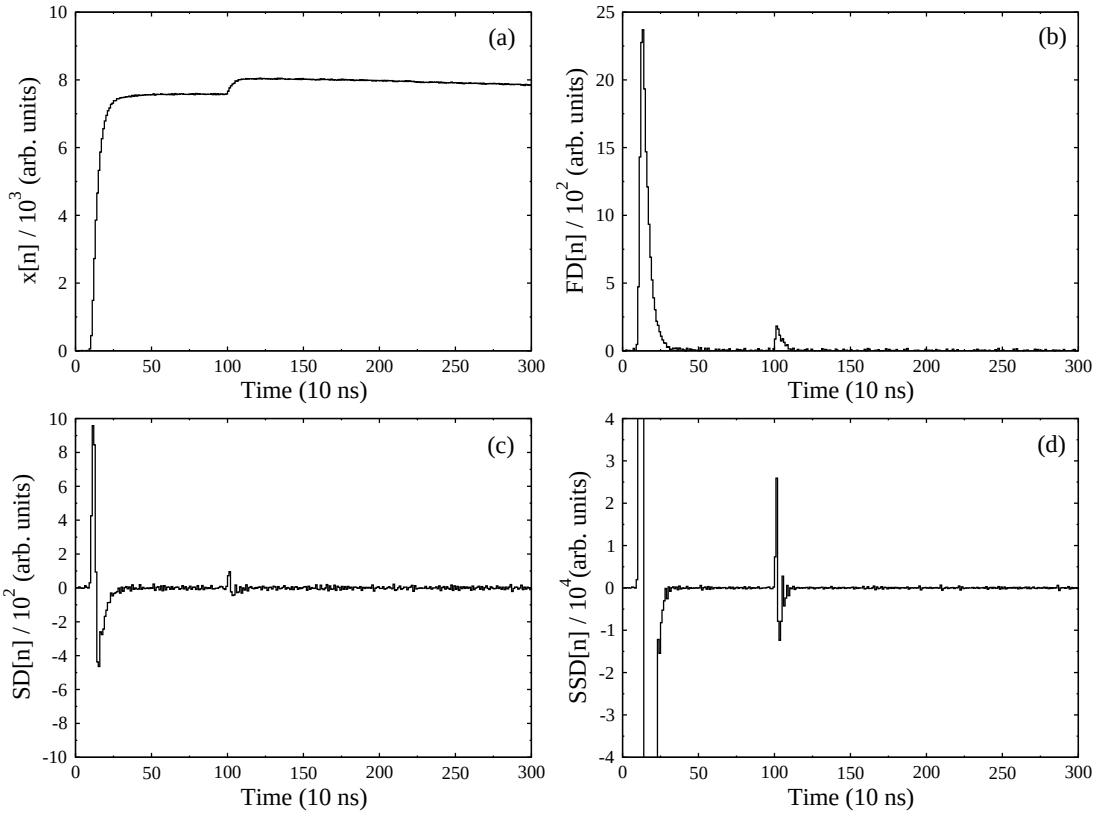

Figure 4.14: (a) An example of a trace of a recoil followed by a proton. The result of the FD operation (see Equation 4.11) performed on the trace shown in (a) is shown in (b). The FD operation performed on (b) is shown in (c). The result of the SSD given by equation 4.12 is shown in (d).

results in an enchanced squared-second differentiation SSD. A comparison of this method compared to a standard second differentiation (a repeat of FD[x]), SD[x], are shown in Figure 4.14.

Figure 4.14 (a) shows a trace of a recoil followed by an interaction with an energy similar to that of a proton. The result of the FD operation is shown in (b). The time difference of these events can be measured by taking the centroids of the two peaks and subtracting one from the other. The result of the SSD is shown in (d), it can be seen that the signal to noise ratio with respect to SD shown in (c), is dramatically increased. A lower threshold can be set on SSD, decreasing the possibility of filtering any useful pileups.

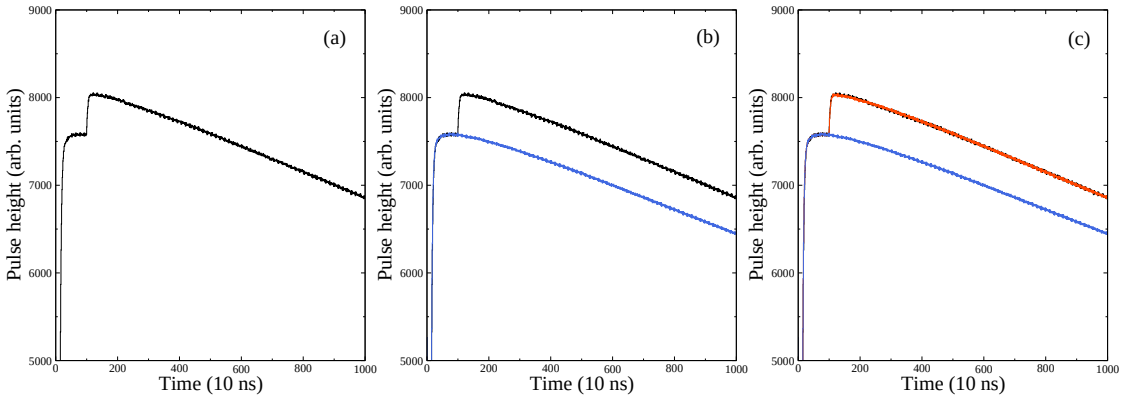

Figure 4.15: (a) A trace of a recoil followed by a particle decay pile up. (b) The first step of the fitting process, the recoil part of the trace has been fitted(blue). (c) The second part of the fitting process, the residual is fitted (red).

The recoil signal before the point at which the threshold is passed is then fitted and subtracted from the piled up trace, the result of this fit can be seen in Figure 4.15 (b). As the super pulse contains the features of a recoil signal, the ballistic deficit is also subtracted. The residual of the subtraction is a pulse that has the shape of a normal decay that can be fitted. The superposition of the two fits is shown in Figure 4.15 (c). The scaling factor of the fit of the residual pulse is directly related to the energy of the second interaction.

The varying offset means that two pulses of the same energy can have a very different shape. For example, if the piled up signal shown in Figure 4.14 (a) had occured at the same offset without the presence of the previous recoil, the super pulse would not be able to fit it. If the shape of the scaled pulse is different to the recoil signal, then the residual pulse will have a shape different to a typical pulse. As the recoil energy is not important, in the case of a non-zero offset the baseline of the super pulse is varied as well as the height to minimize the chi-squared value and get the best fit possible. This scenario rarely occurs as the event rate is ~ 4 kHz (an average of ~ 20 Hz per strip), the average recoil-recoil time difference is ~ 50 ms; the largest possible pulse (~ 14500) decays to baseline after ~ 700 μs ($5t_{1/2}$).

Chapter 5

Low-lying excited states in ^{163}Os and ^{165}Os

5.1 Experimental Details

Excited states in ^{163}Os and ^{165}Os were populated using the reactions listed in Table 5.1. Experiments 2 and 3 were performed consecutively and data from these experiments have been combined for the study of ^{165}Os. The beam species were provided by the K130 cyclotron at the University of Jyväskylä Accelerator Laboratory. Gamma rays emitted at the target position were detected by the JUROGAM spectrometer, comprising 43 escape-suppressed HPGe detectors [43] (See Chapter 3). Fusion-evaporation residues recoiling from the target were separated from scattered beam and transported to the focal plane by the RITU gas-filled separator [45, 56, 57]. At the focal plane fusion evaporation residues were implanted into the double-sided silicon strip detectors (DSSDs) of the GREAT spectrometer [58]. The GREAT multiwire proportional counter provided energy loss and (in conjunction with the DSSDs) time-of-flight information, which allowed the recoils to be distinguished from the scattered beam and subsequent radioactive decays. All detector signals were time

Table 5.1: A table showing experimental details.

Experiment Number	Beam Species	Energy (MeV)	Current (pnA)	Target Isotope	Thickness (mg/cm^2)	Exit Channel	Residual Nucleus	Experiment Duration (h)
1	^{60}Ni	270	4	^{106}Cd	1.1	$3n$	^{163}Os	120
2	^{78}Kr	357	6	^{92}Mo	0.5	$3n2p$	^{165}Os	172
3	^{78}Kr	357	6	^{92}Mo	1.0	$3n2p$	^{165}Os	26

stamped and recorded by the total data readout data acquisition system [59], which allowed implanted nuclei to be identified through temporal and spatial correlations with their subsequent radioactive decays. These data were sorted offline and analysed using the GRAIN [51] and ESCL8R [49] software analysis packages.

5.2 Results

5.2.1 ^{163}Os ($N = 87$)

The recoil-decay tagging (RDT) technique correlates γ rays emitted promptly at the target position with the characteristic radioactive decays of the residual nucleus at the focal plane of a recoil separator [60, 61, 62]. The RDT technique provides high-confidence correlations under the optimum conditions of short decay half-lives and high decay branching ratios. The α-emitting nucleus ^{163}Os has decay properties well suited to RDT spectroscopy. The half-life of ^{163}Os has been measured to be 6.8±0.4 ms which agrees well with the previously measured half-life of 5.5±0.6 ms [22]. A total of 10656 full-energy (E_α = 6510 keV) α(^{163}Os) decays were observed in Experiment 1 (see Table 5.1). Assuming a RITU separation efficiency of 50 % [57] and an efficiency of 65 % for full-energy α-particle detection, this yield corresponds to a cross section of ∼0.5 μb. Figure 5.2(a) shows γ rays correlated with recoil implantations followed by the characteristic α decay of ^{163}Os within the same DSSD pixel of the GREAT spectrometer. The recoil-decay correlation time was limited to 25 ms. The measured properties of γ rays in ^{163}Os are listed in

Table 5.2: Transition energies and relative intensities of γ rays assigned to ^{163}Os and ^{165}Os obtained from the pertinent α-correlated γ-ray singles spectrum. The error on the transition energies ranges from ≈0.5 keV to 1 keV. The multipolarity assignments for ^{165}Os are listed (see text for details).

^{163}Os		^{165}Os		
E_γ (keV)	I_γ (%)	E_γ (keV)	I_γ (%)	Multipolarity
112.0	23(3)	95.2	14(3)	M1
238.4	42(4)	384.3	13(2)	
521.4	31(4)	388.7	10(2)	
553.1	9(3)	489.6	79(3)	E2
556.0	6(3)	499.3	100(3)	E2
561.0	20(4)	518.0	33(3)	E2
623.7	100(7)	539.8	13(3)	
636.9	65(7)	558.6	38(3)	E2
651.4	26(6)	584.9	25(4)	
661.3	73(6)	593.0	19(4)	
668.5	39(4)	596.7	97(5)	E2
693.6	14(3)	604.5	16(2)	
700.0	43(5)	633.2	64(4)	E2
722.5	27(3)	656.1	24(3)	
		691.6	15(2)	
		699.8	43(3)	E2

Table 5.2.

A significant fraction of α particles escape from the DSSD without depositing their full energy. However, it is possible to utilize these decays if there is a distinct daughter α decay with appropriate decay properties. Figure 5.1(a) is an energy spectrum of *gas-vetoed* [1] alpha events that follow a recoil event in the same DSSD pixel within 32 ms.

Decay lines of lighter nuclei are observed due to miscorrelations between recoil implantation and highly populated decay products. Only the strongest alpha decay lines of nuclei that were likely to have been directly populated are labelled. Figure 5.1(b) is an energy spectrum of daughter alpha events occurring within 24 ms of events shown in Figure 5.1(a); the characteristic alpha decay of ^{159}W is highlighted. The $E_\alpha = 6292$ keV decay line in ^{159}W [63] has been measured previously to have a high α-decay branching ratio (92 %) and a half-life of 8.2±0.7 ms [63], which is suffi-

[1] The DSSD event is in anti-coincidence with the gas detector, i.e. it is a decay event

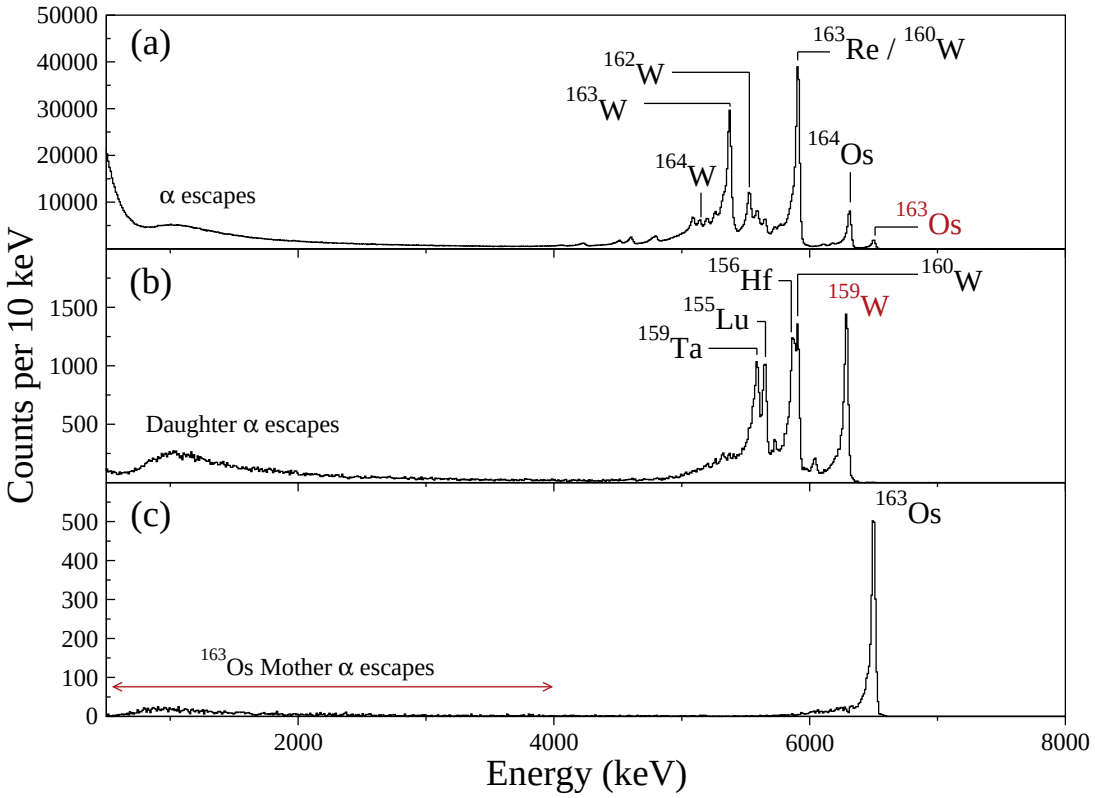

Figure 5.1: (a) Shows a gas-vetoed DSSD energy spectrum of alpha events that occur within 32 ms of recoil implantation, the ^{163}Os alpha-decay line is highlighted . (b) Is an energy spectrum of daughter alpha decay events that occur within 24 ms of events shown in (a), the ^{159}W alpha-decay line is highlighted. (c) Is an energy spectrum of events shown in (a) which are followed by the ^{159}W events shown in (b).

ciently short to give clean correlations with escaping ^{163}Os α particles. Figure 5.1(c) is an energy spectrum of mother alpha events correlated with the ^{159}W alpha decays shown in Figure 5.1(b) with the same time correlations.

Figure 5.2(b) shows a γ-ray spectrum obtained by demanding correlations with escaping α particles shown in Figure 5.1(c). In these data, 2822 escaping α decays satisfied the criteria and were added to the statistics for the γ-ray coincidence analysis. Figure 5.2(b) shows that the γ-ray counting statistics may be augmented through escape correlations without increasing the γ-ray background noticeably. Even so, a meaningful angular correlation analysis was not possible with these data

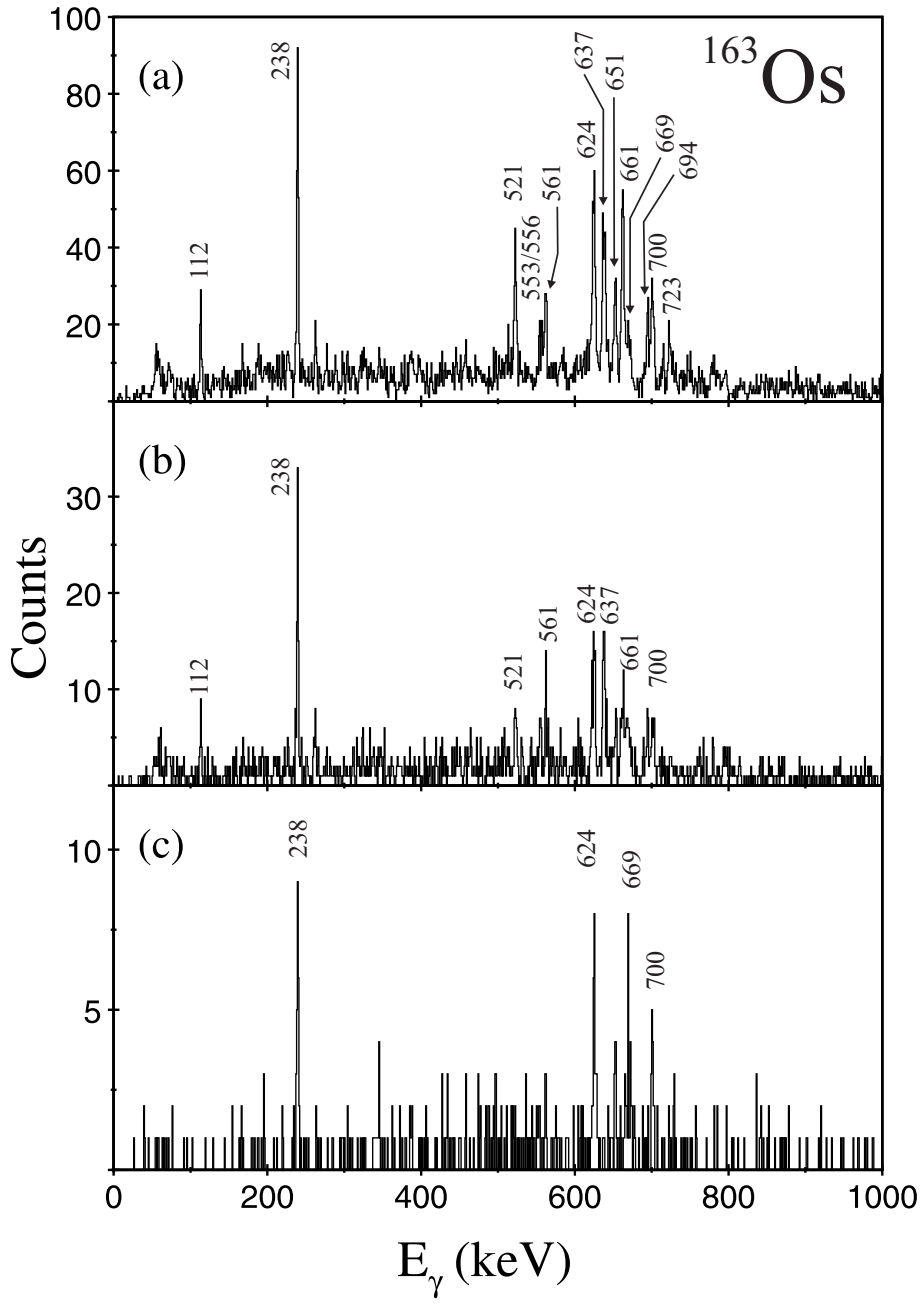

Figure 5.2: (a) Gamma rays correlated with recoil implantations followed by the characteristic α decay of ^{163}Os within the same DSSD pixel of the GREAT spectrometer. (b) Gamma rays correlated with escaping $\alpha(^{163}\text{Os})$ followed by the daughter $\alpha(^{159}\text{W})$ decay within the same pixel of the DSSD. The energy range for the escape α particle is limited to 500 - 4000 keV. The correlation time was limited to 25 ms for the first decay and 32 ms for the second decay. (c) Gamma rays in coincidence with the 624, 669, 700 or 238 keV transitions generated from a $\gamma\gamma$ coincidence matrix correlated with ^{163}Os full-energy and escape α correlations.

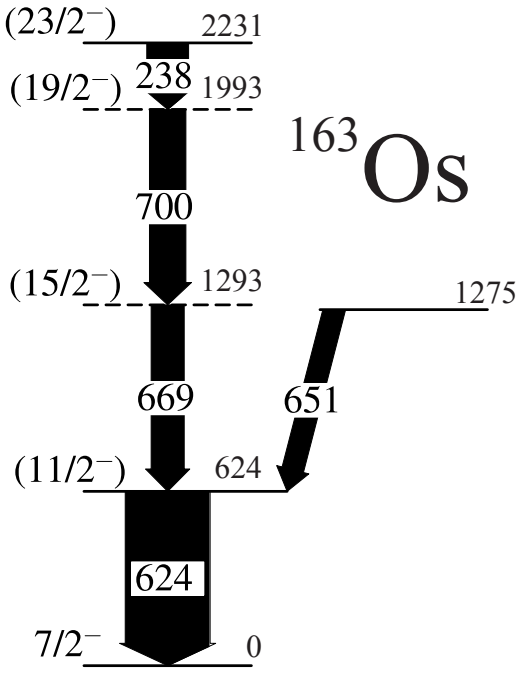

Figure 5.3: Level scheme deduced for ^{163}Os. The transition energies are in keV and their relative intensities are proportional to the width of the arrows. The Internal conversion intensity has been estimated and is included in the width of the arrows.

due to the low level of statistics, which precluded unambiguous multipolarity assignments for the measured γ rays.

A recoil-decay tagged $\gamma\gamma$-coincidence matrix correlated with the full-energy and escape $\alpha(^{163}\text{Os})$ particles was produced from these data. This matrix demonstrated that the 238, 624, 669 and 700 keV γ rays are in coincidence forming a cascade. Figure 5.2(c) shows a summed coincidence spectrum for these transitions. This cascade is assumed to be composed of stretched E2 transitions feeding the ground state. The 624 keV peak is the most intense γ ray and is assumed to be the $(11/2^-) \rightarrow 7/2^-$ transition. The ordering of the 669, 700 and 238 keV transitions could not be unambiguously established from the intensity measurements and coincidence relationships, so the ordering is based on the systematics of excited states in the light Os nuclei. The excitation energy of the $(23/2^-)$ state is insensitive to the ordering of these γ rays. The 651 keV transition is observed to be in coincidence only with the 624 keV transition and is assigned to feed the $(11/2^-)$ state. The level scheme de-

duced for ^{163}Os is presented in Fig. 5.3. The relatively strong 661, 637 and 521 keV transitions that are associated with ^{163}Os (see Fig. 5.2(a) and Table. 5.2) do not appear to be in prompt coincidence with the main cascade and could not be placed in the level scheme.

5.2.2 ^{165}Os ($N = 89$)

The neutron-deficient nucleus ^{165}Os is an α-emitting nucleus with decay properties that are also ideally suited for recoil-decay tagging. In a past study, the half-life of ^{165}Os has been measured to be 72±3 ms with a branching ratio close to 100 % [63]. The half-life has been re-measured in this work as 70.5±0.4 ms. A total of 149953 full-energy (E_α = 6188 keV) α(^{165}Os) decays were observed in Experiments 2 and 3 (see Table 5.1), corresponding to a cross section of ∼5 μb, assuming a RITU separation efficiency of 50 % [57] and an efficiency of 65 % for full-energy α-particle detection. Figure 5.4 is an energy spectrum of gas-vetoed alpha events that follow a recoil event in the same DSSD pixel in experiments 2 and 3.

Again only the strongest alpha lines of nuclei produced directly by fusion evaporation are labelled. The strongest channel produced is $4p$ (^{166}W) [52], but the alpha branching ratio is very low and is not observed at the focal plane. Figure 5.5(a) shows γ rays correlated with recoil implantations followed by the characteristic α decay of ^{165}Os highlighted in Figure 5.4. The recoil-decay correlation time was limited to 280 ms. The measured properties of γ rays in ^{165}Os are listed in Table 5.2.

The γ-ray spectrum in Fig. 5.5(a) shows the same transitions discovered by Appelbe *et al.* in an earlier RDT experiment probing ^{165}Os [18]. In that experiment there were insufficient coincidence data to determine an excitation level scheme. Given the complex character of the spectra in nuclei approaching the single-particle regime, γ-ray coincidence analyses are crucial for ordering the excitation level schemes. Fig-

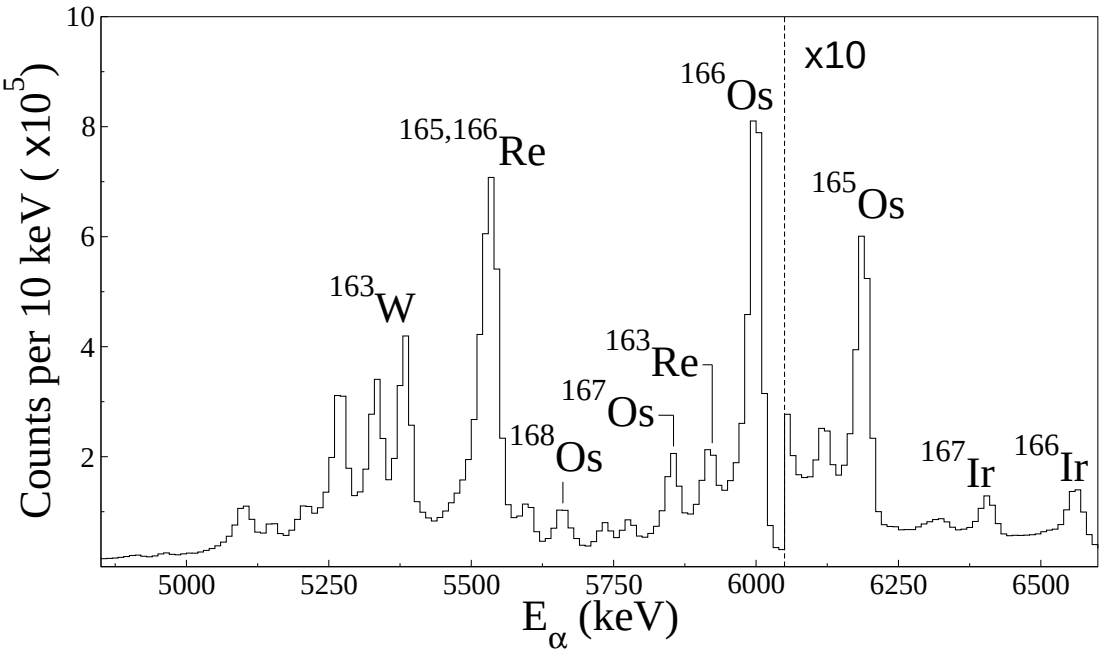

Figure 5.4: Gas vetoed alpha spectrum for experiments 2 and 3 (see Table 5.1). The scale is adjusted at 6.05 MeV to emphasize the ^{165}Os alpha decay peak

ures 5.5(b) and 5.5(c) show summed γ-ray coincidences obtained from an $\alpha(^{165}\mathrm{Os})$-correlated $\gamma\gamma$ coincidence matrix. Correlations with the escaping $\alpha(^{165}\mathrm{Os})$ decays were not included due to the γ-ray background generated by correlations with the daughter, ^{161}W ($t_{1/2}$=409±18 ms, b_α=73±3 %) [63], which is significantly longer lived than the ^{163}Os daughter, ^{159}W. Multipolarity assignments for the strongest γ-ray transitions in ^{165}Os were obtained from angular intensity ratios, R_θ. In this method a ratio of $\alpha(^{165}\mathrm{Os})$-correlated γ-ray intensities detected at the θ=158° and θ=(94° and 86°) spectrometer angles was extracted. The method employed discriminated between different multipolarities in ^{166}W yielding typical R_θ values of approximately 0.8 and 1.7 for stretched quadrupole and stretched dipole transitions, respectively [64]. The angular intensity ratios extracted for ^{165}Os are shown in Figure 5.6 and their multipolarity assignments are listed in Table 5.2. Figure 5.7 shows the level scheme deduced on the basis of γ-ray coincidences, relative intensities and angular intensity ratios.

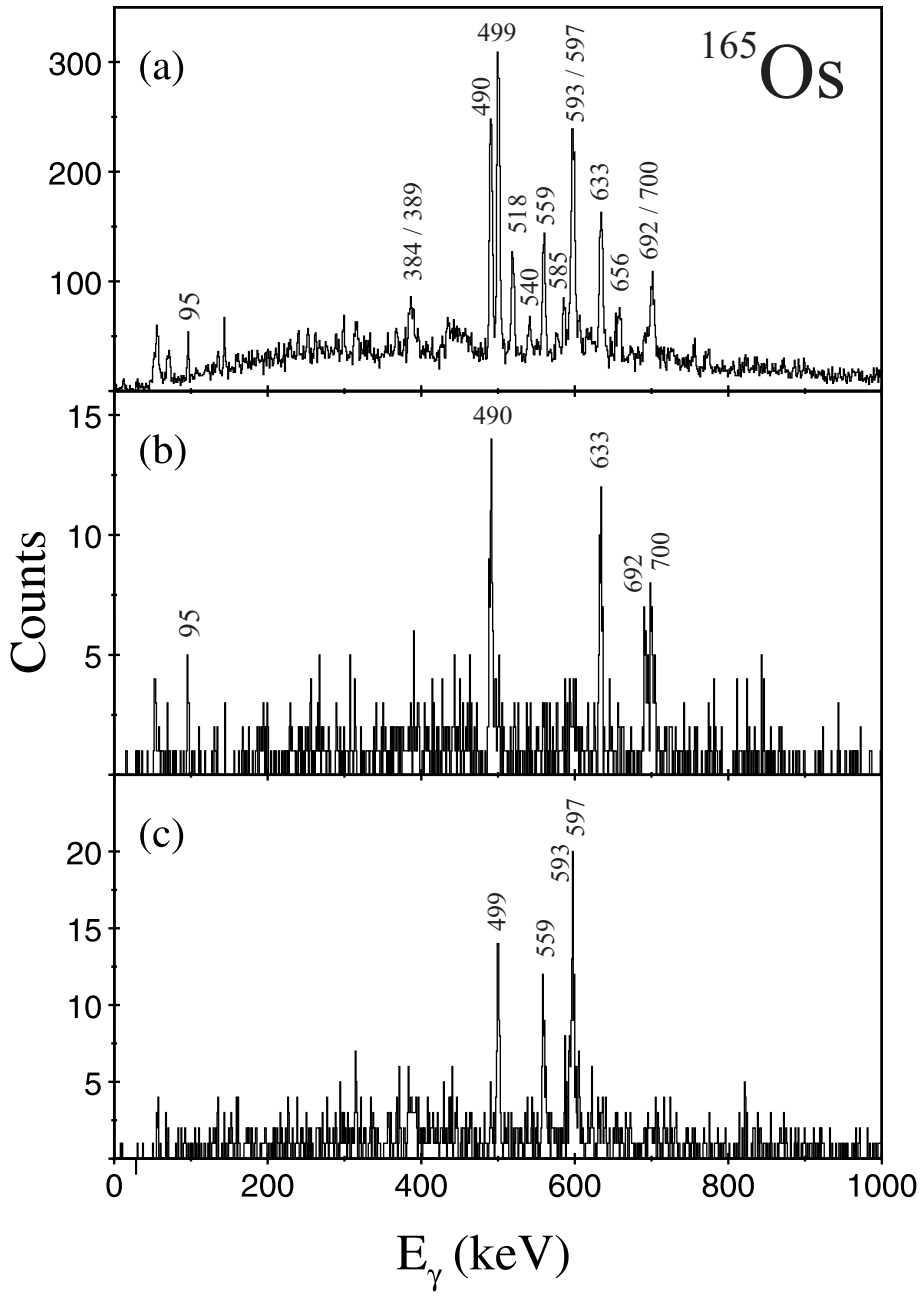

Figure 5.5: (a) Gamma rays correlated with recoil implantations followed by the characteristic α decay of ^{165}Os within the same DSSD pixel of the GREAT spectrometer. (b) Summed γ-ray spectrum in coincidence with the 490, 633, 700 or 692 keV transitions generated from an $\alpha(^{165}\text{Os})$-correlated $\gamma\gamma$ coincidence matrix. (c) Summed γ-ray spectrum in coincidence with the 499, 597, 559 or 593 keV transitions generated from an $\alpha(^{165}\text{Os})$-correlated $\gamma\gamma$ coincidence matrix. The recoil-α correlation time was limited to 280 ms in each case.

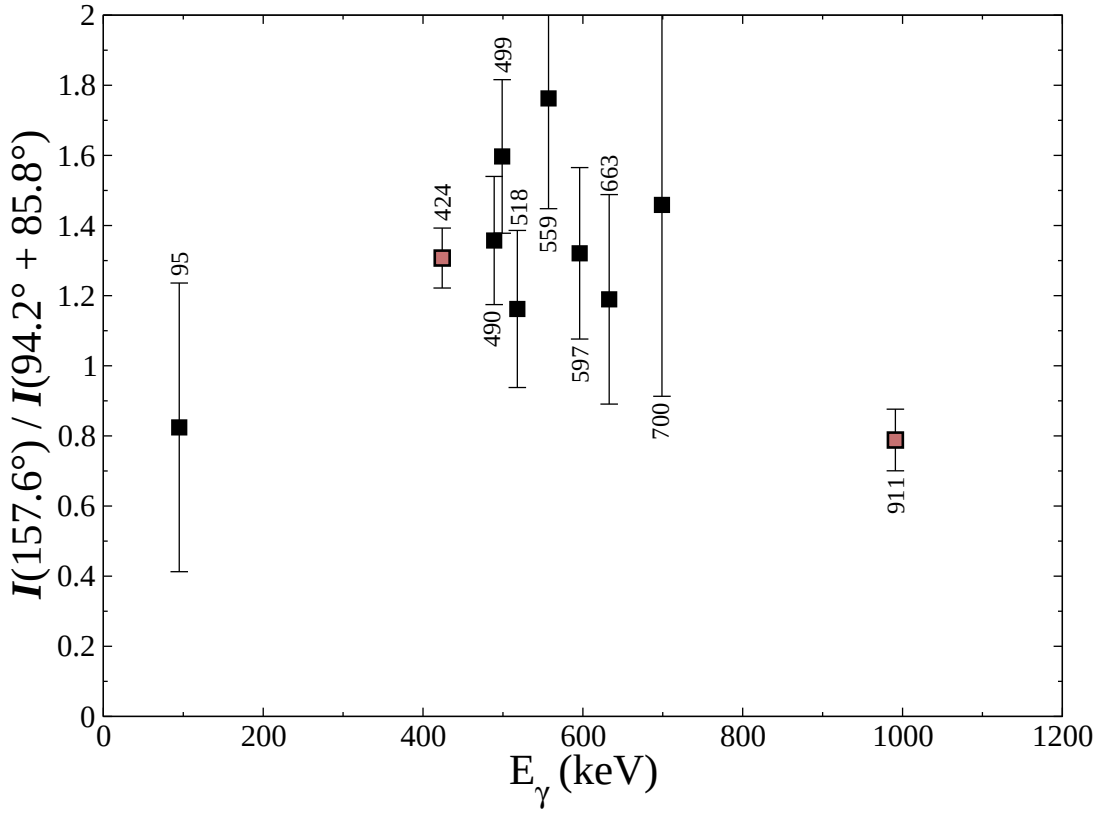

Figure 5.6: Angular distribution intensity ratios between ring 1 and rings 4 and 5. Reference points 424 keV (E2) and 911 keV (M1) are previously measured gamma rays of ^{166}W and are highlighted in red.

While the level of counts is very low, these summed coincidence spectra suggest that there are two distinct low-spin structures in ^{165}Os. Figure 5.5(b) shows γ rays in coincidence with the 490, 633, 700 or 692 keV γ rays, which form the left hand side of Fig. 5.7. It is assumed that the 95 keV transition, which is not apparent in Fig. 5.5(c), is a stretched magnetic dipole transition connecting a stretched E2 cascade to the $7/2^-$ ground state as observed in ^{167}Os$_{87}$ [19]. Allowing for the total conversion coefficient of 6.5 for a 95 keV M1 transition [65], the intensity of this transition is greater than that of the 490 keV E2 transition feeding the $9/2^-$ state. A parallel sequence of γ rays comprising the 499, 597, 559 and 593 keV transitions (shown on the right-hand side of Fig. 5.7) is also assumed to feed the ground state

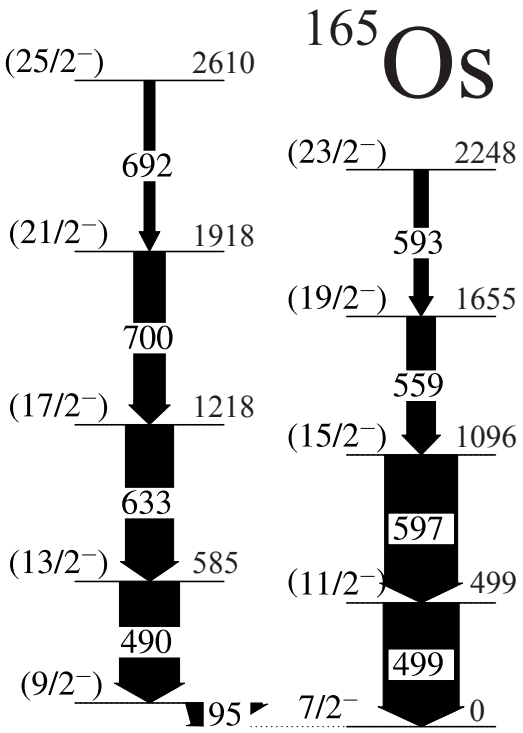

Figure 5.7: Level scheme deduced for ^{165}Os. The transition energies are in keV and their relative intensities are proportional to the width of the arrows. The Internal conversion intensity has been estimated and is included in the width of the arrows.

based on comparisons with the structure of ^{167}Os [19]. The energy spectrum of these summed γ-ray coincidences is shown in Fig. 5.5(c).

5.3 Discussion

The low-lying states in the neutron-deficient osmium isotopes are based on single quasiparticle configurations formed when the odd neutron occupies one of the available $f_{7/2}$, $h_{9/2}$ or $i_{13/2}$ states near the Fermi surface [66, 67, 68, 69, 70]. Figure 5.8 compares selected low-lying excited states in ^{163}Os and ^{165}Os with the ground state bands in their lighter even-N neighbours. The low-lying states in ^{163}Os and ^{165}Os fit in with the systematic trend of the light Os isotopes of increasing excitation energy in nuclei closer to N=82. This indicates a change in structure from collective rotations in the $N > 90$ Os isotopes towards a single-particle regime. Indeed, in ^{162}Os

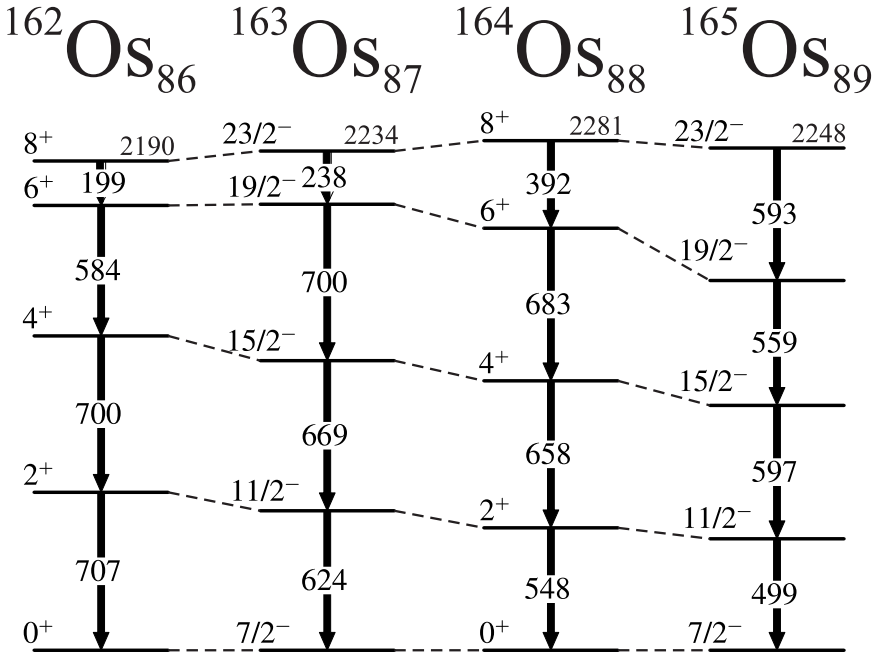

Figure 5.8: Comparison of energy levels in ^{163}Os and ^{165}Os with the ground state bands in their lighter even-N neighbours. All levels are placed relative to the ground state. All level spin assignments are tentative. The dashed lines connect states with similar structure.

a low-lying 8^+ state was identified and interpreted as the $(f_{7/2}, h_{9/2})_{8^+}$ or $(h_{9/2})^2_{8^+}$ configuration [16]. The low-lying $23/2^-$ state in ^{163}Os lies between the 8^+ states in the neighbouring even-N isotopes. Therefore, the $23/2^-$ states is interpreted as the maximally aligned $(f_{7/2}, h^2_{9/2})_{23/2^-}$ state.

There is evidence in this mass region for the existence of a low-lying $13/2^+$ isomer based on a configuration where the odd neutron occupies the $i_{13/2}$ orbital. The relative ordering of the single-quasiparticle excitations in nearby nuclei has been deduced from the electromagnetic decay paths of the $13/2^+$ isomeric state. For example, Scholey *et al.* measured the half-lives of the $13/2^+$ isomers in ^{163}W and ^{167}Os to be 154±3 ns and 672±7 ns, respectively and deduced that the decay path comprises an M2 transition to the $9/2^-$ state followed by an M1 transition to the $7/2^-$ ground state, see Fig. 5.9. Thus, the first excited structure is interpreted as

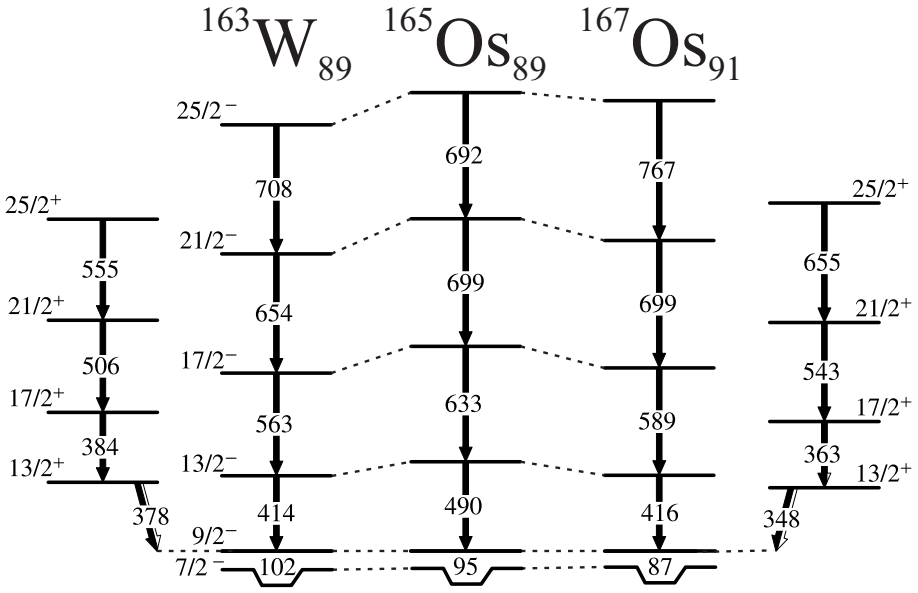

Figure 5.9: Comparison of energy levels in ^{165}Os with its heavier odd-N isotope ^{167}Os and its lower-Z isotone ^{163}W. All levels are placed relative to the ground state. All level spin assignments are tentative. The dashed lines connect states with similar structure.

a single quasineutron configuration based upon the $h_{9/2}$ orbital. Figure 5.9 compares the excited states based upon the $(9/2^-)$ state in ^{165}Os with the structures based on the $h_{9/2}$ configuration in the lighter even-Z ($N = 89$) isotone, ^{163}W [71] and the heavier odd-N isotope ^{167}Os [19]. This structure in ^{165}Os shows a marked similarity with these neighbouring nuclei and is also assumed to be based on the $h_{9/2}$ state.

The $\nu i_{13/2}$ band built on the $13/2^+$ isomer is the most intense structure in the yrast spectra of nearby odd-N nuclei, such as the $\nu i_{13/2}$ bands in ^{163}W and ^{167}Os shown in Fig. 5.9. However, in ^{165}Os only excited states built upon the $\nu f_{7/2}$ and $\nu h_{9/2}$ configurations have been observed. The absence of this structure in ^{165}Os is consistent with the trend of increasing excitation energy of the $i_{13/2}$ state with decreasing neutron number in the Os [66, 19], W [72, 71] and Ta [73] isotopes when approaching the $N = 82$ shell closure.

Chapter 6

Spectroscopy of ^{164}Ir

Spectroscopic studies of short-lived proton emitting nuclei lying between the N=82 and Z=82 shell closures have flourished in recent years thanks to the advent of increasingly advanced detection systems. In this area, proton emission strongly competes with alpha decay. This is due to the large relative reduction of the potential barrier for proton emission compared to an α decay. As described in Chapter 2, the half-lives for proton decay are extremely sensitive to the angular momentum of the emitted proton. Due to this fact, the properties of the proton decay can provide us with the configuration of the decaying state by direct comparison with theory. The configurations are not as easily derived from observations of the alpha decay from the same state.

In this region as the neutron number decreases, there is a general trend of increasing Q_p-values of respective states. As the half-life is strongly dependent on the Q_p-values, the life-times of the decaying states decrease rapidly with N. For this reason, along with the rapidly decreasing production cross sections, decay spectroscopy is becoming increasingly challenging as the limit of existence is approached. Nearly half of the known proton emitters have been discovered in the region $N > 82 > Z$ [74, 75, 76, 63, 77, 78, 79, 80, 40], thanks to increasingly sophisticated separation

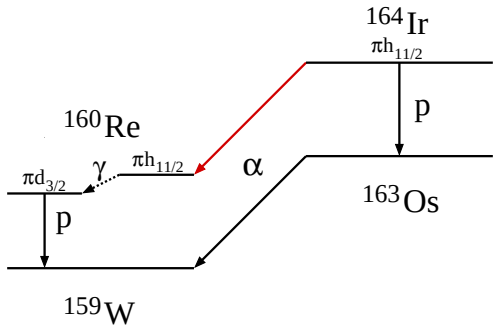

Figure 6.1: A decay scheme showing all decays used to calculate energy of the high spin state of ^{160}Re. The newly observed α decay is highlighted in red. All γ decays from to the ground state of ^{160}Re are yet to be observed [4], and are therefore indicated with a dashed line.

and decay tagging techniques [60, 61, 62]. These techniques however are limited by the time response of the detectors. To observe decay events that occur within the dead time of implantation an offline pulse shape analysis must be performed. Observations of particle emission from odd Z nuclei in this region often identify two decaying states with few exceptions. Most nuclei are observed to decay from both a high-spin and low-spin state owing to the protons occupying the $h_{11/2}$ and either the $s_{1/2}$ or $d_{3/2}$ orbitals. The following chapter will discuss the search for the decay of the low-spin state of ^{164}Ir and the first observation of the α decay of the high-spin state. Figure 6.1 shows the decay paths of ^{164}Ir, the previously unobserved alpha decay path is highlighted red.

6.1 Experimental Setup

The experiment was performed at the Accelerator Laboratory of the University of Jyväskylä where the beam was provided by the K130 cyclotron. The fusion-evaporation reaction ^{92}Mo(^{78}Kr,$p5n$)^{164}Ir was used in order to populate states in ^{164}Ir. The molybdenum target of thickness 0.5 mg/cm^2 was bombarded for 315 hours at energies of 420 - 450MeV with an average beam current of 10 pnA. The gas-

filled separator RITU [2] was used to suppress scattered beam and transport recoiling fusion products (recoil events) to the focal plane where they were implanted into the double-sided silicon strip detectors (DSSDs) of the GREAT spectrometer [3].

The front and back faces of the two DSSDs were instrumented with analogue and digital electronics respectively. The time stamp and energy for all signals detected in the y strips were recorded. Furthermore, traces representing pulses from the charge sensitive preamplifiers were recorded for the 80 digitized y-strips of the rear of the DSSD. The recorded trace length was 10.16 μs (1016 samples), during this time the rear strip was dead. However, piled up signals are visible in the traces.

The front 120 vertical strips were instrumented with analogue equipment, however, in addition to the position, time and energy information output from the ADC, a pattern register also recorded the position and time. As a pattern register only records time stamps it runs without dead time. The purpose of this arrangement was to eliminate the dead time of the detector caused by implantations, and therefore make it possible to regain pixel information of decays that happen within the dead time. The total dead time of the analogue electronics was ~ 7.4 μs; the energy of any subsequent signals can not be recorded during dead time. Using both the traces for y strips and the pattern register for the x strips, the pixel information for the pileup could be recovered for a signal during the dead time. The energy of the piled up signal was then extracted in an offline analysis.

All signals from both faces of the DSSDs were recorded by the triggerless Total Data Readout (TDR) data acquisition system and given a 10 ns time stamp. The analogue data were analysed using the GRAIN software package [51]. Correlations and analyses of traces were performed separately.

6.2 Results

The RDT technique has been employed to observe proton and α radioactivities of ^{164}Ir. The production cross section of ^{164}Ir is very low owing largely to the high number of evaporated particles needed for population. Figure 6.2 (a) is an energy spectrum of mother decay events in the DSSD occurring within 0.5 ms of recoil implantation. A low-energy calibration was performed using the previously observed ^{161}Re, ^{160}Re and ^{165}Ir decay lines. For very short time correlations (i.e. t < 200 μs) a baseline correction was performed by minimizing the FWHM of the strongest peaks. Labelled transitions were populated directly by fusion-evaporation. Some alpha peaks are present due to miscorrelations between the recoil and strongly populated, relatively long-lived daughter nuclei. The large range of alpha peaks present in this spectrum is reflective of the relatively high beam energy. The strong presence of 6-particle evaporation channels (e.g. ^{164}Os and ^{155}Lu) indicates that a sensible beam energy was chosen.

6.2.1 Proton radioactivity in ^{164}Ir

A new measurement of the $h_{11/2}$ isomer decay

Figure 6.2 (a) is DSSD energy spectrum of escape-vetoed mother events occurring within 0.5 ms of recoil implantation. The proton decay line of the high-spin state of ^{164m}Ir can easily be identified at previously observed energy[1]. Figure 6.2 (b) is an energy spectrum of escape-vetoed mother decay events followed by events that are characteristic of the ^{163}Os alpha decay ($E_\alpha = 6510$ keV, $t_{1/2} = 6.8 \pm 0.4$ ms [22]) and occur within 350 μs of recoil implantation. The high-spin proton emission line is clearly visible with very little background. Events to the lower end of the energy spectrum have been taken as escape events and have been included in the

[1]isomeric (or *metastable*) states are denoted with an m

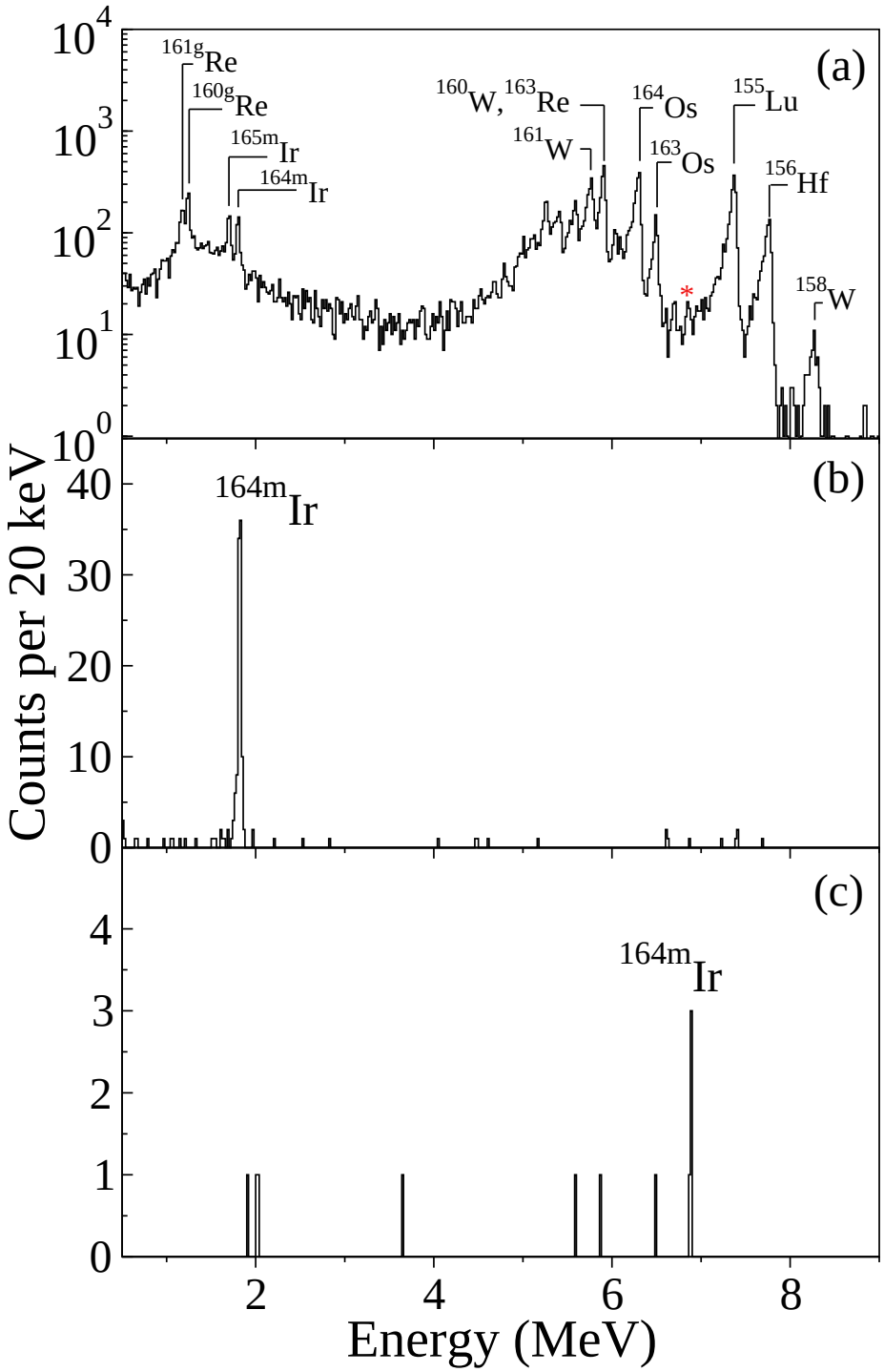

Figure 6.2: A DSSD energy spectrum showing (a) mother decay events occurring within 0.5 ms of recoil implantation, (b) mother decay events occurring within 350 μs of implantation followed by an ^{163}Os alpha decay and (c) mother decay events occurring within 350 μs of implantation followed by events characteristic of the ^{160m}Re proton decay.

calculation of the half life; in total, 100 full-energy high-spin proton decays were observed. The observed statistics are an order of magnitude higher than previous observations [77, 78]. The proton-decay energy was measured to be 1814 $\pm$ 6 keV, which is in good agreement with previous measurements. Using Equation 2.36, the energy of the decay corresponds to a Q-value of 1825 $\pm$ 8 keV. A screening correction of 16 keV [36] must be added to obtain a Q_p^{bare}-value for theoretical calculations of the reduced decay width.

Searching for the $d_{3/2}$ ground-state decay

As previously stated, the low-spin ground-state proton decay of ^{164}Ir is predicted to have a half-life shorter than the time period after recoil implantation in which the DSSDs are dead. The GRAIN analysis software package is unable to perform mother-daughter correlations of such events. The package was, however, used to record timestamps of events characteristic of the ^{163}Os alpha decay in anti-coincidence with the gas detector. A total of 5102 decay events were detected and the time stamps were recorded.

The following analysis was performed using independent C codes. Figure 6.3 is a histogram of both ADC and (deconvoluted) pattern register channels that fired during a short time period[2]. In general the pattern register rate is higher than the ADC rate; this is what one would expect as the pattern register runs without dead time. From the histogram, it can be seen that pattern register outputs coinciding with the 160-170 and 224 ADC channels did not record data during the experiment. Because of this, only strip correlations could be made within the 10 μs correlation time after recoil implantation.

The time stamps of the ^{163}Os events were used to make pixel correlations with recoiling nuclei. A time correlation of 25 ms was used to obtain recoil traces. All

[2]Pattern register channel numbers have been modified to coincide with the ADC channel number notation

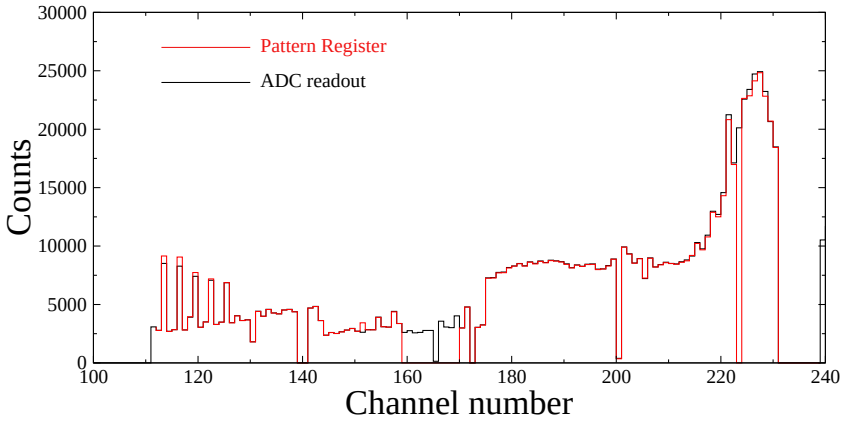

Figure 6.3: A comparison of analogue DSSD channels that were recorded to fire by the ADC (black) and pattern register (red).

traces within the time correlation were considered to be either recoiling ^{164}Ir or ^{163}Os ions. In total 6552 traces were correlated with the ^{163}Os decays which satisfied the energetic requirements of a recoil. Using the method to find piled up events described in Chapter 4, 6 traces were identified as proton decays. Using previously measured values of the half life, and assuming the same detection efficiency for the 100 counts between 10 - 500 μs, one would expect 8 $\pm$ 2 proton decays for $t < 10$ μs, which is in good agreement with the 6 observed. The correlated recoil traces are shown in Figure 6.4 (a).

Due to the small height of the pileup signal, the two traces highlighted green are interpreted as escaping proton decays following recoil implantation. The escape ratio is consistent with a typical value of 40%. An energy spectrum of the traces obtained using the the super-pulse method is shown in Figure 6.4(b). The energy resolution is poor for several reasons. The main reason is the very short base line that was recorded by the Lyrtech cards; for each trace there were only 10 samples of the baseline before the rise. Although the chi-squared of the fit is generally low after charge collection, the chi-squared of the base line fit is very large. The result is a poor calibration of the scaling-factor-to-energy relationship. Furthermore, the

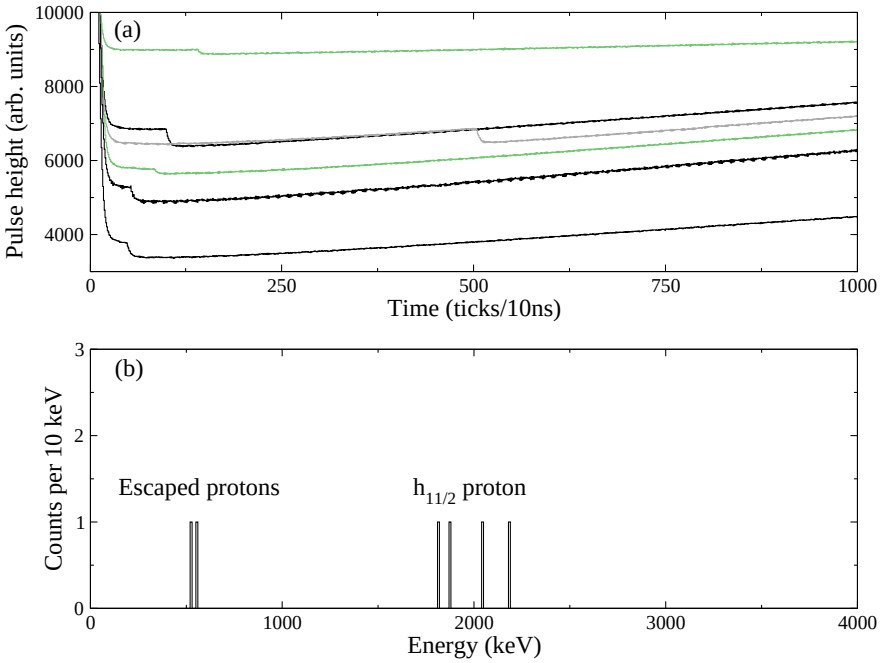

Figure 6.4: (a) Recoil traces followed by an ^{163}Os alpha decay event within 25 ms. (b) Energy spectrum acquired from pile up signals in (a), the green traces are considered to be signals arising from escaping protons

energy was assumed to be linearly related to the trace height as statistics were too low to perform a low-energy calibration for each strip. Discrimination between the ground-state decay and the isomer cannot be made, but these events can be used in addition to the isomer decays to calculate a half-life.

6.2.2 The First Observation of The Isomer Alpha Decay

The RDT method has been employed to make correlations with the decay of the very weakly populated ^{164}Ir nucleus. The alpha decay daughter of ^{164}Ir, ^{160}Re, also has a short half-life of 611 $\pm$ 7 μs [81]. The half lives for both the mother and daughter nucleus are very short in comparison to the more strongly populated decay chains, making them ideal for using the RDT method. Figure 6.2 (c) shows an energy spectrum of events following a recoil within 350 μs that are followed by a daughter decay within 3 ms with an energy of the ^{160g}Re proton decay. A peak of 4 counts

can be seen at an energy of 6880 ± 10 keV. Due to the very short correlation time, there is a very low peak-to-background ratio. This peak can be seen in Figure 6.2 (a) (highlighted with an asterisk) and has been identified as the alpha decay of the $h_{11/2}$ state; the energy corresponds to a Q-value of 7052 ± 10 keV.

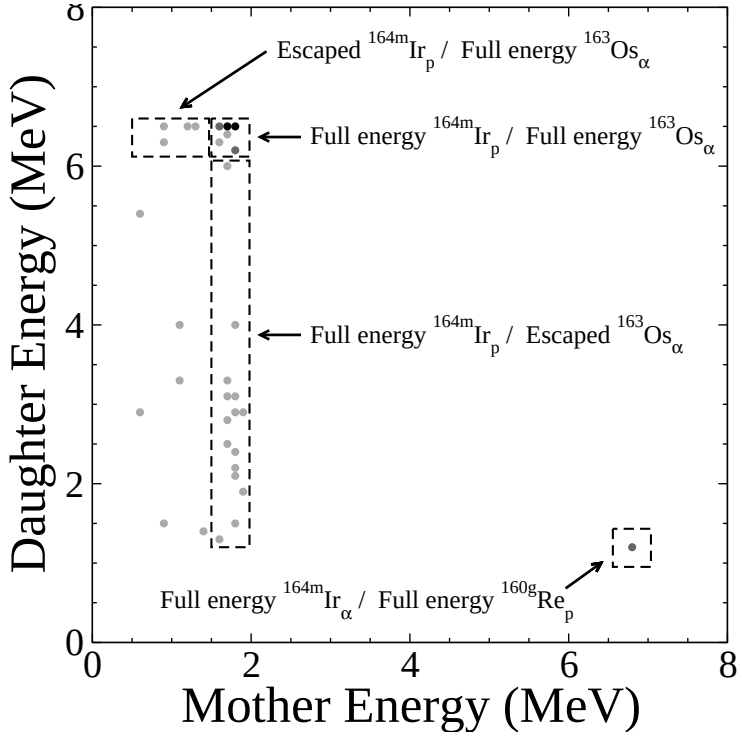

Figure 6.5: A two-dimensional energy plot of mother events (x-axis) occurring within 350 μs of recoil implantation followed by a daughter decays (y-axis) within 28 ms, followed by events characteristic of the ^{159}W alpha decay.

Further constraints can be set to unambiguously identify the 6880 keV peak as the high spin state alpha decay. Figure 6.5 shows a 2D plot of mother-daughter correlations. The conditions are such that the mother decay occurs within 0.35 ms of recoil implantation followed by a daughter alpha decay without time constraints, followed by a granddaughter alpha decay characteristic of ^{159}W (6283 keV) within 28 ms. The alpha and proton daughters of ^{164}Ir have different half-lives. A mother-daughter correlation time should, therefore, not be used when calculating the relative branching. Two alpha decays have been correlated with the ^{160}Re daughter ground-state proton decay. A total of 42 $^{164}Ir_p$-$^{163}Os_\alpha$-$^{159}W_\alpha$ correlations were observed

(including mother/daughter escapes highlighted in Figure 6.5). An alpha-branching ratio of 4.5 ± 3.3 % is obtained.

Using a mother-daughter correlation time of 350 μs, a total 5 full-energy alpha decays were correlated with the ^{160}Re daughter proton decay[3]. This is in agreement with a $\sim$ 40 % escape probability[4]. The full-energy peak efficiency must be taken in to consideration when calculating the branching ratio's of different decay modes. The full-energy peak efficiency was measured to be 0.58 and 0.59 for proton and alpha decay, respectively. Using the 5 $^{164}\mathrm{Ir}_{\alpha}$-$^{160}\mathrm{Re}_{p}$ and 100 $^{164}\mathrm{Ir}_{p}$-$^{163}\mathrm{W}_{\alpha}$ correlations, an alpha-branching ratio of 4.8 ± 2.2 % is obtained for the high-spin state. Combining decay times of the alpha and the proton decay, a half life of $t_{1/2}$= 70 ± 10 μs is obtained using the maximum-likelihood method [82].

6.3 Discussion

The low-seniority shell model discussed in Reference [40] calculates the spectroscopic factor of proton emission based on the number of proton-hole pairs below the Z=82 shell gap exist in a particular isotope. Figure 6.6 shows theoretical spectroscopic factors for the $\pi d_{3/2}$ and $\pi h_{11/2}$ orbitals for a given isotope (see caption) along with experimentally measured proton-decay widths in this area. A stringent test of spherical shell model calculations [83, 40] requires high-precision measurements of proton-decay Q-values and half-lives. The precision of the reduced proton-decay width for $^{164\mathrm{m}}$Ir has been improved significantly and serves as a good test of the low-seniority spherical shell model. A proton-decay width of $0.298^{+0.058}_{-0.055}$ has been measured. It can be seen in Figure 6.6 that this value is in good agreement with the low-seniority spherical shell model.

Figure 6.7 shows high spin alpha decay Q-value systematics of odd-odd nuclei

[3]Again, a mother-daughter correlation time was not used
[4]In comparison with the 2 $^{164}\mathrm{Ir}_{\alpha}$-$^{160}\mathrm{Re}_{p}$-$^{159}\mathrm{W}_{\alpha}$ correlations

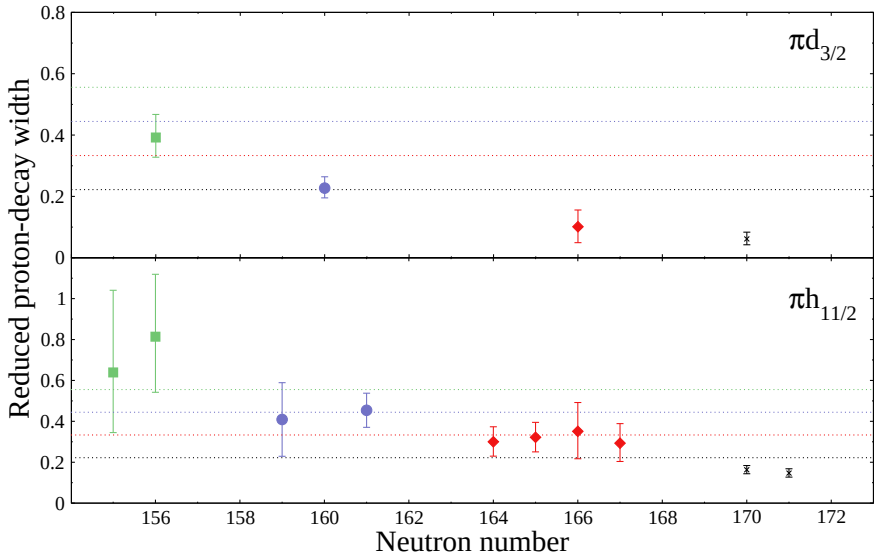

Figure 6.6: Experimental spectroscopic factors plotted against neutron number for isotopes of lutetium (green), rhenium (blue), iridium (red) and gold (black). The dotted lines are theoretical spectroscopic factors for their respective isotopes (colour co-ordinated).

as a function of neutron number. The open symbols represent Q-values predicted in Ref. [5], and are shown to highlight the expected trend with decreasing N. The new ^{164m}Ir alpha-decay Q-value is highlighted in red. As expected, the Q-value increases almost linearly as the neutron number decreases. An alpha branching ratio of 4.8 ± 2.2 % corresponds to a partial half-life of 1.5 ± 0.7 ms. Using the WKB approximation [34] with the Igo potential [35], a reduced decay width of 41.1 ± 19.8 keV is obtained which corresponds to an unhindered alpha decay.

In a recent study by Darby *et al.* [4], it was shown that an isomeric high-spin state exists in ^{160}Re that preferentially decays via gamma emission. The energy of this high spin state was predicted in Ref. [5] by a simple interpolation of the high spin Q_p-values of ^{164}Ir and ^{156}Ta less a mean deviation to be 185 ± 21 keV. Using a weighted average from References [84, 63, 85, 76] one obtains $Q_\alpha(^{163}\text{Os}) = 6668 \pm 5$. This combined with the recently reported $Q_p(^{160g}\text{Re})$=1272 ± 6 keV [81] and both proton and alpha ^{164m}Ir Q-values measured in the present study, one obtains

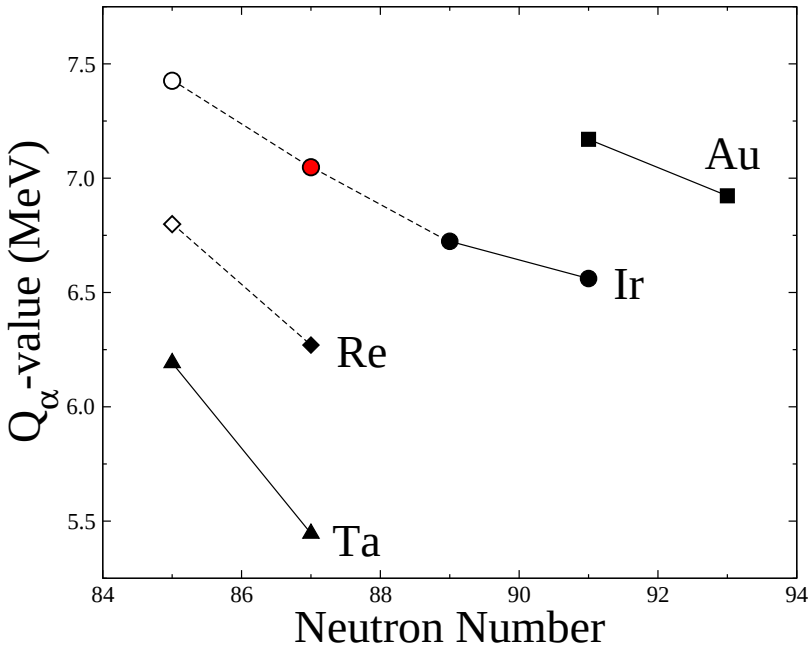

Figure 6.7: Alpha decay Q-values from the $h_{11/2}$ state of odd-odd nuclei as a function of neutron number. The measured Q-value for ^{164}Ir is highlighted with red. Open symbols are Q-values predicted in Ref. [5]

an excitation energy of the ^{160}Re $h_{11/2}$ state of 169 ± 14 keV using the formula

$$E = Q_p(^{164m}\text{Ir}) + Q_\alpha(^{163}\text{Os}) - Q_\alpha(^{164m}\text{Ir}) - Q_p(^{160g}\text{Re}). \quad (6.1)$$

This value is in good agreement with the interpolation. The motivation for search for the high spin state of ^{160}Re stems from the absence of charged particle emission. This is the only example of a proton-emitting nucleus where only the low-spin state is observed. Possible reasons for this are discussed in terms of a change in structure in Ref. [4]. In that work, two gamma emitting states are observed with gamma-ray energies of 96 keV and 38 keV which were interpreted as the $9^+ \rightarrow 7^+$ and $7^+ \rightarrow 6^-$ transitions, respectively. The remaining ground-state E2 transition ($4^- \rightarrow 6^-$) was not observed (see Figure 6.8). However, using the excitation energy obtain in Equation 6.1, one would expect to see a transition at 35 ± 14 keV; at this energy, the electron conversion coefficient for an E2 transition is $\sim$ 500. The calculated excita-

tion energy is consistent with predicted $h_{11/2}$ energy level of ^{164}Ir and implies s-wave alpha emission from the $h_{11/2}$ state in ^{164}Ir. This is consistent with the observation that the alpha decay is unhindered. A level scheme of ^{160}Re showing gamma-ray transitions observed in References [4, 86] is shown in Figure 6.8, the newly observed alpha decay is shown to feed in the 9^+. The figure includes unobserved transitions shown as dashed lines.

Unlike ^{160}Re, only the high-spin state has been observed for ^{164}Ir. For odd-odd nuclei in this region, the unpaired proton and neutron couple according to the Nordheim rules [87]. These state that if one of the nucleons has antiparallel spin and one has parallel spin to their respective orbital angular moment, they will couple to give the lowest possible total angular momentum (i.e. $j_1 = l_1 \pm s_1$ coupled with $j_2 = l_2 \mp s_2$), or, if *both* nucleons have anti-parallel or parallel spin then they couple to give the highest possible total angular momentum (i.e. $j_1 = l_1 \pm s_1$ coupled with $j_2 = l_2 \pm s_2$). In the case of ^{164}Ir, when an unpaired proton in the $d_{3/2}$ shell model orbital couples with the unpaired neutron in the $f_{7/2}$ orbital, the resulting spin takes the lowest possible value of 2^-. An unpaired proton in the $h_{11/2}$ orbital couples with the unpaired $\nu f_{7/2}$ orbital resulting in the fully aligned 9^+ state. The large change in spin means that gamma emission to the ground state is slow with respect to particle emission. The result is a low gamma-decay branching ratio, and in turn a weakly populated ground-state with respect to the high-spin state. This combined with the lowering of the centrifugal barrier for a unpaired $d_{3/2}$ proton of an already short-lived nucleus results in extremely low detection probabilities.

In Figure 6.6, it can be seen that although the spectroscopic factors for $\pi h_{11/2}$ emission are well reproduced, the experimental spectroscopic factor for $d_{3/2}$ proton emissions deviate from the low-seniority shell model predictions. This deviation is explained in terms of particle-vibration coupling (see Ref. [83]), where by a 2^+ phonon couples with a $d_{3/2}$ proton so that a different centrifugal barrier is experi-

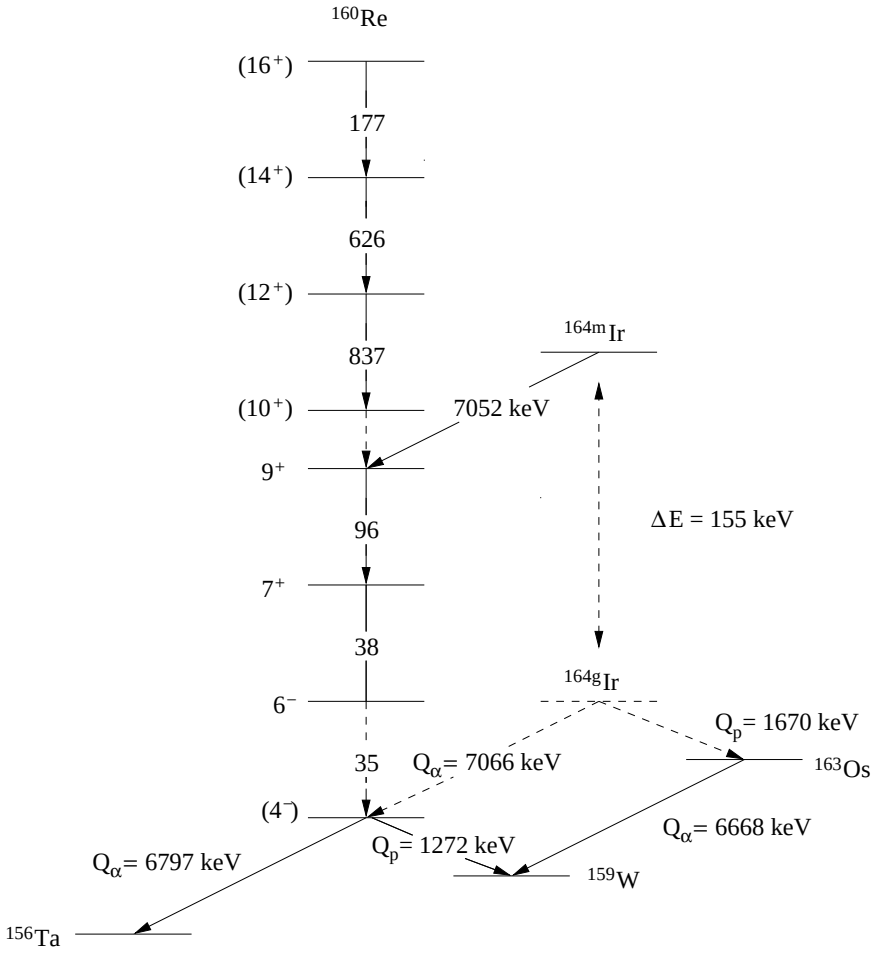

Figure 6.8: A decay scheme of some of the nuclei involved in this analysis. All gamma transitions are shown in keV. Proton, alpha and gamma-ray transitions are shown as right, left, and vertical pointing arrows, respectively. Unobserved transitions are shown as dashed lines. The extrapolated value for the Q_α and Q_p of ^{164g}Ir is shown. Tentative spins and parities are shown in parentheses.

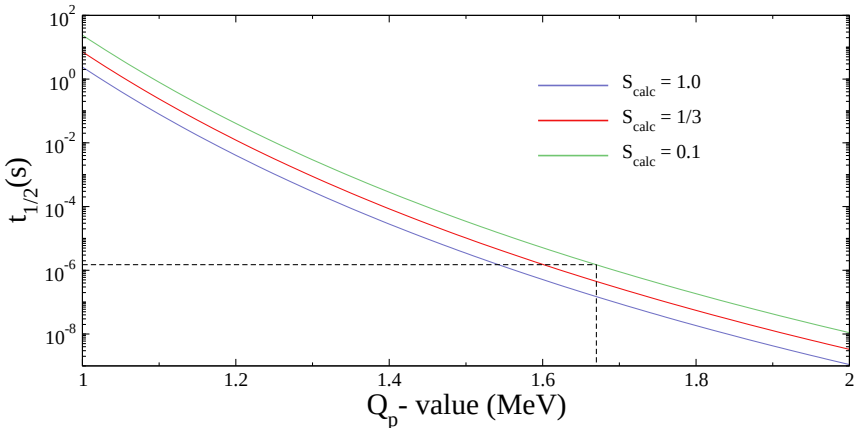

Figure 6.9: Theoretical half life of the $d_{3/2}$ proton decay as a function of Q-value for $S_{calc} = 1$, $\frac{1}{3}$ and 0.1. The dashed line indicates the point of the extrapolated Q-value of 1.55 MeV for the ground-state decay.

enced which results in a distorted spectroscopic factor. The Q_α-value of the ^{164g}Ir can be estimated by an extrapolation of ground-state alpha decay Q-values of ^{166g}Ir (6724 ± 6 keV [40]) and ^{168g}Ir (6382 ± 10 keV [88]) as 7066 ± 12 keV. In a similar fashion to Equation 6.1, the Q-value of the ground-state proton decay of ^{164}Ir can be estimated. Using the equation

$$Q_p(^{164q}\mathrm{Ir}) = Q_\alpha(^{164g}\mathrm{Ir}) + Q_p(^{160g}\mathrm{Re}) - Q_\alpha(^{163}\mathrm{Os}), \tag{6.2}$$

a Q-value of 1670 ± 14 is obtained. The decays involved in this calculation are shown in Figure 6.8. This Q-value corresponds to an excitation energy of 155 keV for the $h_{11/2}$ state which fits well with systematics. Using a spectroscopic factor of 0.33 a half-life of $\sim$ 0.5 μs is obtained for the $d_{3/2}$ proton emission. However, if it is assumed that the spectroscopic factor for ^{164}Ir deviates from theory in the same manner as it does in ^{165}Ir ($S_{exp} = 0.1$), the half life is increased to $\sim$ 1.5 μs. Even so, a time-of-flight of $\sim$0.5 μs means that 20 % of low spin states decay before of implantation. This coupled with the extremely low production cross section and the poor energy resolution of the trace analysis make it impossible to distinguish

between the ground state and isomer in the piled up traces.

Chapter 7

Summary

Gamma-ray transitions have been observed for the first time in the highly neutron-deficient nucleus ^{163}Os. The low-lying yrast structure has been established to a tentative spin and parity $23/2^-$ corresponding to the maximally aligned $(f_{7/2}, h_{9/2})^3_{23/2^-}$ state. A level scheme for the heavier odd-N isotope ^{165}Os has also been established for the first time. The level structures in both nuclei are interpreted in terms of configurations involving the negative-parity $f_{7/2}$ and $h_{9/2}$ neutron orbitals and reflect the transition from γ-soft shapes observed in the heavier isotopes to near spherical shapes near the closed $N = 82$ shell. The observation of excited states in ^{163}Os and ^{165}Os completes the knowledge of excited states in the osmium nuclides spanning an uninterrupted isotopic chain from $^{162}\mathrm{Os}_{86}$ to $^{199}\mathrm{Os}_{123}$.

The proton decay from the high-spin state of ^{164}Ir has been observed and its energy measured to a higher precision than previous measurements as 1814 $\pm$ 6 keV. The absence of $\mathrm{d}_{3/2}$ proton decay in the analogue data indicates that the spectroscopic factor is lower than that predicted in the low seniority shell model. Mother-daughter-granddaughter correlations have been made that unambiguously identify the alpha decay of the high-spin state of ^{164}Ir for the first time. The alpha decay has an energy of 6880 $\pm$ 10 keV. By combining the life time information

for these decay, a half life of 70 ± 10 μs was measured. Using an optical model proposed by Bechetti and Greenlees [39], a WKB approximation was used to calculate a reduced-proton decay width of $0.298^{+0.058}_{-0.055}$. This is in very good agreement with the theoretical value of $0.\dot{3}$ from the low seniority shell model proposed by Davids *et al.* in Ref. [40].

The alpha-decay branching ratio has been measured to be 4.8 ± 2.2 %. By comparison with WKB approximation of the nuclear potential using the Igo potential, a reduced alpha decay width of has been calculated to be 41.1 ± 19.8 keV which is indicative of an unhindered s-wave emission. Furthermore, the energy of the decay yields an excitation of the high-spin state of the daughter nucleus, ^{160}Re, of 169 keV, which is consistent with the observations reported in References [86] and [4].

The DSSDs of the GREAT spectrometer at the Accelerator Laboratory of the University of Jyväskylä have been instrumented using digital electronics for the first time. Correlations were made between events characteristic of the ^{163}Os alpha decay and proton decays of ^{164}Ir that occurred within the dead time of the detector after recoil implantation. Due to low statistics and poor energy resolution, discrimination between the $d_{3/2}$ and $h_{11/2}$ proton decay cannot be made in the traces. However, the results have shown that the trace analysis used to observe short-lived charged particle emissions is valid. Future experiments of the same nature should record a longer baseline prior to recoil implantation in order to improve energy resolution. For further validation of the method, the analysis should be performed on a known particle emission on a stronger reaction channel.

Bibliography

[1] P. Greenlees, PhD thesis, University of Liverpool, 1999.

[2] M. Leino *et al.*, NIMB **99**, 653 (1995).

[3] R.D. Page *et al.*, NIMB **204**, 634 (2003).

[4] I.G. Darby *et al.*, Physics Letters B **695**, 78 (2011).

[5] R. D. Page, Phys. Rev. C **83**, 014305 (2011).

[6] E. Rutherford, Philosophical Magazine **21** (1911).

[7] J. Chadwick, Nature **129**, 312 (1932).

[8] L. Bianco *et al.*, Phys. Lett. **B690**, 15 (2010).

[9] T. Kurtukian-Nieto *et al.*, Preprint, 2007.

[10] R. Robinson and M. Thoennessen., At. Data Nucl. Data Tables **98**, 911 (2012).

[11] L. Fortunato, S. De Baerdemacker and K. Heyde, Phys. Rev. **C74**, 014310 (2006).

[12] T. Kibedi *et al.*, Nucl. Phys. **A567**, 183 (1994).

[13] P.M. Davidson, Nucl. Phys. **A568**, 90 (2001).

[14] J.L. Wood and K. Heyde, Rev. Mod. Phys. **83**, 1467 (2011).

[15] E. McCutchan and N. Zamfir, Phys. Rev. **C71**, 054306 (2005).

[16] D.T. Joss *et al.*, Phys. Rev. **C70**, 017302 (2004).

[17] S.L. King *et al.*, Phys. Rev. **C62**, 067301 (2000).

[18] D.E. Appelbe *et al.*, Phys. Rev. **C66**, 014309 (2002).

[19] D. O'Donnell *et al.*, Phys. Rev. **C79**, 064309 (2009).

[20] D.T. Joss *et al.*, Nucl. Phys. **A689**, 631 (2001).

[21] H. Kettunen *et al.*, Phys. Rev. **C69**, 054323 (2004).

[22] C.R. Bingham *et al.*, Phys. Rev. **C54**, R20 (1996).

[23] P.J. Sapple *et al.*, Phys. Rev. **C84**, 054303 (2011).

[24] S.J. Steer *et al*, Phys. Rev. C **84**, 044313 (2011).

[25] K. Heyde, *Basic Ideas and Concepts in Nuclear Physics* (Institute of Physics, 1994).

[26] A. H. Wapstra, *Nuclear spectroscopy tables* (North-Holland, Amsterdam, 1959).

[27] K.S. Krane, *Introductory Nuclear Physics* (John Wiley & Sons, 1988).

[28] M. Mayer, Phys. Rev. **75**, 1969 (1949).

[29] O. Haxel and J.H.D. Jensen and H.E. Suess, Phys. Rev. **75**, 1766 (1949).

[30] R.F. Casten, *Nuclear Structure form a simple perspective* (Oxford Science Publications, 2000).

[31] S. Hofmann, *Particle Emission from Nuclei* (CRC Press, 1989).

[32] A. Jain and V. Tewary, Zeitschrift Für Astrophysik **54**, 107 (1962).

[33] H. Geiger and J. Nuttall, Philosophical Magazine **22** (1911).

[34] J. Rasmussen, Phys. Rev. **113**, 1593 (1959).

[35] G. Igo, Phys. Rev. Lett. **1**, 72 (1958).

[36] K.N. Huang and H. Mark, At. Data Nucl. Data tables **18**, 243 (1976).

[37] H. Bethe, Rev. Mod. Phys. **9** (1937).

[38] J. Rasmussen, Xi - alpha-decay, in *Alpha-, Beta- and Gamma-Ray Spectroscopy*, edited by K. Siegbahn, pp. 701 – 743, Elsevier, Amsterdam, 1968.

[39] F. Becchetti and G. Greenlees, Phys. Rev. **182**, 1190 (1969).

[40] C.N. Davids *et al.*, Phys. Rev. C **55**, 2255 (1997).

[41] V.F. Weisskopf, Phys. Rev. **83**, 1073 (1951).

[42] H. Hbel, Progress in Particle and Nuclear Physics **54**, 1 (2005).

[43] C. W. Beausang *et al.*, Nucl. Instrum. Methods. Phys. Res. A. **313**, 37 (1992).

[44] C.W. Beausang and J. Simpson, J Phys G Nucl. Partic. **22**, 527 (1996).

[45] M. Leino *et al.*, Nucl. Instrum. Methods. Phys. Res. B. **126**, 320 (1997).

[46] R. Carroll, PhD thesis, University of Liverpool, 1999.

[47] I.H. Lazarus *et al.*, IEEE Trans. Nucl. Sci. **48**, 567 (2001).

[48] R. Firestone and V. Shirley, *Table of Isotopes, 2 Volume Set* (John Wiley & Sons, 1998).

[49] D. C. Radford, Nucl. Instrum. Methods. Phys. Res. A **361**, 297 (1995).

[50] H. Bethe, Annalen der Physik **397**, 325 (1930).

[51] P. Rahkila, Nucl. Instrum. Methods. Phys. Res. A **595**, 637 (2008).

[52] J. Simpson *et al.*, J Phys G Nucl Partic **18**, 1207 (1992).

[53] Cremat, Cr-110 charge sensitive preamplifier: application guide, 2013.

[54] A. Georgiev, W. Gast, and R. Lieder, IEEE Trans Nucl. Sci. **41**, 1116 (1994).

[55] R. Carola, Ph.D. thesis, University of Heidelberg, 2004.

[56] J. Uusitalo *et al.*, Nucl. Instrum. Methods. Phys. Res. B. **204**, 638 (2003).

[57] J. Sarén *et al.*, Nucl. Instrum. Methods. Phys. Res. A. **654**, 508 (2011).

[58] R. D. Page *et al.*, Nucl. Instrum. Methods. Phys. Res. B. **204**, 634 (2003).

[59] I.H. Lazarus *et al.*, IEEE Trans. Nucl. Sci. **48**, 567 (2001).

[60] K.H. Schmidt *et al.*, Phys. Lett. **B168**, 39 (1986).

[61] R.S. Simon *et al*, Z. Phys. **A325**, 197 (1986).

[62] E.S. Paul *et al.*, Phys. Rev. **C51**, 78 (1995).

[63] R.D. Page *et al.*, Phys. Rev. **C53**, 660 (1996).

[64] J. Simpson *et al.*, J. Phys. **G18**, 1207 (1992).

[65] T. K. *et al.*, Nucl. Instrum. Methods Phys. Res. A. **589**, 202 (2008).

[66] R.A Bark *et al.*, Nucl. Phys. **A646**, 399 (1999).

[67] R.A. Bark, G.D Dracoulis and A.E. Stuchbery, Nucl. Phys. **A514**, 503 (1990).

[68] C.A. Kalfas *et al.*, Nucl. Phys. **A526**, 205 (1991).

[69] B. Fabricius *et al.*, Nucl. Phys. **A511**, 345 (1990).

[70] G.D Dracoulis, C. Fahlander and A.P. Byrne, Nucl. Phys. **A401**, 490 (1983).

[71] J. Thomson *et al.*, Phys. Rev. **C81**, 014307 (2010).

[72] G. D. Dracoulis *et al.*, Proceedings of the International Conference of Nuclear Structure at High Angular Momentum, Ottawa, AECL Report No. 10613 **2**, 94 (1992).

[73] K. Lagergren *et al.*, Phys. Rev. **C83**, 014313 (2011).

[74] R.D. Page *et al.*, Phys. Rev. Lett. **68**, 1287 (1992).

[75] R.J. Irvine *et al.*, Phys. Rev. C **55**, R1621 (1997).

[76] H. Kettunen *et al.*, Phys. Rev. C **69**, 054323 (2004).

[77] H. Kettunen *et. al.*, Acta Phys. Pol. A **32**, 989 (2001).

[78] H. Mahmud *et al.*, European Physical Journal A **15**, 85 (2002).

[79] D.T. Joss *et al.*, Phys. Lett. B **641**, 34 (2006).

[80] J. Uusitalo *et al.*, Phys. Rev. C **59**, R2975 (1999).

[81] I.G. Darby *et al.*, Phys. Rev. C **83**, 064320 (2011).

[82] P. L. Meyer, J. Amer. Statist. Assoc. **62**, 1258 (1967).

[83] C.N. Davids *et al.*, Phys. Rev. C **64**, 034317 (2001).

[84] C.R. Bingham *et al.*, Phys. Rev. C **54**, R20 (1996).

[85] S. Hofmann *et al.*, Z.Phys. **A299**, 281 (1981).

[86] P. Sapple, PhD thesis, University of Liverpool, 2010.

[87] L. W. Nordheim, Rev. Mod. Phys **23**, 322 (1951).

[88] B. Hadinia *et al.*, Phys. Rev. C **80**, 064310 (2009).